A novel algorithm for inferring the vertical distribution of trace gases using remote sensing measurements

Thesis by
Harrison Alexander Parker

In Partial Fulfillment of the Requirements
for the degree of
Doctor of Philosophy

CALIFORNIA INSTITUTE OF TECHNOLOGY
Pasadena, California

2023
Defended May 31st, 2023

Harrison Alexander Parker
ORCID: 0000-0002-0041-2764

ACKNOWLEDGEMENTS

First, I would like to acknowledge my advisor, Paul Wennberg, for his support and patience through my time at Caltech. Your passion for science and discovery is something I hope to emulate. Over the years, I have learned from many wonderful folks in the Wennberg and Seinfeld groups and at JPL. Coleen Roehl, you have always been patient and kind when responding to any odd question I could ask you. Debra Wunch, you helped me learn everything I could about TCCON and were encouraging at every step. Joshua Laughner, thank you for spending hours going though nitty, gritty math with me and becoming my good friend through professional and personal interests alike. Geoff Toon, you were a fountain of knowledge about everything spectral. Greg Osterman, thank you for creating such a welcoming and supportive academic environment. John Crounse, perpetually calm and collected, thank you for your help with everything in situ. Camille Viatte, thank you for teaching me how to be a professional scientist. Jacob Hedelius, you showed me the ropes and helped me find a sense of community at Caltech — thank you.

I would like to thank the members of my thesis advisory committee. Christian Frankenberg's approachability was crucial to making it through my first years here at Caltech. Mitchio Okumura's consistency and patience really helped when struggling through difficult topics. John Seinfeld, I truly appreciate your personal and caring approach to every one of your advisees.

None of the work I have done would have been possible without the support of the Linde staff. Nora Oshima, Bronagh Glaser, Leilani Rivera-Dotson, and Carolyn Rosales, I will always remember our break room discussions about life, work, and, of course, tea. This building would fall apart without you all and I really appreciate all the support over the years.

I will try to be brief, but I have met so many wonderful people at Caltech. The following is in no particular order and, if I have not included someone, I apologize and guarantee it is not an intentional omission. Zachary Erikson, I enjoyed the times spend drinking tea and watching the rain. Krystal Vasquez, thank you for showing me what it means to speak to power. Hannah Allen, I loved all our long, nerdy conversations and all the DnD sessions. James Park, you put up with a lot in our office and are a tremendous scientist. Dien Wu, I appreciate all our conversations and your patience with teaching me about your work. Haroula Baliaka, you are so strong and so kind. Kat Ball, your optimism and energy are infectious. Henry Peterson, we have too much in common and it is amazing. Sophia Charan, all our game nights were amazing and I am so glad you are making the world a better place. Yuanlong Huang, I always appreciated your continuous support and loved our discussions about life. Ryan Ward, thank you for always pulling me back to the real world. Ben Schulze, your passion for science is truly amazing and I appreciate all your support in both the personal and academic spheres.

To those in Linde 121, thank you for going along on this ride for the last few years and 'yes, and' -ing all the weird shenanigans that went on. Ariana Tribby, thank you for helping me find ways to express my experiences, I am so glad to have you and Cris in my life. Maria Yu, you came into a very strange office and quickly found your part in the madness, it has been wonderful to have you

as an officemate. Lily Dove, a companion through so many things, you have taught me as much and more than I have learned in grad school — I'd like to see a caterpillar do that. Sara Murphy, I will always fondly remember our existential discussions and their degradation into absurd internet speak. Reina Buenconsejo (I am absolutely including you in the Linde 121 group), your friendship has made me a better person, thank you for being you.

With no exaggeration, learning about pedagogy from the Center for Teaching Learning, and Outreach (CTLO) changed my life. I am indebted to everyone at the CTLO and hope to pay it forward. In particular, I would like to thank Cassandra Horii for leading Caltech through the chaos of the transition to remote learning and always upholding equitable and inclusive principles. Jenn Weaver, you have been an incredible mentor, teacher, supervisor, and friend. It gives me hope to know that you are fighting the good fight and making the world a better place. Jennifer Imamura, I admire your continuous tenacity and welcoming approach. You make me believe that anything can be done. Leslie Rico, the CTLO would fall apart without you. Thank you for helping my naïve, young self figure things out. Unfortunately, my time with the CTLO was limited and I wish that I had had more time to work with Mitch Aiken, Kitty Cahalan, and the amazing current team members. If you are reading this and have a chance or opportunity to work with the CTLO, make it happen.

My family has been so supportive of my time in grad school and I could not have finished this without them. Mom and Dad, thank you for believing in me and pushing me to learn at every opportunity, it's worth more than a Nobel. Taylor, thank you for always being there and sharing in the most absurd and unique experiences of grad school and life — I owe you money for a trip. Austin, you and Alys have been consistently, immediately, and unconditionally supportive and it means the world. Jessie, you have treated me like family since you met me, and I hope someday to have a tenth of your character. Gilbert, thank you for always reminding me that life should be fun and that it is absolutely necessary to find joy in it.

Boots, we have conquered mountains and deserts and beaches. Momo, you are the best scruff scruff. Denali, you are most definitely a good boy.

Mike, you are the best friend anyone could hope for, far better than I have deserved at times. You have truly taught me the meaning of friendship. I can't wait to get together when we are older to look back on all the wild times that are yet to come. I'm so glad I had a five-pound bag of skittles that day.

And finally, Jackie. Meeting you was the first day of my life. You are my everything. Every step of the way you have accepted me for who I am. You are so open, loving, and warm and you make the world a better place for everyone around you. I am in continuous awe of your drive and passion. It has made me a better person in every facet of life. It can be hard to be completely certain in life and yet I am certain that, no matter where life goes, I want to go there with you.

ABSTRACT

Remote sensing is a powerful tool that is used to diagnose sources, sinks, and fluxes of trace gases across different spatial and temporal scales. Ground-based remote sensing measurements of column-averaged dry mole fractions (DMF) of gases such as carbon dioxide (CO_2) and carbon monoxide (CO) made by the Total Carbon Column Observing Network (TCCON) are used to validate space-based measurements and better understand the carbon cycle. Surface signals of gas exchange can be masked in the total column values, however, limiting their use in assessment of local surface fluxes. Retrievals of the vertical distribution of trace gases can be used to obtain gas exchange information that is more directly related to changes at the surface but require high precision measurements with less temporal resolution than the TCCON total column measurements. In this thesis, I develop an algorithm, the Temporal Atmospheric Retrieval Determining Information from Secondary Scaling (TARDISS), that infers vertical information, or 'partial columns', from existing, quality-controlled total column data. The TARDISS algorithm does not fit the solar spectra but rather begins with trace gas column retrievals obtained from different spectral bands using the standard TCCON retrievals. TARDISS takes advantage of the fact that different bands have different sensitivities to the same trace gas as a function of altitude and solar zenith angle. We use the TARDISS partial column data to examine estimated surface fluxes in the North American boreal forest and compare them to surface fluxes estimated from tall tower in situ measurements. We also outline changes in air quality from the sudden change in traffic behavior from the COVID-19 lockdown which serves as motivation for the use of the TARDISS-derived lower partial column CO data to examine recent changes in air quality in the South Coast Air Basin.

PUBLISHED CONTENT AND CONTRIBUTIONS

Scientific Publications

Parker, H. A., Hasheminassab, S., Crounse, J. D., Roehl, C. M., & Wennberg, P. O. (2020). Impacts of Traffic Reductions Associated With COVID-19 on Southern California Air Quality. Geophysical Research Letters, 47(23). https://doi.org/10.1029/2020GL090164

H.A.P performed research, analyzed data, and wrote the manuscript.

Parker, H. A., Laughner, J. L., Toon, G. C., Wunch, D., Roehl, C. M., Iraci, L. T., Podolske, J. R., McKain, K., Baier, B., and Wennberg, P. O.: Inferring the vertical distribution of CO and CO_2 from TCCON total column values using the TARDISS algorithm, Gases/Remote Sensing/Data Processing and Information Retrieval, https://doi.org/10.5194/amt-2022-322, 2022.

H.A.P performed research, analyzed data, and wrote the manuscript.

TABLE OF CONTENTS

Acknowledgements iii
Abstract v
Published Content and Contributions vi
Table of Contents vii
List of Illustrations viii
List of Tables xvii
Chapter I: Introduction 1
Chapter II: Impacts of traffic reductions associated with COVID-19 on Southern California air quality 7
2.1 Introduction 8
2.2 Methods and Data 9
2.3 Results and Discussion 11
Chapter III: Inferring the vertical distribution of CO and CO_2 from TCCON total column values using the TARDISS algorithm 27
3.1 Introduction 28
3.2 Methods 31
3.3 Results and Discussion 53
3.4 Conclusions 77
Chapter IV: Assessing surface fluxes of carbon dioxide using a novel remote-sensing dataset 86
4.1 Introduction 86
4.2 Methodology and Data 88
4.3 Results and Discussion 92
4.4 Conclusions and Future Work 98
Chapter V: Outlook 103
Appendix A: Supplemental Information for impacts of traffic reductions associated with COVID-19 on Southern California air quality 108
Appendix B: Supplemental Information for Inferring the vertical distribution of CO and CO_2 from TCCON total column values using the TARDISS algorithm 122
Appendix C: Supplemental Information for Assessing surface fluxes of carbon dioxide using a novel remote-sensing dataset 133

LIST OF ILLUSTRATIONS

Number *Page*

2.1 a) Box plot of the basin-maximum 24-hr $PM_{2.5}$, 8-hr daily maximum O_3, and 1-hr daily maximum NO_x during the COVID-19 period (19 March to 30 June) in 2020 and in the past five years (2015-2019) in the South Coast Air Basin. Horizontal lines inside boxes denote median values, edges of box denote the 25th and 75th percentiles, and the whiskers denote ±1.5×IQR. Dots are data points > 1.5×IQR. The confidence diamond in each box contains the mean and the upper and lower 95% of the mean. The means are reported to the right of the box plots with the standard deviation in parenthesis. b) 7-day moving average of basin-maximum 24-hr $PM_{2.5}$, 8-hr daily maximum O_3, and 1-hr daily maximum NO_x in 2020 and in the past five years in the South Coast Air Basin. c) (Left) Basin-wide daily average traffic flow deviation from January to February in percent is plotted with the 7-day moving average represented by the red line. (Right) Average difference from January to February traffic levels for 19 March to 30 June period separated by the source/receptor area for the South Coast Air Basin. 14

2.2 Middle panel: Map of the tropospheric NO2 column as measured by the TROPOMI instrument for the 19 March to 30 June, 2020 period with color indicated by the bar to the right of the map. The locations of each air quality monitoring site are denoted by circles color coded (excluding the West LA site) by the difference between the 2020 afternoon NO2 values and the value expected by the 2000 to 2019 trend in afternoon NO2 in percent. Surrounding Panels: Time series plots of NO2, O3, and Ox in ppb for each site for the 19 March to 30 June period from 2000 to 2020. The dotted lines show the exponential fit for each species. The grey dotted lines represent the standard deviation of the residuals between the measured values of NO2 and the fit. Values for 2020 are represented by asterisks. The difference between the average afternoon values of NO2, O3, and Ox in our analysis period in 2020 and the long-term trend is noted within each individual plot in percent.....17

2.3 Left: Hourly afternoon COVID period O_x concentrations are plotted against temperature and color coded by NO_2, all in ppb. The grey

boxes are CalNex O_x concentrations in ppb. Middle: Hourly afternoon COVID period CH_2O column abundances, in molecules per square centimeter, are plotted against temperature and color coded by O_3. The grey boxes are CalNex CH_2O concentrations in ppb and follow the right y-axis. Right: Afternoon COVID period $PM_{2.5}$ concentrations are plotted against temperature and are color coded by NO_z. The grey boxes are PM_1 concentrations from CalNex measurements. All data shown here is from Pasadena. In the left and middle panels, the upper and lower black lines are the 10% and 90% quantile values for the COVID period from 2015 to 2019 values, respectively. 19

3.1 Vertical sensitivities of the total column retrievals from GFIT used in our algorithm for both CO_2 (left column) and CO (right column) plotted against pressure normalized to the surface and color coded by the solar zenith angle (SZA). A column averaging kernel greater than 1 means that the total column is more sensitive to molecules at this pressure level than the average sensitivity. For example, if we move some of the CO_2 molecules from 200 hPa to the surface in our a priori profile, the retrieved total column and scale factor (VSF) will decrease for the 6073 cm^{-1} window and increase for the 4852 cm^{-1} window while the true and a priori total columns remain unchanged. The 6220 and 6339 cm^{-1} CO_2 and 2160 and 2111 cm^{-1} CO windows have near-identical kernels due to the CO_2 bands being almost identical in their line strengths, separations, widths, and temperature dependences. The 6339 cm^{-1} CO_2 is represented by black dashed lines behind the dotted lines representing the 6220 cm^{-1} sensitivities and the 2111 cm^{-1} CO is represented by black dashed lines behind the dotted lines representing the 2160 cm^{-1} sensitivities. 33

3.2 Flowchart illustrating the steps performed by of the TARDISS retrieval. The input to the TARDISS retrieval is the output of the spectral fitting done by the GGG2020 software suite represented by the green row. The setup of the components of the TARDISS algorithm from the output of the TCCON spectral fits is shown in Equations 3.11 through 3.14 and in the middle row. The TARDISS retrieval is performed using Equation 3.16, the output partial column DMF values are calculated using Equation 3.17, and the information content is calculated by Equation 3.18 and 3.19 as shown in the bottom row. 35

3.3 Example of an a priori covariance matrix color coded by the magnitude of the value. The axes represent the relationship of the contribution of each measurement to each partial column and each other measurement. The upper right and lower left quadrants are dark blue and represents zero assumed correlation between the upper and lower partial columns over a day of measurements. The diagonal is scaled to constrain the fit and the lower right quadrant shows the assumed correlation between upper partial column scalar values over a day of measurement. The lower partial column has an a priori covariance that is a scaled identity matrix, the upper partial column has an a priori covariance that decays over one third of the measurement day, and the cross covariances between the upper and lower partial columns are assumed to be zero. 47

3.4 An example of the profiles used in the direct comparison calculations using data from the Park Falls site on July 27, 2018. The profile above 10 km is not shown. The solid black line is the TCCON a priori profile scaled by the median of the vertical scaling factors from the spectral windows used. The green dot-dashed line is the measured AirCore mole fraction. The red, dashed line is the AirCore measurements interpolated to the vertical spacing of the TCCON prior, and the blue, dotted line with circles is the smoothed, vertical sensitivity weighted profile that is integrated to calculate the partial column that the TARDISS retrieval would calculate if it had a 'true,' AirCore profile. The black dots within the blue circles represent the points of the profile that make up the lower partial column.....53

3.5 The direct comparisons between the partial column DMF values retrieved from the TARDISS fit and the integrated, smoothed in situ partial columns for CO_2 (a,b) and the CO (c,d) for the lower (a,c) and upper (b,d) columns. The CO_2 comparisons are color coded by site and the CO comparisons are solely from the Lamont site. The error bars in the x-direction are the reported errors from the aircraft data smoothed the same way as the in situ measurements and the error bars in the y-direction are the output errors from the TARDISS fit scaled by the VEM values. The black solid line is the 1-1 line and the blue dot-dash line is the linear fit of the data with the y-intercept forced through zero. The blue dot-dash line for the lower partial column CO fit is overlapping with the solid black line. The slopes

of the partial column validation of the TCCON spectral windows used in the retrieval are represented by dashed lines. 61
3.6 East Trout Lake site direct comparisons between the partial column DMF values retrieved from the TARDISS fit and the integrated, smoothed aircraft partial columns for lower column CO_2 and CO. The error bars in the x-direction are the integrated partial columns of the profile shifted by the error values and then subtracted from the original partial column integration. The error bars in the y-direction are the output errors from the TARDISS fit scaled by the VEM value for the site. The black solid line is the 1-1 line and the blue dot-dash line is the linear fit of the data with the y-intercept forced through zero. The slope for the fit is 1.001±0.002 for CO_2 and is 0.945±0.012 for CO. 63
3.7 Lamont site direct comparisons between the partial column DMF values retrieved from the TARDISS fit and the integrated, smoothed airborne partial columns for lower column CO_2 and CO. The error bars in the x-direction are the integrated partial columns of the profile shifted by the error values and then subtracted from the original partial column integration. The error bars in the y-direction are the output errors from the TARDISS fit scaled by the VEM value for the site. The black solid line is the 1-1 line and the blue line is the linear fit of the data with the y-intercept forced through zero. The slope for the fit is 1.002±0.001 for CO_2 and is 1.000±0.002 for CO.65
3.8 Vertical sensitivities of the lower partial column (left column) and upper partial column (right column) scalars color coded by solar zenith angle in degrees. The sensitivities calculated when using a temporally covariant a priori covariance matrix are shown in the top row and when using a non-temporally covariant a priori covariance matrix are shown in the bottom row. 68
3.9 The same comparison shown in Fig. 3.7 is shown here without error bars and color coded by the DoF per measurement for the comparison day retrieval. The blue dot-dash line above the black 1-to-1 line is the linear fit of the data with the y-intercept forced through zero with a slope of 1.002±0.001. 74
3.10 Time series plot of the monthly median lower (top) and upper (bottom) partial column values of CO_2 in ppm for the five sites used in the work from 2012 (or the start of measurement) to the end of 2021. Data from before 2012 measured in Park Falls and 2011 in

Lamont are not used due to instrument alignment issues and laser issues. 76
3.11 Time series plot of the monthly median lower (top) and upper (bottom) partial column values of CO in ppb for the three sites used in the work that have the InSb detector from 2017 to the end of 2021. CO has been declining in most of the US cities due to emissions control technologies 76
4.1 Selected time series of daily average TARDISS upper (top panel) and lower (bottom panel) partial column CO2 (left axis, blue circles) and the free tropospheric temperature (right axis, black squares) at the Park Falls, WI, TCCON detrended using a 30-day moving mean. 89
4.2 Monthly aggregated estimates of $Flux_{FTS}$ and the NEE calculated from in situ measurements (Tower NEE) color-coded by the lower partial column water column and sized by the number of days measured in each month. The blue dashed line represents the linear fit between the two measurements of NEE. The grey ellipses represent the errors in the x- and y-direction to one standard deviation. The solid diagonal black line is the 1-1 comparison line, and the solid vertical and horizontal lines are at the values of zero for the tower and FTS NEE, respectively 94
4.3 Direct comparison of the monthly aggregations of the TARDISS derived $Flux_{FTS}$ and the storage fluxes (left panel), eddy covariance fluxes (right panel), and total NEE fluxes (middle panel) reported from the 396m level of the tall tower color-coded by the lower partial column water column and sized by the number of days measured in each month. The blue dashed lines represent the linear fit between the data. The grey ellipses represent the errors in the x- and y-direction to one standard deviation. The solid diagonal black line is the 1-1 comparison line, and the solid vertical and horizontal lines are at the values of zero for the tower and FTS fluxes, respectively 95
4.4 Histogram of the daily $Flux_{FTS}$ values measured at the Park Falls and Armstrong TCCON sites....97
A.1 Left: 7-day moving average temperature (top), relative humidity (middle), and wind speed (bottom) in 2020 and 2015 to 2019 in the South Coast Air Basin. For 2020, measurements before 19 March are in green and after 19 March are in red. The averages of the measurements for 2015 to 2019 are in black with the associated

range as grey shading. Right: Monthly average precipitation in the South Coast Air Basin in 2020 and 2015 to 2019 in centimeters per month. 108
A.2 Left: Breakdown of monitoring sites and the measurements included in the analysis. Right: Map of the locations of the sites described in the table on the left. 109
A.3 Plots of mean O_3 concentrations by hour of day and day of week in Pasadena for our analysis period in 2020 and the average of 2015 to 2019. Vertical lines mark 12pm and 4pm respectively in each plot 110
A.4 Air quality index time series for daily AQI values for LA county for 2010 to 2020 generated on the EPA website (https://www.epa.gov/outdoor-air-quality-data/air-data -multiyear-tile-plot).....111
A.5 Air quality index time series for daily AQI values for San Bernardino County for 2010 to 2020 generated on the EPA website (https://www.epa.gov/outdoor-air-quality-data/ air-data-multiyear-tile-plot).....112
A.6 Air quality index time series for daily AQI values for Riverside County for 2010 to 2020 generated on the EPA website (https://www.epa.gov/outdoor-air-quality-data/ air-data-multiyear-tile-plot).....113
A.7 Air quality index time series for daily AQI values for Orange County for 2010 to 2020 generated on the EPA website (https://www.epa.gov/outdoor-air-quality-data/ air-data-multiyear-tile-plot).....114
A.8 Sensitivity test by excluding the rainy days from the analysis (right, in red) in comparison to including all the days (left, in black). The means are reported to the right of the box plots with the standard deviation in parenthesis.....115
A.9 Left: Box plots of 8-hr DM O_3 values during the 2015 to 2019 COVID period and 2020 COVID period. Right: Map of the difference between the 2015 to 2019 COVID period and 2020 COVID period in parts per billion (top) and percentage (bottom) ..116
A.10 Left: Box plots for 1-hr daily maximum NO_X values during the 2015 to 2019 COVID period and 2020 COVID period. Right: Map of the difference between the 2015 to 2019 COVID period and 2020 COVID period in parts per billion (top) and percentage (bottom) ..116
A.11 Left: Box plots for 24-hr $PM_{2.5}$ values during the 2015 to 2019 COVID period and 2020 COVID period. Right: Map of the

difference between the 2015 to 2019 COVID period and 2020 COVID period in μg m^{-3} (top) and percentage (bottom) 117
A.12 Left: Box plots for the column CH_2O concentrations for the COVID period for 2015 to 2019 and for 2020. Right: Time series of the yearly COVID period CH_2O concentrations. Error bars represent the standard error in the mean 118
A.13 Left: Box plots for the Pasadena temperature measurements for the COVID period for 2015 to 2019 and for 2020. Right: Time series of the yearly COVID period temperature measurements. Error bars represent the standard error in the mean. 118
A.14 Hourly afternoon O_3 concentrations are plotted against temperature and color coded by NO_2, all in ppb. The grey boxes are CalNex O_3 concentrations in ppb. All data shown here is from Pasadena. In the left and middle panels, the upper and lower black lines are the 10% and 90% quantile values for the 2015 to 2019 values, respectively 119
A.15 Left: Box plots for weekend(red) and weekday(blue) 1-hr daily maximum NO_X for the COVID period in 2020 and 2015 to 2019. Right: Difference between weekend and weekday 1- hr daily maximum NO_X for the COVID period in 2020 and 2015 to 2019 in parts per billion(top) and percent(bottom). Error bars represent the standard error in the mean.....120
A.16 Left: Box plots for weekend(red) and weekday(blue) 8-hr daily maximum O_3 for the COVID period in 2020 and 2015 to 2019. Right: Difference between weekend and weekday 8-hr daily maximum O_3 for the COVID period in 2020 and 2015 to 2019 in parts per billion(top) and percent(bottom). Error bars represent the standard error in the mean.....120
B.1 Errors in the retrieval of CO_2 from the midday total column measurement at the Park Falls site on July 18, 2018 using the MAP method outlined by Equation 3.13 and the least squares method outlined by Equation 3.12. The blue circles represent the error in the lower partial column and the orange asterisks represent the error in the upper partial column. Note the difference in the range of the y axis in the left and right plots both of which are in parts per million. The x axis indicates the number of points included in the overall fit with zero additional points representing the retrieval of a single spectrum 125

B.2 Same as Fig. B.1, except the a priori covariance is removed from the MAP retrieval.....126
B.3 The direct comparisons between the total column DMF values retrieved from the TARDISS fit and the integrated, smoothed in situ partial columns for CO_2 (left) and the CO (right). The black solid line is the 1-1 line and the blue dot-dash line is the linear fit of the data with the y-intercept forced through zero. The slopes of the partial column validation of the TCCON spectral windows used in the retrieval are represented by dashed lines 128
B.4 Monthly mean lower partial column scalar errors plotted for CO_2 (top) and CO (bottom). 129
B.5 Monthly mean lower partial column errors plotted for CO_2 in ppm (top) and CO in ppb (bottom). 130
B.6 Monthly mean upper partial column errors plotted for CO_2 in ppm (top) and CO in ppb (bottom). 130
B.7 Comparison Validation Error Multiplier (VEM) and number of comparison days plotted by the minimum DoF per measurement filter applied to the comparison data. The retrieved data is in comparison with in situ data measured as a part of the NOAA GGGRN (Global Greenhouse Gas Reference Network) Aircraft sites from 2008 -2018 at the Lamont measurement site 131
B.8 Example of one day of TCCON retrievals of total column CO (top) from two different spectral windows (4233 in blue and 2160 in orange) above the TARDISS partial column retrievals for CO (lower partial column in red dots, upper partial column in black dots) for the same day (bottom).....132
C.1 Monthly comparisons of daily average TARDISS upper partial column CO_2 (y-axis) and the free tropospheric temperature (x-axis) at the Park Falls, WI, TCCON detrended using a 30-day moving mean. The dashed blue line is the linear fit of the data. The solid black line is the same slope between each panel as a visual aid. Panel titles represent the month of the year with “1” representing January and “12” representing December 133
C.2 Same as Fig. C.1 for the lower partial column values.....134
C.3 Selected time series of hourly average TARDISS upper (top panel) and lower (bottom panel) partial column CO_2 (left axis, blue circles) and the reported three-hourly values of free tropospheric temperature (right axis, black squares) at the Park Falls, WI, TCCON detrended using a 30-day moving mean.....134

C.4 Same as Fig. 4.3 for the 120m measurement level on the tower.... 135
C.5 Same as Fig. 4.3 for the 30m measurement level on the tower.....135
C.6 Histogram of the daily $Flux_{FTS}$ values measured at the Armstrong TCCON site during the Winter (DJF) and Summer (JJA).....136

LIST OF TABLES

Number *Page*

3.1 Location, dates of measurement, and DOIs of the TCCON sites used in this work. CO measurements require an InSb detector to cover the 2160 and 2111 cm-1 windows, which has only been available since 2017 at Caltech, Lamont, and East Trout Lake 51

3.2 Variations in CO_2 retrieval upper and lower column validation slopes, upper and lower column mean ratio deviations, upper and lower column comparison errors, and DoF for different TARDISS a priori choices and a priori covariance matrix scaling values. The asterisk in the fourth row indicates that this is the operational set of parameter choices for the CO_2 retrieval.....57

3.3 Variations in CO retrieval upper and lower column validation slopes, upper and lower column mean ratio values, upper and lower column comparison errors, and DoF for different TARDISS a priori choices and a priori covariance matrix scaling values. The asterisk in the second to last row indicates that this is the operational set of parameter choices for the CO retrieval. 59

3.4 Comparisons of the TARDISS partial column retrieval to the partial column comparisons of the fits of the TCCON spectral windows from TCCON used as input for the TARDISS algorithm. The data in the TARDISS row uses the operational parameters for the fit that are identified in Table 3.2 and 3.3 by an asterisk 62

3.5 Validation comparison DoF, error, validation slope and mean ratio deviation and site VEM values for lower and upper column CO_2 for retrievals using a temporally constrained upper column and a temporally unconstrained upper column. The retrievals are performed with the operational parameters denoted by asterisks in Table 3.2 66

3.6 Errors in the CO and CO_2 lower partial column retrievals of each site shown as the average of the entire data time series and broken down into total retrieval error, retrieval noise, smoothing error, validation error multiplier, and total error. The values for total retrieval error and total error represent one standard deviation. 71

3.7 Degrees of freedom per measurement (and per day) for the lower column, upper column, and total retrieval, in addition to the

Shannon information content separated by site for the CO and CO_2 retrievals.....73
A.1: 2000 to 2019 trends and 2020 anomalies in afternoon (12:00 - 16:00 local) NO_2, O_3, and O_X concentrations for sites in the basin that have measurements of both NO_2 and O_3 for the 2000 to 2020 period. Anomalies represent the difference between values observed during 2020 COVID period afternoons and the values expected from a 2000-2019 fit of COVID period afternoons. Values in parentheses represent the anomaly values for the 19 April to 30 June period instead of the 19 March to 30 June period.....109
B.1 Table of variable names, descriptions, and defining equation for all the variables used in the work.....122
B.2 Site, measurement type, species, campaign or program, citation, and dates of the in situ profile data used in this work 127
B.3 Comparisons of the TARDISS total column retrieval to the total column comparisons of the fits of the TCCON spectral windows used as input for the TARDISS algorithm. The data in the TARDISS row uses the operational parameters for the fit that are identified in Table 3.2 and 3.3 by an asterisk.....128
B.4 DoF, comparison slopes, VEM, and total errors in the CO and CO_2 lower partial column retrievals for the long term comparisons performed at the Lamont and East Trout Lake sites. The values for total retrieval error and total error represent one standard deviation.129
C.1 Comparison statistics of the monthly values of the TARDISS-derived surface fluxes and in situ, tower estimated NEE, storage, and eddy covariance fluxes at 30, 120, and 396 meters.....137
C.2 Statistics of the TARDISS-derived surface fluxes for the Armstrong and Park Falls TCCON sites for overall yearly, summer, and winter data.....138

Chapter 1

INTRODUCTION

Remote sensing is a powerful tool for measuring atmospheric species. Species related to climate and air quality such as carbon dioxide (CO_2) and carbon monoxide (CO) are remotely measured both from the ground and from space to better understand anthropogenic and biogenic climate drivers and enhance our ability to model the world around us (Crisp et al., 2017; Eldering et al., 2019; Wiacek et al., 2007; Wunch et al., 2011). Measurements made by ground-based Fourier transform spectrometers (FTSs) as a part of the Total Carbon Column Observation Network (TCCON) are used to validate measurements from space-based instruments as well as expand our knowledge of the carbon cycle (Wunch et al., 2011). TCCON reports total column (defined as the surface to the top of the atmosphere) dry mole fraction (DMF) values for an array of atmospheric species that are then calibrated to the World Meteorological Organization (WMO) standard by comparison with in situ vertical profile measurements.

TCCON uses a nonlinear, least-squares algorithm, called GFIT, to minimize the errors in the difference between a spectrum derived from a forward radiative transfer model and a spectrum of sunlight measured by the FTS. Each spectrum is split into spectral regions (also called windows) to isolate absorption features from a particular atmospheric species of interest. The GFIT algorithm retrieves a single scaling factor which it applies to an a priori vertical profile for each species. The a priori profiles are then vertically integrated and scaled by the retrieved scaling factor to get the a posteriori total column values. These values are converted to DMF by dividing by the column of dry air computed from the total column value of O_2 retrieved from the same spectra. Under optimal conditions, retrieved total column DMF values are reported roughly every three minutes during the day.

Retrievals obtained from different spectral windows have different sensitivities to different parts of the atmosphere. These sensitivities are referred to as averaging kernels and are

solar zenith angle dependent column vectors for the scaled priors retrieved by TCCON. The sensitivity, or lack thereof, to changes at different altitudes is the result of the spectral properties of the window. For example, since information about the stratosphere comes from the near the center of a spectral absorption line as a result of diminished collisional broadening, optically thin windows tend to be more sensitive to changes in the upper troposphere and stratosphere. If the absorption line center is saturated due to absorption in the lower atmosphere, the spectrum will not have much information from the stratosphere and will be less sensitive to stratospheric changes.

Profile retrievals have been explored using TCCON spectra in individual windows, but a method to combine the information from different spectral windows has yet to be developed (Connor et al., 2016; Kuai et al., 2012; Roche et al., 2021). Profile retrievals from TCCON spectra have been shown to theoretically have roughly three degrees of freedom meaning three pieces of vertical information could be retrieved from a spectrum but the retrievals are subject to nonphysical results and oscillation due to errors in spectroscopy and a priori meteorology, particularly temperature (Connor et al., 2016; Roche et al., 2021).

In Chapter 3, we describe a new algorithm, the Temporal Atmospheric Retrieval Determining Information from Secondary Scaling, or TARDISS, that enables retrieval of vertical information about the distribution of trace gases from TCCON data. Instead of fitting the spectra directly, we fit the differences in the total column DMF values obtained from different spectral bands with different vertical sensitivities by performing a secondary scaling of two partial columns of the atmosphere. This algorithm takes advantage of previous efforts to carefully calibrate the total column retrievals against WMO-scale in situ observations.

Similar to the spectral fitting, we use the maximum a posteriori (MAP) method described in Rodgers, 2008, that returns a scaling factor that maximizes the posterior probability distribution. In the spectral fitting performed by GFIT, this returns the optimal scaling

factor of the prior profile that minimizes the errors between the measured and modeled spectrum. In our new algorithm, this returns the optimal scaling factors for a partial column near the surface (0-2 km) and one above (2-70 km) that minimizes the differences between the total column DMF values retrieved from different spectral windows and a new total column DMF calculated by scaled partial columns. This eliminates the need to fit spectra directly by utilizing the information already retrieved by GFIT. This method also allows us to use a priori information to further inform the secondary scaling.

Aside from not directly fitting the spectra directly, the key component of the TARDISS algorithm is that it simultaneously fits data obtained over an entire day of measurement instead of one spectrum at a time. Utilizing the temporal dimension takes advantage of improving the signal-to-noise by joint retrieval of many observations compared to traditional profile retrievals obtained from each spectra. It also, and possibly more importantly, allows for the use of temporal a priori information meaning that we can constrain the retrieval based on our understanding and expectation of the behavior of the atmosphere over the day. This aspect of the algorithm has the greatest potential for further study and could be useful in improving the algorithm in the future.

This algorithm provides new information about surface mixing ratios of CO_2 and CO from TCCON stations around the world. The InGaAs detector measures the spectral windows used for the retrieval of CO_2 partial columns. These detectors are standard to the instrumentation so that ~30 sites worldwide can retrieve partial column CO_2 values. The InSb detector is critical for retrieval of CO partial columns as it provides access to spectral windows with sensitivity peaked near the surface; however, this detector requires liquid nitrogen cooling and is only being used in a smaller subset of TCCON sites. Overall, this means that there are decades of data to process with TARDISS providing many new avenues of scientific study. This new approach and data could be useful for finding ways to improve the total column retrievals, finding ways to improve the TARDISS algorithm, performing new carbon cycle studies, or even reexamining previous studies with partial column data.

In Chapter 4, we use the partial column CO_2 data retrieved by TARDISS to examine the surface fluxes at the Park Falls, Wisconsin TCCON site using methodology adapted from a study that used total column measurements (Keppel-Aleks et al., 2012). Estimations of carbon fluxes are used to understand the influence of the biosphere on the climate and to inform climate models. For these reasons, having remote estimations of surface fluxes that are more directly sensitive to the surface would be ideal. It is difficult to make estimations of fluxes of CO_2 using remote sensing measurements (Keppel-Aleks et al., 2012; Torres et al., 2019). Changes in CO_2 due to surface fluxes can be small compared to synoptic and seasonal variability. Furthermore, total column measurements can be less sensitive to the surface as influences from the surface are integrated in the column. Our goal is to better understand the influences of the biosphere on the uptake of carbon and to understand influences and biases on TARDISS-derived flux estimations.

Chapter 2 focuses on in situ air quality measurements with support from remotely sensed measurements of formaldehyde. The South Coast Air Basin (SoCAB) in Southern California is known for having poor air quality, due to the combination of emissions and unique meteorological conditions, that has been improving over the past 70 years (Parrish et al., 2016; Pollack et al., 2013). Reducing vehicular emissions through local and state legislature has been the primary method to improve air quality and the reduction of vehicular travel during the COVID-19 lockdown resulted in an unintentional natural experiment of the effects of a step change in vehicular emissions. Overall, we found that the long-term assumptions of photooxidation in SoCAB will change and need to be reexamined as there are further decreases in vehicular emissions and the proportional influence of other emission sources grows.

CO is a useful tool for understanding air quality since it is long-lived (compared to some other pollutants) and is related to both vehicular emissions and the oxidation of volatile organic compounds (VOCs). The exploration of the change in emissions in Chapter 2 offers motivation for the use of the TARDISS-retrieved partial column CO values using the

TCCON measurements made in Pasadena, CA to examine changes in air quality over the past six years.

The chapters of this work are presented in the order they were written. Chapter 2 serves as the motivation for future uses of the TARDISS lower partial column CO data, particularly from urban sites like the Pasadena, CA TCCON site. Chapter 3 describes the methodology and validation of the TARDISS algorithm. Chapter 4 explores the use of the TARDISS partial column CO_2 data to estimate surface fluxes. Finally, Chapter 5 outlines directions for future research related to improving the TARDISS retrievals and possible uses of the new partial column data for scientific study. The supplemental information for Chapters 2, 3, and 4 can be found in Appendix A, B, and C, respectively.

References

Connor, B. J., Sherlock, V., Toon, G., Wunch, D., and Wennberg, P. O.: GFIT2: an experimental algorithm for vertical profile retrieval from near-IR spectra, Atmospheric Measurement Techniques, 9, 3513–3525, https://doi.org/10.5194/amt-9-3513-2016, 2016.

Crisp, D., Pollock, H. R., Rosenberg, R., Chapsky, L., Lee, R. A. M., Oyafuso, F. A., Frankenberg, C., O'Dell, C. W., Bruegge, C. J., Doran, G. B., Eldering, A., Fisher, B. M., Fu, D., Gunson, M. R., Mandrake, L., Osterman, G. B., Schwandner, F. M., Sun, K., Taylor, T. E., Wennberg, P. O., and Wunch, D.: The on-orbit performance of the Orbiting Carbon Observatory-2 (OCO-2) instrument and its radiometrically calibrated products, Atmos. Meas. Tech., 10, 59–81, https://doi.org/10.5194/amt-10-59-2017, 2017.

Eldering, A., Taylor, T. E., O'Dell, C. W., and Pavlick, R.: The OCO-3 mission: measurement objectives and expected performance based on 1 year of simulated data, Atmos. Meas. Tech., 12, 2341–2370, https://doi.org/10.5194/amt-12-2341-2019, 2019.

Keppel-Aleks, G., Wennberg, P. O., Washenfelder, R. A., Wunch, D., Schneider, T., Toon, G. C., Andres, R. J., Blavier, J.-F., Connor, B., Davis, K. J., Desai, A. R., Messerschmidt, J., Notholt, J., Roehl, C. M., Sherlock, V., Stephens, B. B., Vay, S. A., and Wofsy, S. C.: The imprint of surface fluxes and transport on variations in total column carbon dioxide, Biogeosciences, 9, 875–891, https://doi.org/10.5194/bg-9-875-2012, 2012.

Kuai, L., Wunch, D., Shia, R.-L., Connor, B., Miller, C., and Yung, Y.: Vertically constrained CO2 retrievals from TCCON measurements, Journal of Quantitative Spectroscopy and Radiative Transfer, 113, 1753–1761, https://doi.org/10.1016/j.jqsrt.2012.04.024, 2012.

Parrish, D. D., Xu, J., Croes, B., and Shao, M.: Air quality improvement in Los Angeles—perspectives for developing cities, Frontiers of Environmental Science & Engineering, 10, 1–13, https://doi.org/10.1007/s11783-016-0859-5, 2016.

Pollack, I. B., Ryerson, T. B., Trainer, M., Neuman, J. A., Roberts, J. M., and Parrish, D. D.: Trends in ozone, its precursors, and related secondary oxidation products in Los Angeles, California: A synthesis of measurements from 1960 to 2010: OZONE TRENDS IN LA FROM 1960 TO 2010, Journal of Geophysical Research: Atmospheres, 118, 5893–5911, https://doi.org/10.1002/jgrd.50472, 2013.

Rodgers, C. D.: Inverse methods for atmospheric sounding: theory and practice, Repr., World Scientific, Singapore, 240 pp., 2008.

Torres, A. D., Keppel-Aleks, G., Doney, S. C., Fendrock, M., Luis, K., De Mazière, M., Hase, F., Petri, C., Pollard, D. F., Roehl, C. M., Sussmann, R., Velazco, V. A., Warneke, T., and Wunch, D.: A Geostatistical Framework for Quantifying the Imprint of Mesoscale Atmospheric Transport on Satellite Trace Gas Retrievals, JGR Atmospheres, 124, 9773–9795, https://doi.org/10.1029/2018JD029933, 2019.

Wiacek, A., Taylor, J. R., Strong, K., Saari, R., Kerzenmacher, T. E., Jones, N. B., and Griffith, D. W. T.: Ground-Based Solar Absorption FTIR Spectroscopy: Characterization of Retrievals and First Results from a Novel Optical Design Instrument at a New NDACC Complementary Station, J. Atmos. Oceanic Technol., 24, 432–448, https://doi.org/10.1175/JTECH1962.1, 2007.

Wunch, D., Toon, G. C., Blavier, J.-F. L., Washenfelder, R. A., Notholt, J., Connor, B. J., Griffith, D. W. T., Sherlock, V., and Wennberg, P. O.: The Total Carbon Column Observing Network, Philosophical Transactions of the Royal Society A: Mathematical, Physical and Engineering Sciences, 369, 2087–2112, https://doi.org/10.1098/rsta.2010.0240, 2011.

Chapter 2

IMPACTS OF TRAFFIC REDUCTIONS ASSOCIATED WITH COVID-19 ON SOUTHERN CALIFORNIA AIR QUALITY

Parker, H. A., Hasheminassab, S., Crounse, J. D., Roehl, C. M., and Wennberg, P. O.: Impacts of Traffic Reductions Associated With COVID-19 on Southern California Air Quality, Geophysical Research Letters, 47, https://doi.org/10.1029/2020GL090164, 2020.

Abstract

On 19 March 2020, California put in place Stay-At-Home orders to reduce the spread of SARS-CoV-2. As a result, decreases up to 50% in traffic occurred across the South Coast Air Basin (SoCAB). We report that, compared to the 19 March to 30 June period of the last five years, the 2020 concentrations of $PM_{2.5}$ and NO_x showed an overall reduction across the basin. O_3 concentrations decreased in the western part of the basin and generally increased in the downwind areas. The NO_x decline in 2020 (approximately 27% basin-wide) is in addition to ongoing declines over the last two decades (on average 4% less than the -6.8% per year afternoon NO_2 concentration decrease) and provides insight into how air quality may respond over the next few years of continued vehicular reductions. The modest changes in O_3 suggests additional mitigation will be necessary to comply with air quality standards.

Plain Language Summary

On 19 March 2020, California put in place Stay-At-Home orders to reduce the spread of SARS-CoV-2. As a result, there was much less traffic in Southern California. Reduced traffic along with a month-long stretch of unusually rainy weather at the beginning of the lockdown led to significant reductions in $PM_{2.5}$ and NO_x levels across the basin. Concentrations of O_3, on the other hand, showed inconsistent changes across the basin. The response of O_3 to these large changes in nitrogen oxide concentrations suggests

mitigation efforts beyond those associated with continuing vehicle emission reductions will be important to meet clean air goals.

2.1 Introduction

As restrictions were enacted to slow the spread of SARS-CoV-2, the virus that causes COVID-19, the decrease in human activity (traffic, industry, etc) in major cities worldwide resulted in significant changes in air quality. Cities in China, Italy, Germany, and the United States have shown decreases in atmospheric nitrogen dioxide (NO_2) concentrations (Bauwens et al., 2020; Goldberg et al., 2020; Naeger & Murphy, 2020). In Pittsburgh, Pennsylvania, for example, significant decreases in concentrations of NO_2, carbon monoxide (CO) and fine particulate matter ($PM_{2.5}$) have been observed (TanzerGruener et al., 2020). Los Angeles (LA), known for its car culture and multidecadal fight with air pollution (Parrish et al., 2016; Pollack et al., 2013), was reported to have some of the cleanest air in its history as a result of the sudden drop in traffic emissions (https:// www.latimes.com/opinion/story/2020-04-22/coronavirus-is-making-it-clear-that-car-culture-is-its-own-kind-of-plague). For LA and the broader South Coast Air Basin (SoCAB), however, the COVID-19 restrictions coincided with precipitation at least three times the historical average (Figure A.1). As the anomalously rainy period ended in the SoCAB, the levels of the secondary pollutant ozone (O_3) returned to values comparable or exceeding those of previous years despite the sustained decrease in traffic flow (more than 20% below the values in January and February).

The influence of nitrogen oxide (NO_x) pollution in the SoCAB on air quality has been the subject of a decades-long study. Since the mid-20th century, NO_x in the SoCAB has been decreasing by roughly 3% per year on average (Parrish et al., 2016; Pollack et al., 2013). In the last decade, regulations of NO_x have been focused on reducing the emissions from heavy duty diesel vehicles (Final 2016 Air Quality Management Plan, 2016). Historically, reductions in weekend NO_x emissions have led to higher weekend O_3 levels. Higher weekend O_3 levels are the result of the combination of increased photochemical production

of oxidant ($O_x = NO_2 + O_3$) from elevated OH levels due to the reduced loss of OH via its reaction with NO_2 and an increased fraction of O_x present as O_3 due to the reduced conversion to NO_2 via reaction with NO. This phenomenon is known as the 'weekend effect'. The weekend effect has been used to predict the effects of future NO_x emission reductions on air quality (Baidar et al., 2015). Changes in VOC emissions do not generally scale with NO_x because these emissions are associated with many sectors (and include biogenic emissions). On-road vehicle VOC emissions are now thought to account for only about one fourth of the total emissions (CEPAM: 2016 SIP - Standard Emission Tool, n.d.).

Both the weekend effect and the especially large reductions in vehicular emissions in 2020 provide evidence for the continuing efficacy of mobile fleet emissions reductions on air quality. Given the long-term trends in such emissions, the experience of spring 2020 provides a glimpse of what the air quality will look like approximately five years into the future of vehicle targeted emission reductions.

2.2 Methods and Data

Basin-wide air pollutant data (O_3, NO_2, NO_x, and $PM_{2.5}$) were obtained from the California Air Resources Board (CARB) Air Quality Data Query Tool (https://www.arb.ca.gov/aqmis2/aqdselect.php)(Figure 2.1). The 2020 air quality data are preliminary, unvalidated, and subject to change. Continuous measurements of $PM_{2.5}$ along with trace-gas measurements of CO, SO_2, O_3, NO, NO_2, and NO_y were conducted at the Caltech campus by the Caltech air quality system (CITAQS) using Teledyne instrumentation (Text A.1). While the regulatory NO_2 chemiluminescence measurements are known to include contributions from other nitrogen-containing species due to the non-selectivity of the molybdenum converter (Villena et al., 2012), the chemiluminescence data from the South Coast Air Quality Management District (South Coast AQMD) station in Pasadena (located approximately 400 m south of the CITAQS) agree within a few tenths of a ppb with the optical NO_2 measurements from the CITAQS. Remotely sensed CH_2O total column abundances are provided by the Total Carbon Column Observing Network (TCCON) site in Pasadena (Wunch et al., 2011). Temperature and precipitation data are

taken from meteorological sensors located alongside the CH_2O measurement (tccon-weather.caltech.edu). Historical observations of temperature, relative humidity and wind speed data across the basin were obtained from CARB's Meteorology Data Query Tool and precipitation data were acquired from the National Oceanic and Atmospheric Administration (NOAA). The CITAQS, TCCON site, and meteorological station are all located in or on the Linde Laboratory on the southwest corner of the Caltech campus roughly half a kilometer north of a regulatory air monitoring station in Pasadena, operated by the South Coast AQMD. Our analysis also makes use of O_3, NO_2, CH_2O, $PM_{2.5}$, and weather data from the 2010 CalNex campaign ground site also located on the Caltech campus (https://www.esrl.noaa.gov/csl/projects/calnex/). Basin wide daily traffic counts were obtained from the Caltrans PeMS website (http://pems.dot.ca.gov/). TROPOMI tropospheric NO_2 columns are used for illustrative purposes in Figure 2.2 and follow suggested data quality guidelines (Veefkind et al., 2012).

In our analysis, we use the sum of NO_2 and O_3, also referred to as oxidant (O_x), CH_2O, and $PM_{2.5}$ as metrics of air quality. O_x is conserved with respect to the cycling of NO_2 photolysis to O_3 and NO, and O_3 reacting with NO to reform NO_2. This makes O_x measurements useful as a diagnostic of air chemistry since it is less sensitive to local effects on photochemistry (e.g., local NO emissions reacting with O_3 to form NO_2, or clouds changing the photolysis frequency of NO_2) and is instead driven by overall emissions, losses, and net photochemical O_x production. CH_2O is often used as a proxy for VOC reactivity, especially for the oxidation of small alkenes from both anthropogenic and biogenic sources (Pollack et al., 2012; Zhu et al., 2014; Wolfe et al., 2016). $PM_{2.5}$ is both directly emitted and produced within the atmosphere (secondary), with the latter generally being dominant in the SoCAB. Secondary production of $PM_{2.5}$ arises from NH4, NO_3, and sulfate chemistry and the oxidation of gas-phase VOCs and is the main culprit for low visibility during smog events (Schiferl et al., 2014).

In sections 2.3.1 and 2.3.4, we only consider the air monitoring sites that were active through the entire 2015 to 2020 period. For NO_x and O_3, we consider sites that measure

both of these parameters, while for $PM_{2.5}$ we consider data from all the sites with $PM_{2.5}$ measurements (Figure A.2). In these sections, we report 24-hr $PM_{2.5}$, 8-hr daily maximum (DM) O_3, and 1-hr DM NO_x that have regulatory relevance.

In section 2.3.2, we use data from 13 sites in the basin that have measurements of both NO_2 and O_3 for the 2000 to 2020 period. In section 2.3.3, we focus on data from Pasadena only. In the above-mentioned sections, we focus on data collected during the afternoon hours (12pm to 4pm local) since the afternoons are often the times with maximum values of O_3 or O_x and are therefore the most influential in terms of air quality reporting, such as O_3 exceedances (Figure A.3). For an accurate comparison from year to year, we define the 19 March to 30 June window as the COVID-19 (or simply COVID) period for all comparisons.

2.3 Results and Discussion

2.3.1 The Confluence of Anomalous Weather and COVID-19 Restrictions

On 19 March 2020, the state of California enacted Stay-At-Home orders restricting all non-essential work in order to reduce the spread of COVID-19 (https://www.gov .ca.gov/wp-content/uploads/2020/03/3.19.20-attested-EO-N-33-20-COVID-19-HEALTHORDER.pdf). Eleven days before this order, on 8 March 2020, mobility and traffic started decreasing everywhere in the SoCAB (Figure 2.1, c). By April, SoCAB traffic and mobility dropped to about 50% of the pre-COVID-19 period (January and February, 2020). SoCAB traffic counts slowly recovered from late April through early June and stabilized at about 80% of pre-COVID-19 levels by the end of June (Figure 2.1, c) despite different phases of restrictions. While the traffic flow decreased in all areas of the basin, the average differences varied in different parts of the basin as the western and eastern areas have returned close to pre-COVID-19 values (Figure 2.1, c, right panel). Concurrently, the air quality index (AQI) in the second half of March and beginning of April were consistently ‘green’ and SoCAB citizens enjoyed clean air with high visibility (Figure A.4-A.7). Naturally, this led to the association of the decrease in traffic with clean

air and the condemnation of LA car culture as the culprit for bad air quality (https://www.latimes.com/opinion/story/2020-04-22/coronavirus-is-making-it-clear-that-car-culture -is-its-own-kind-of-plague).

The decrease in traffic and improvement in air quality was also coincident with frequent stormy conditions and above-normal amounts of rainfall. The rainfall in the basin in 2020 was well above that of the past decade with precipitation in March and April over three and five times the average values, respectively (Figure A.1). Rainfall affects air quality by removing pollutants such as nitric acid and $PM_{2.5}$ from the air through wet deposition (Seinfeld & Pandis, 2006). In addition, rainy periods are associated with higher basin ventilation rates, decreasing pollution buildup in the basin. Figure 2.1b shows the basin-maximum concentrations of 8-hr DM O_3, 1-hr DM NO_x, and 24-hr $PM_{2.5}$ for the pre- and post-COVID-19 period in 2020 along with the average values for 2015 to 2019 with the 2020 rainy days shaded in blue. During the rainy period in March and early April, temperatures dropped below the range observed over the previous five years (Figure A.1). During this drop in temperature, the 1-hr DM NO_x and 24-hr $PM_{2.5}$ were consistently lower than the lower limits of the 2015 to 2019 range. The 8-hr DM O_3 concentrations were consistently at the lower end of the 2015 to 2019 range. After the rainy period, temperatures in late April and early May rose above historical values (Figure A.1) and 8-hr DM concentrations of O_3 were highly elevated. In fact, in May 2020, SoCAB experienced 18 days of O_3 exceedance from the federal standard of 70 ppb more than any other year from 2015 to 2019. The spike in O_3 concentrations outside the range of the 2015 to 2019 values in late April and early May is coincident with, and likely partially due to, a similar pattern of higher temperatures and lower wind speeds in the basin (Figure 2.1 and A.1). This return to higher O_3 levels occurred although traffic remained at least 30% lower than pre-COVID levels. After May, however, the temperatures, wind speeds, and O_3 concentrations in the basin returned to values within the range of values observed in 2015-2019. NO_x concentrations remained equal to or lower than the previous five years, and, in June, $PM_{2.5}$ concentrations dropped lower than the lower end of the range of values from the past five years. To assess the impact of rainy days on the observed trends, a sensitivity test was

carried out. When the rainy days are excluded from the analysis, the basin-maximum levels are comparable to the values for the entire window with only a 2.76%, 2.11%, and 0.64% difference between including rainy days and not for 24-hr $PM_{2.5}$, 8-hr DM O_3, and 1-hr DM NO_x respectively (Figure A.8).

The changes in 8-hr DM O_3 concentrations in 2020 were not consistent across the basin (Figure A.9). Compared to the same months in 2015-2019, sites in the western part of the basin generally experienced lower 8-hr DM O_3 concentrations (up to 9 ppb or 22% reduction) while most of downwind areas experienced an overall increase (up to 8 ppb or 15% increase). 24-hr $PM_{2.5}$ and 1-hr DM NO_x showed an overall decrease across the basin (10%-45% and 13%-40% reduction, respectively) (Figure A.10-A.11). As discussed above, while the COVID-19 countermeasures altered pollutant concentrations in Los Angeles, the anomalous weather significantly contributed to the clean air observed in late March and early April.

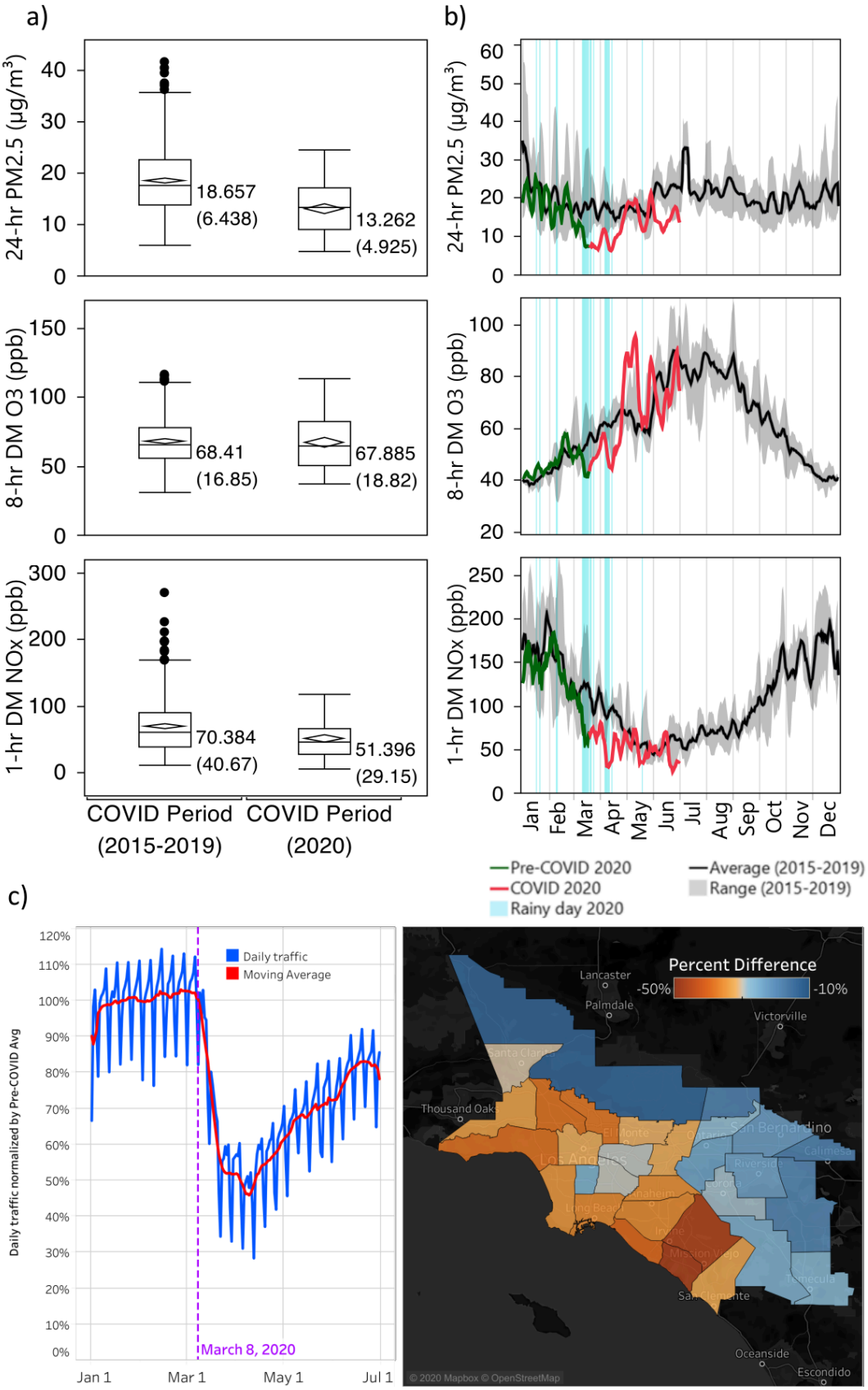
a)
b)
24-hr PM2.5 (µg/m³)
8-hr DM O3 (ppb)
1-hr DM NOx (ppb)
18.657
(6.438)
13.262
(4.925)
68.41
(16.85)
67.885
(18.82)
70.384
(40.67)
51.396
(29.15)
COVID Period
(2015-2019)
COVID Period
(2020)
Jan
Feb
Mar
Apr
May
Jun
Jul
Aug
Sep
Oct
Nov
Dec
Pre-COVID 2020
COVID 2020
Rainy day 2020
Average (2015-2019)
Range (2015-2019)
c)
Daily traffic normalized by Pre-COVID Avg
Daily traffic
Moving Average
March 8, 2020
Jan 1
Mar 1
May 1
Jul 1
Percent Difference
-50%
-10%
Lancaster
Palmdale
Victorville
Thousand Oak
Oceanside
Escondido
© 2020 Mapbox © OpenStreetMap

Figure 2.1: a) Box plot of the basin-maximum 24-hr $PM_{2.5}$, 8-hr daily maximum O_3, and 1-hr daily maximum NO_x during the COVID-19 period (19 March to 30 June) in 2020 and in the past five years (2015-2019) in the South Coast Air Basin. Horizontal lines inside boxes denote median values, edges of box denote the 25th and 75th percentiles, and the whiskers denote ±1.5×IQR. Dots are data points > 1.5×IQR. The confidence diamond in each box contains the mean and the upper and lower 95% of the mean. The means are reported to the right of the box plots with the standard deviation in parenthesis. b) 7-day moving average of basin-maximum 24-hr $PM_{2.5}$, 8-hr daily maximum O_3, and 1-hr daily maximum NO_x in 2020 and in the past five years in the South Coast Air Basin. c) (Left) Basin-wide daily average traffic flow deviation from January to February in percent is plotted with the 7-day moving average represented by the red line. (Right) Average difference from January to February traffic levels for 19 March to 30 June period separated by the source/receptor area for the South Coast Air Basin.

2.3.2 Twenty Years of Reductions and COVID-19

In the context of the trends in air quality in the SoCAB over the past decade, the diverse response of secondary pollutants to the large drops in vehicular emissions during the COVID-19 period is not surprising. Over the past 20 years, vehicular emissions, particularly heavy-duty diesel trucks, have been targeted by regulation and atmospheric concentrations of NO_x have decreased substantially (Final 2016 Air Quality Management Plan, 2016). Figure 2.2 shows the changes in afternoon concentrations of NO_2, O_3, and O_x in sites across the basin since 2000 around a map of tropospheric NO_2 column concentrations for COVID-19 period in 2020 from the TROPOMI instrument. While the 1-hr DM NO_x and 8-hr DM O_3 concentrations have regulatory relevance, the afternoon (i.e., 12:00 to 16:00) values of air pollutants used below are more closely related to the photochemical interactions occurring at peak O_x values.

Over the 2000 to 2019 period, the afternoon NO_2 concentrations have been decreasing at rates between 4.90% and 9.08% per year across the basin (Table A.1). The trends reported here are larger than described elsewhere due to the use of afternoon values instead of the data from the entire day (Pollack et al., 2013; Parrish et al., 2016; Jiang et al., 2018). In terms of O_x, the decreases in NO_2 concentrations have been partially offset by increases in O_3 concentrations due to the nonlinear relationship between NO_2 and O_3 (Fujita et al.,

2016). The trends in afternoon O_3 concentrations vary in different parts of the basin, from decreases of 0.87% to increases of 0.64% per year, while afternoon O_x concentrations have decreased by between 0.39% and 1.53% per year across the basin.

COVID-19 traffic reductions led to an overall drop in atmospheric NO_2 concentrations in Los Angeles similar to those seen in other major cities around the world (Bauwens et al., 2020; Goldberg et al., 2020; Le et al., 2020; Naeger & Murphy, 2020; Tanzer-Gruener et al., 2020). Depending on the location in the basin, afternoon NO_2 concentrations for 2020 were up to 33% lower than those expected using the trend between 2000 and 2019; in several remote locations, NO_2 levels were actually larger than expected in 2020 (Table A.1). For example, COVID period afternoon NO_2 values in Reseda in 2020 were even lower than the expected 5.7% yearly decrease by 33% or 1.3 ppb. Changes in afternoon O_3 are modest and of both signs (decreases of up to 13% or 6.5 ppb and increases as large as 16% or 8.6 pbb). Half of the sites (West LA, Pasadena, Azusa, Glendora, Pomona, Banning, and San Bernardino) have anomalies of opposite sign (a positive NO_2 anomaly and a negative O_3 anomaly or vice versa) as is expected in a NO_x -saturated atmosphere. The other half of the sites (Reseda, Central LA, La Habra, Upland, Fontana, and Lake Elsinore) show little O_3 anomaly at all or have O_3 and NO_2 anomalies with the same sign suggesting that they may be in NO_x -insensitive or even NO_x-limited photochemical regimes in 2020. Each site in the SoCAB is influenced by accumulation and photochemical processing of the upwind pollutants, local emissions, and average meteorology (Wagner et al., 2012; Baidar et al., 2015). The combination of these factors has led to historically larger O_3, and often lower NO_2, concentrations in the northeast parts of the basin. It is no surprise then that the sites exhibiting NO_x -insensitive or NO_x -limited behavior are downwind or outside the most heavily NO_x polluted areas of the basin (Figure 2.2). The Central LA site is an exception with negative 2020 anomalies in both NO_2 and O_3 despite being close to the maximum in tropospheric NO_2 columns, but also experienced one of the largest NO_2 anomalies, possibly triggering this NO_x -limited response.

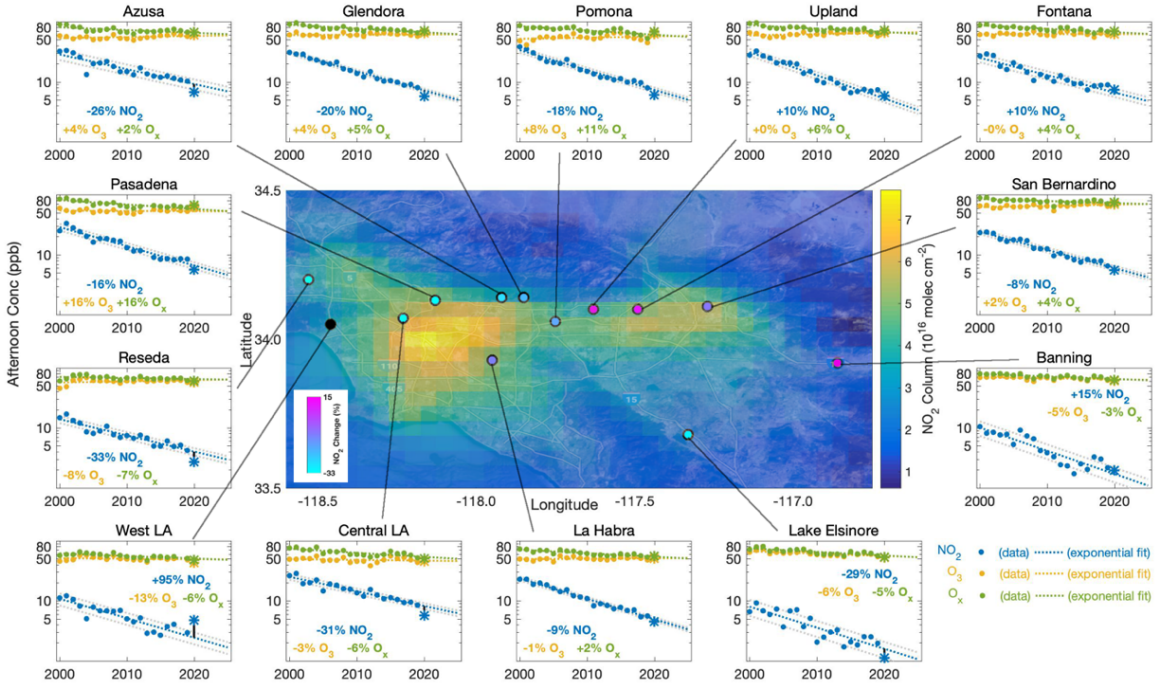

Figure 2.2: Middle panel: Map of the tropospheric NO_2 column as measured by the TROPOMI instrument for the 19 March to 30 June, 2020 period with color indicated by the bar to the right of the map. The locations of each air quality monitoring site are denoted by circles color-coded (excluding the West LA site) by the difference between the 2020 afternoon NO_2 values and the value expected by the 2000 to 2019 trend in afternoon NO_2 in percent. Surrounding Panels: Time series plots of NO_2, O_3, and O_x in ppb for each site for the 19 March to 30 June period from 2000 to 2020. The dotted lines show the exponential fit for each species. The grey dotted lines represent the standard deviation of the residuals between the measured values of NO_2 and the fit. Values for 2020 are represented by asterisks. The difference between the average afternoon values of NO_2, O_3, and O_x in our analysis period in 2020 and the long-term trend is noted within each individual plot in percent.

The measurement site in West LA shows significantly larger afternoon NO_2 values in 2020 compared to the fit (95% or 2.5 ppb increase), but the decreases in 1-hr DM NO_x from the 2015-2019 to the 2020 COVID period shown in Figure A.10 suggests that there may be a significant shift in time-of-day emission patterns near this site. The variations in NO_2 in the basin are independent of the analysis period. For example, when using the period after the anomalous rain in 2020 (19 April to 30 June), the range of deviations in afternoon NO_2

concentrations is between -34% and 176% (-1.9 and 3.7 ppb) with the West LA site responsible for the upper value of this range (Table A.1).

At this time, we have fewer constraints on how VOC emissions have changed in 2020. Formaldehyde columns measured in Pasadena, however, provide some clues. CH_2O is formed within the atmosphere from the photo-oxidative degradation of hydrocarbons. Major CH_2O loss pathways are photolysis and reaction with OH radical. Assuming daytime [OH] = 4×10^6 molec cm^{-3} (Griffith et al., 2016), and $j_{CH2O} = 5.3 \times 10^{-5}$ s^{-1} (noontime values scaled by 0.7), we estimate a daytime photochemical lifetime of 3.2 hours for CH_2O, with photolysis accounting for about 60% of the loss. Thus, we expect the abundance of CH_2O to be quite sensitive to the oxidation rate of VOC. Afternoon column CH_2O measurements in Pasadena exhibited a 10% decrease in the COVID-19 period in 2020 ($1.25\pm0.53\times10^{16}$ molec cm^{-2}) from the COVID-19 period between 2015 and 2019 ($1.37\pm0.35\times10^{16}$ molec cm^{-2}) (Figure A.12). The changes in CH_2O column abundance are consistent with what would be expected from the 30% decline in vehicular emissions assuming such emissions account for 14 of the total. Since Pasadena exhibited NO_x -saturated behavior, the increase in O_3 in 2020 from the reduction of NO_2 may have been muted by the observed 10% decrease, so far as CH_2O is effective as a proxy of VOC emissions. Changes in VOCs around the basin may have similar corresponding effects on the local chemistry shown in Figure 2.2 and Table A.1.

2.3.3 The Correlation of Air Quality and Temperature

There is a strong correlation between air pollution levels and temperature in Los Angeles (Figure 2.3). Such correlations are well documented and have been used to analyze changes in emissions and photochemical regimes elsewhere (Geddes et al., 2009; Pusede et al., 2014, 2015; Baidar et al., 2015). In the SoCAB, hot, sunny days result in faster rates of photochemistry from the combination of increases in sunlight, increased biogenic and evaporative emissions, increases in many temperature-dependent rate coefficients, and metrological differences due to a shallower mixed layer that traps pollutants closer to the surface. While NO_x emissions have been shown to be largely independent of temperature,

VOC emissions are known to increase with temperature due to enhanced evaporation and increased biogenic emissions (Pusede et al., 2015; McDonald et al., 2018; Final 2016 Air Quality Management Plan, 2016). Here, we illustrate the correlation of air quality with temperature using measurements in Pasadena made in 2010 and 2020.

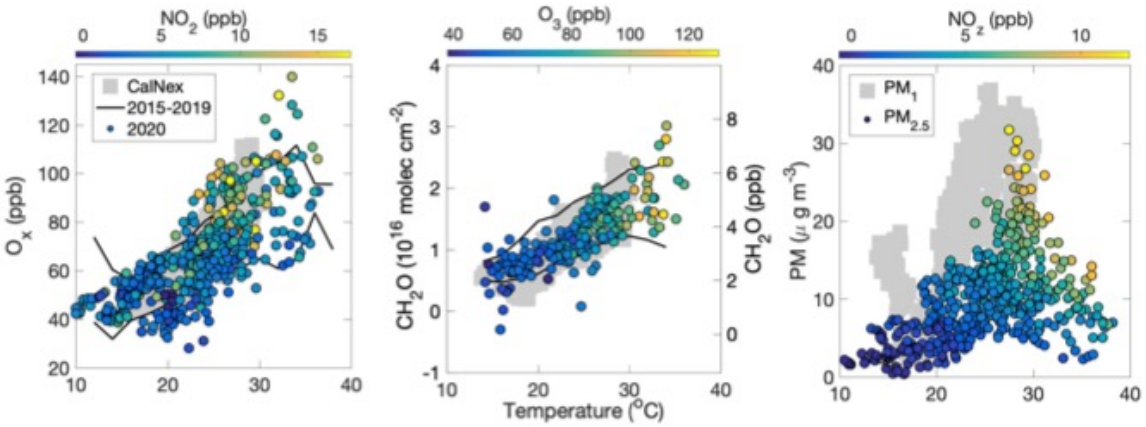

Figure 2.3: Left: Hourly afternoon COVID period O_x concentrations are plotted against temperature and color coded by NO_2, all in ppb. The grey boxes are CalNex O_x concentrations in ppb. Middle: Hourly afternoon COVID period CH_2O column abundances, in molecules per square centimeter, are plotted against temperature and color coded by O_3. The grey boxes are CalNex CH_2O concentrations in ppb and follow the right y-axis. Right: Afternoon COVID period $PM_{2.5}$ concentrations are plotted against temperature and are color coded by NO_z. The grey boxes are PM_1 concentrations from CalNex measurements. All data shown here is from Pasadena. In the left and middle panels, the upper and lower black lines are the 10% and 90% quantile values for the COVID period from 2015 to 2019 values, respectively.

Figure 2.3 shows afternoon values of O_x, CH_2O, and $PM_{2.5}$ plotted against temperature during CalNex in 2010 (May through July 2010) and for data from the 19 March to 30 June period from the South Coast AQMD station in Pasadena, CITAQS, or the Caltech TCCON instrument. Afternoon temperatures in Pasadena were slightly cooler in 2020 (by 0.22 C on average) than in the 2015 -2019 COVID periods (Figure A.13). There is little change in the values of O_x or its relationship to temperature. Likewise, the relationship of O_3 to temperature is consistent over the same period (Figure A.14). $PM_{2.5}$ has, however, decreased. Although the overall concentration of O_x is decreasing, it is doing so slowly and following the same relationship with respect to temperature as observed over the last 5 to

10 years so that it is not readily apparent in Figure 2.3. CH_2O column amounts have been consistent over the past five years with a clear dependence on temperature that remains in 2020 despite lower observed values. While the mechanisms leading to the formation of $PM_{2.5}$ are more complicated than the reactions that lead to the formation of NO_2, O_3, and CH_2O, Figure 2.3 shows that $PM_{2.5}$ is correlated to temperature, particularly for temperatures comparable with the CalNex measurements (10-30 C), and that variations in $PM_{2.5}$ across the temperature range are correlated with variations in NO_x oxidation products (NO_z). By definition PM_1 concentrations are at most equal to $PM_{2.5}$ values so that Figure 2.3 shows $PM_{2.5}$ concentrations have decreased since CalNex measurements of PM_1 in 2010.

As NO_x decreases in a NO_x -saturated photochemical regime, OH concentrations increase and therefore the rate at which VOCs are oxidized also will increase. Thus, even if VOC emissions decrease the net photochemistry will not necessarily change. CH_2O concentrations can provide a measure of this net VOC photochemistry. In Pasadena, the increase of O_3 and decrease in CH_2O compared to the last 5 years suggests, therefore, that NO_x reductions have not yet reached the point where the net photochemistry has slowed significantly outside of temperature driven variations. The continued temperature dependence over the past decade in Pasadena suggests that the O_x in similarly NO_x -saturated areas of the basin will continue to be driven by meteorology along with changes in emissions and that the reductions in NO_x concentrations from COVID-19 countermeasures have not outpaced the effects of meteorology on the production of O_x . It should be noted that the CH_2O measurements from CalNex shown in Figure 2.3 were in situ and therefore are not directly comparable to the column CH_2O observations but still demonstrate the same temperature dependence.

In summary, while absolute concentrations of O_x have slightly decreased over the last decade, the temperature dependences of O_x , CH_2O, and $PM_{2.5}$ have remained similar over the past 5 years and when compared to temperatures seen during CalNex measurements despite substantial reductions in NO_x emissions (Final 2016 Air Quality Management Plan,

2016). The consistency of pollutant concentrations and patterns with respect to temperature in 2020 despite significant reductions in vehicular emissions during COVID-19 countermeasures emphasizes the influence of weather on air quality (especially during years with consistently record-breaking temperatures) and the need for other, concurrent approaches to reducing O_x in combination with vehicular emissions reductions.

2.3.4 2020 Air Quality as a glimpse of the future

In the same way that changes in air quality between the weekend and weekdays have provided insight into the role of truck emissions (Baidar et al., 2015), the broader traffic reductions associated with COVID-19 provide insight into expected air quality changes over the next five years, assuming the continuation of the long-term trends of reductions in vehicular emissions. On most weekends in the SoCAB, the reduction in NO_x emissions from heavy duty diesel trucks reduces morning O_3 titration and increases O_3 production efficiency, leading to an overall increase in O_3 concentrations (the so-called NO_x disbenefit). While the magnitude of the weekend reduction in 1-hr DM NO_x varies from site to site, most of the sites across the basin showed a larger percentage reduction (5- 30%) of 1-hr DM NO_x from the weekends to the weekdays between the 2015 to 2019 and 2020 COVID-19 period which would theoretically enhance the O_3 weekend effect (Figure A.15). However, the weekend to weekday differences in 8-hr DM O_3 have decreased across the basin (Figure A.16). In fact, some of the sites (mostly located in downwind areas of the basin such as Pasadena, Mira Loma, and Rubidoux) show lower 8-hr DM O_3 on weekends compared to weekdays during the 2020 COVID period, suggesting that in some areas of the basin we may finally be approaching NO_x emission levels that slow photochemistry. On the other hand, the consistency of O_x values despite the substantial NO_x reduction suggests that the western portion of the basin is still NO_x -saturated (Pollack et al., 2012; Wolff et al., 2013; Baidar et al., 2015; Fujita et al., 2016).

The lack of improvement in O_x levels in 2020 is consistent with the pattern observed over the past decade in the basin (Figure 2.3). Only under exceptionally low vehicular emissions (e.g. weekends during April and May 2020), are there now glimmers of hope that oxidant

levels will begin to decline. Thus, these data suggest that a broader focus on reducing VOC emissions (in combination with the current focus on NO_x reductions) will be needed to attain air quality standards basin-wide. As VOC emissions from light duty vehicles are now thought to be a minority of the total VOC emissions (McDonald et al., 2018), reductions in VOC emissions will need to come primarily from area and non-mobile sources such as solvent use, paints, cleaners, gardening equipment, and the oil/gas sector. To the extent that biogenic emissions are important, replacing high-VOC emitting trees species would also be helpful.

Acknowledgments

The views expressed in this document are solely those of the authors and do not necessarily reflect those of the South Coast AQMD. Data from the CITAQS is available by request and will be available online to the public in the near future. This facility was funded by Caltech's Linde Center for Global Environmental Science and the Resnick Sustainability Institute. All data from the AQMD sites is available through the California Air Resources Board Air Quality Data Query Tool (https://www.arb.ca.gov/aqmis2/aqdselect.php). Data from the CalNex campaign is available online (https://www.esrl.noaa.gov/csl/projects/calnex/). TROPOMI data used in this research is available through the Sentinel-5P Data Hub (https://s5phub.copernicus.eu/). Traffic data used here is available through the Caltrans PeMS program (http://pems.dot.ca.gov/). Weather data is available online or by contacting the corresponding author (http://tccon-weather.caltech.edu/). We thank NASA via NNX17AE15G for support of retrievals of CH_2O from the Caltech TCCON station. Harrison Parker thanks the Rose Hill Foundation for initial support of his graduate fellowship.

References

Baidar, S., Hardesty, R. M., Kim, S.-W., Langford, A. O., Oetjen, H., Senff, C. J., Volkamer, R. (2015, November). Weakening of the weekend ozone effect over California's South Coast Air Basin: WEEKEND OZONE EFFECT OVER CALIFORNIA. Geophysical Research Letters, 42 (21), 9457–9464. Retrieved 2018-

10-17, from http://doi.wiley.com/10.1002/2015GL066419 doi: 10.1002/2015GL066419

Bauwens, M., Compernolle, S., Stavrakou, T., M¨uller, J., Gent, J., Eskes, H., Zehner, C. (2020, June). Impact of Coronavirus Outbreak on NO 2 Pollution Assessed Using TROPOMI and OMI Observations. Geophysical Research Letters, 47 (11). Retrieved 2020-06-22, from https://onlinelibrary.wiley .com/doi/abs/10.1029/2020GL087978 doi: 10.1029/2020GL087978

CEPAM: 2016 SIP - Standard Emission Tool. (n.d.). Retrieved 2020-09-23, from https://www.arb.ca.gov/app/emsinv/fcemssumcat/cepam emssumcat query v5.php

Final 2016 Air Quality Management Plan (Tech. Rep.). (2016). South Coast Air Quality Management District. Retrieved from https://www.aqmd.gov/ docs/default-source/clean-air-plans/air-quality-management-plans/ 2016-air-quality-management-plan/final-2016-aqmp/final2016aqmp.pdf ?sfvrsn=15

Fujita, E. M., Campbell, D. E., Stockwell, W. R., Saunders, E., Fitzgerald, R., & Perea, R. (2016, February). Projected ozone trends and changes in the ozone-precursor relationship in the South Coast Air Basin in response to varying reductions of precursor emissions. Journal of the Air & Waste Management Association, 66 (2), 201–214. Retrieved 2018-10-17, from https://www.tandfonline.com/doi/full/10.1080/10962247.2015.1106991 doi: 10.1080/10962247.2015.1106991

Geddes, J. A., Murphy, J. G., & Wang, D. K. (2009, July). Long term changes in nitrogen oxides and volatile organic compounds in Toronto and the challenges facing local ozone control. Atmospheric Environment, 43 (21), 3407–3415. Retrieved 2018-10-17, from http://linkinghub.elsevier.com/retrieve/pii/ S1352231009002507 doi: 10.1016/j.atmosenv.2009.03.053

Goldberg, D. L., Anenberg, S. C., Griffin, D., McLinden, C. A., Lu, Z., & Streets, D. G. (2020, September). Disentangling the Impact of the COVID-19 Lockdowns on Urban NO 2 From Natural Variability. Geophysical Research Letters, 47 (17). Retrieved 2020-11-03, from https://onlinelibrary.wiley.com/doi/ 10.1029/2020GL089269 doi: 10.1029/2020GL089269

Griffith, S. M., Hansen, R. F., Dusanter, S., Michoud, V., Gilman, J. B., Kuster, W. C., Stevens, P. S. (2016, April). Measurements of hydroxyl and hydroperoxy radicals during CalNex-LA: Model comparisons and radical budgets: HO x Radicals During CalNex-LA. Journal of Geophysical Research: Atmospheres, 121 (8), 4211–4232. Retrieved 2018-10-17, from http:// doi.wiley.com/10.1002/2015JD024358 doi: 10.1002/2015JD024358

Jiang, Z., McDonald, B. C., Worden, H., Worden, J. R., Miyazaki, K., Qu, Z., Boersma, K. F. (2018, May). Unexpected slowdown of US pollutant emission reduction in the past decade. Proceedings of the National Academy of Sciences, 115 (20), 5099–5104. Retrieved 2018-10-17, from http://www.pnas.org/lookup/doi/10.1073/pnas.1801191115 doi: 10.1073/pnas.1801191115

Le, T., Wang, Y., Liu, L., Yang, J., Yung, Y. L., Li, G., & Seinfeld, J. H. (2020, June). Unexpected air pollution with marked emission reductions during the COVID-19 outbreak in China. Science, eabb7431. Retrieved 2020-07-14, from https://www.sciencemag.org/lookup/doi/10.1126/science.abb7431 doi: 10.1126/science.abb7431

McDonald, B. C., de Gouw, J. A., Gilman, J. B., Jathar, S. H., Akherati, A., Cappa, C. D., Trainer, M. (2018, February). Volatile chemical products emerging as largest petrochemical source of urban organic emissions si. Science, 359 (6377), 760–764. Retrieved 2018-10-17, from http://www.sciencemag.org/lookup/doi/10.1126/science.aaq0524 doi: 10.1126/science.aaq0524

Naeger, A. R., & Murphy, K. (2020). Impact of COVID-19 Containment Measures on Air Pollution in California. Aerosol and Air Quality Research, 20 (10), 2025–2034. Retrieved 2020-11-03, from https://aaqr.org/articles/aaqr-20 -05-covid-0227 doi: 10.4209/aaqr.2020.05.0227

Parrish, D. D., Xu, J., Croes, B., & Shao, M. (2016, October). Air quality improvement in Los Angeles—perspectives for developing cities. Frontiers of Environmental Science & Engineering, 10 (5). Retrieved 2018-10-17, from http://link.springer.com/10.1007/s11783-016-0859-5 doi: 10.1007/s11783-016-0859-5

Pollack, I. B., Ryerson, T. B., Trainer, M., Neuman, J. A., Roberts, J. M., & Parrish, D. D. (2013, June). Trends in ozone, its precursors, and related secondary oxidation products in Los Angeles, California: A synthesis of measurements from 1960 to 2010: OZONE TRENDS IN LA FROM 1960 TO 2010. Journal of Geophysical Research: Atmospheres, 118 (11), 5893–5911. Retrieved 2018-10-17, from http://doi.wiley.com/10.1002/jgrd.50472 doi: 10.1002/jgrd.50472

Pollack, I. B., Ryerson, T. B., Trainer, M., Parrish, D. D., Andrews, A. E., Atlas, E. L., Xiang, B. (2012, November). Airborne and ground-based observations of a weekend effect in ozone, precursors, and oxidation products in the California South Coast Air Basin: SOCAB WEEKEND OZONE EFFECT. Journal of Geophysical Research: Atmospheres, 117 (D21), n/a–n/a. Retrieved 2019-10-30, from http://doi.wiley.com/10.1029/2011JD016772 doi: 10.1029/2011JD016772

Pusede, S. E., Gentner, D. R., Wooldridge, P. J., Browne, E. C., Rollins, A. W., Min, K.-E., Cohen, R. C. (2014, April). On the temperature dependence of organic reactivity, nitrogen oxides, ozone production, and the impact of emission controls in San Joaquin Valley, California. Atmospheric Chemistry and Physics, 14 (7), 3373–3395. Retrieved 2018-10-17, from https:// www.atmos-chem-phys.net/14/3373/2014/ doi: 10.5194/acp-14-3373-2014

Pusede, S. E., Steiner, A. L., & Cohen, R. C. (2015, May). Temperature and Recent Trends in the Chemistry of Continental Surface Ozone. Chemical Reviews, 115 (10), 3898–3918. Retrieved 2018-10-17, from http://pubs.acs.org/doi/ 10.1021/cr5006815 doi: 10.1021/cr5006815

Schiferl, L. D., Heald, C. L., Nowak, J. B., Holloway, J. S., Neuman, J. A., Bahreini, R., Murphy, J. G. (2014, February). An investigation of ammonia and inorganic particulate matter in California during the CalNex campaign: CALNEX AMMONIA AND INORGANIC FINE PM. Journal of Geophysical Research: Atmospheres, 119 (4), 1883–1902. Retrieved 2020-07-17, from http://doi.wiley.com/10.1002/2013JD020765 doi: 10.1002/2013JD020765

Seinfeld, J. H., & Pandis, S. N. (2006). Atmospheric chemistry and physics: from air pollution to climate change (2nd ed ed.). Hoboken, N.J: J. Wiley. (OCLC: ocm62493628)

Tanzer-Gruener, R., Li, J., Eilenberg, S. R., Robinson, A. L., & Presto, A. A. (2020, June). Impacts of Modifiable Factors on Ambient Air Pollution: A Case Study of COVID-19 Shutdowns. Environmental Science & Technology Letters. Retrieved 2020-06-30, from https://pubs.acs.org/doi/10.1021/ acs.estlett.0c00365 doi: 10.1021/acs.estlett.0c00365

Veefkind, J. P., Aben, I., McMullan, K., F¨orster, H., de Vries, J., Otter, G., Levelt, P. F. (2012, May). TROPOMI on the ESA Sentinel-5 Precursor: A GMES mission for global observations of the atmospheric composition for climate, air quality and ozone layer applications. Remote Sensing of Environment, 120 , 70–83. Retrieved 2018-10-31, from http://www.sciencedirect.com/science/ article/pii/S0034425712000661 doi: 10.1016/j.rse.2011.09.027

Villena, G., Bejan, I., Kurtenbach, R., Wiesen, P., & Kleffmann, J. (2012, January). Interferences of commercial NO₂ instruments in the urban atmosphere and in a smog chamber. Atmospheric Measurement Techniques, 5 (1), 149–159. Retrieved 2018-10-17, from https:// www.atmos-meas-tech.net/5/149/2012/ doi: 10.5194/amt-5-149-2012

Wagner, N. L., Riedel, T. P., Roberts, J. M., Thornton, J. A., Angevine, W. M., Williams, E. J., Brown, S. S. (2012). The sea breeze/land breeze circulation in Los Angeles and its influence on nitryl chloride production in this region. Journal of Geophysical

Research: Atmospheres, 117 (D21). Retrieved 2020-07-14, from https://agupubs .onlinelibrary.wiley.com/doi/abs/10.1029/2012JD017810 (eprint: https://agupubs.onlinelibrary.wiley.com/doi/pdf/10.1029/2012JD017810) doi: 10.1029/2012JD017810

Wolfe, G. M., Kaiser, J., Hanisco, T. F., Keutsch, F. N., Gouw, J. A. d., Gilman, J. B., Warneke, C. (2016, March). Formaldehyde production from isoprene oxidation across NOx regimes. Atmospheric Chemistry and Physics, 16 (4), 2597–2610. Retrieved 2018-11-05, from https://www.atmos-chem-phys.net/ 16/2597/2016/ doi: https://doi.org/10.5194/acp-16-2597-2016

Wolff, G. T., Kahlbaum, D. F., & Heuss, J. M. (2013, March). The vanishing ozone weekday/weekend effect. Journal of the Air & Waste Management Association, 63 (3), 292–299. Retrieved 2018-10-17, from https:// www.tandfonline.com/doi/full/10.1080/10962247.2012.749312 doi: 10.1080/10962247.2012.749312

Wunch, D., Toon, G. C., Blavier, J.-F. L., Washenfelder, R. A., Notholt, J., Connor, B. J., Wennberg, P. O. (2011, May). The Total Carbon Column Observing Network. Philosophical Transactions of the Royal Society A: Mathematical, Physical and Engineering Sciences, 369 (1943), 2087–2112. Retrieved 2018- 10-17, from http://rsta.royalsocietypublishing.org/cgi/doi/10.1098/ rsta.2010.0240 doi: 10.1098/rsta.2010.0240

Zhu, L., Jacob, D. J., Mickley, L. J., Marais, E. A., Cohan, D. S., Yoshida, Y., Chance, K. V. (2014). Anthropogenic emissions of highly reactive volatile organic compounds in eastern Texas inferred from oversampling of satellite (OMI) measurements of HCHO columns. Environmental Research Let ters, 9 (11), 114004. Retrieved 2018-11-05, from http://stacks.iop.org/ 1748-9326/9/i=11/a=114004 doi: 10.1088/1748-9326/9/11/114004

Chapter 3

INFERRING THE VERTICAL DISTRIBUTION OF CO AND CO_2 FROM TCCON TOTAL COLUMN VALUES USING THE TARDISS ALGORITHM

Parker, H. A., Laughner, J. L., Toon, G. C., Wunch, D., Roehl, C. M., Iraci, L. T., Podolske, J. R., McKain, K., Baier, B., and Wennberg, P. O.: Inferring the vertical distribution of CO and CO 2 from TCCON total column values using the TARDISS algorithm, Gases/Remote Sensing/Data Processing and Information Retrieval, https://doi.org/10.5194/amt-2022-322, 2022.

Abstract

We describe an approach for determining limited information about the vertical distribution of carbon monoxide (CO) and carbon dioxide (CO_2) from total column, ground-based TCCON observations. For CO and CO_2, it has been difficult to retrieve information about their vertical distribution from spectral line shapes because of the errors in the spectroscopy and the atmospheric temperature profile that mask the effects of variations in their mixing ratio with altitude. For CO_2 the challenge is especially difficult given that these variations are typically 2% or less. Nevertheless, if sufficient accuracy can be obtained, such information would be highly valuable for evaluation of retrievals from satellites and more generally for improving the estimate of surface sources and sinks of these trace gases.

We present here the Temporal Atmospheric Retrieval Determining Information from Secondary Scaling (TARDISS) retrieval algorithm. TARDISS uses several, simultaneously-obtained total column observations of the same gas from different absorption bands with distinctly different vertical averaging kernels. The different total column retrievals are combined in TARDISS using a Bayesian approach where the weights and temporal covariance applied to the different retrievals include additional constraints on the diurnal variation in the vertical distribution for these gases. We assume that the near-surface part of the column varies rapidly over the course of a day (from surface sources

and sinks, for example) and the upper part of the column has a larger temporal covariance over the course of a day.

Using measurements from the five North American TCCON sites, we find that the retrieved lower partial column (between the surface and ~800 hPa) of the CO and CO_2 dry mole fractions (DMF) have slopes of 0.999 ±0.002 and 1.001±0.003 with respect to lower column DMF from integrated in situ data measured directly from aircraft and in AirCores. The average error for our lower column CO retrieval is 1.51 ppb (~2%) while the average error for our CO_2 retrieval is 5.09 ppm (~1.25%). Compared with classical line-shape-derived vertical profile retrievals, our algorithm reduces the influence of forward model errors such as imprecision in spectroscopy (line shapes and intensities) and in the instrument line shape. In addition, because TARDISS uses the existing retrieved column abundances from TCCON (which themselves are computationally much less intensive than profile retrieval algorithms), it is very fast and processes years of data in minutes. We anticipate that this approach will find broad application for use in carbon cycle science.

3.1 Introduction

Remote sensing retrievals of atmospheric gas abundances are used to diagnose the sources, sinks, and fluxes at the local, regional, and global scales (Connor et al., 2008, p.2; Deeter, 2004; Kerzenmacher et al., 2012; Wunch et al., 2011). Compared with in situ measurements, these retrievals, which are used in carbon cycle science investigations, are less influenced by nearby point sources or sinks and rapidly changing meteorological conditions that would lead to erroneous flux calculations (Keppel-Aleks et al., 2012). Because the column represents the integral of a gas from the surface to the top of the atmosphere, flux estimates from column amounts are less sensitive to errors in the assumed vertical transport than those using surface measurements (Keppel-Aleks et al., 2011, 2012). In contrast, since signals of CO_2 and CO fluxes at the surface are muted in the total column (due to the dilution of signals from the surface being integrated throughout an entire column), they are less useful in diagnosing local emissions than in situ measurements. For

CO_2, the total columns are strongly influenced by synoptic scale transport in the troposphere making it even more difficult to discern the influences of surface fluxes (Keppel-Aleks et al., 2011, 2012). For CO, its several-week lifetime in the free troposphere results in regional transport influences that can dampen the surface signals in the total column values (Deeter, 2004; Zhou et al., 2019). These issues limit the effectiveness of total column measurements in surface flux analysis — particularly for local sources.

Profile retrievals can, in principle, ameliorate these issues and thereby enable more direct information on surface processes. Theoretical analysis shows that two to three vertical degrees of freedom (DoF) can be achieved in CO_2 retrievals from near-IR (NIR) and mid-IR (MIR) spectra from high-resolution Fourier transform spectrometers (Connor et al., 2016; Kuai et al., 2012; Roche et al., 2021; Shan et al., 2021). In practice, however, Connor et al. (2016) and Roche et al. (2021) showed that the precision of retrieved CO_2 profiles using spectral windows in the NIR was much lower than the theoretical estimate due to uncertainty in the temperature profile and in the forward radiative transfer model. Likewise, Shan et al. (2021) retrieve CO_2 profiles using spectral windows in the MIR. They use an a posteriori optimization method to improve the tropospheric CO_2 signal and they report errors near 2%. Although both of these methods retrieve profiles with sufficient degrees of freedom to observe some signals of the variation in the vertical distribution, they report errors sufficiently large enough to encourage the exploration of other methods for use for carbon cycle studies.

Several operational CO profile retrievals exist, but these products still face the issues of column dilution or larger sensitivity to the free troposphere compared to the surface. The Network for the Detection of Atmospheric Composition Change (NDACC) retrieves profiles of CO in the atmosphere (Buchholz et al., 2017) with ~2 degrees of freedom for the signal providing information of a lower (surface-8km) layer sensitive to the boundary layer and an upper (8-20 km) layer with ~1-3% uncertainty in the total column (Zhou et al., 2018, 2019). These ground-based measurements require higher spectral resolution than those typically available in the TCCON interferometers. The higher resolution also requires

longer measurement time, resulting in fewer observations per day. This limits their ability to capture diurnal changes and makes the measurements more susceptible to variations in solar viewing during acquisition of the interferograms. These measurements also require highly accurate knowledge of the spectral line widths, their temperature dependence, the instrument line shape (ILS), and the solar spectrum. These limitations motivate our work to develop a new product with better sensitivity to surface processes and higher temporal resolution from the existing TCCON retrievals.

In our approach, we do not retrieve profile information directly from the spectra. Instead, we utilize the vertical and temporal domains to infer partial column dry mole fraction (DMF) values. We fit partial column scalar values to match TCCON retrieved total column DMF that are 1) quality controlled and 2) individually tied to World Meteorological Organization (WMO) trace gas standard scales which mitigates a number of errors in the forward radiative transfer model, including those arising from errors in the spectroscopy. We use the extant multiple total column measurements from spectral windows with different line intensities and hence different shapes of the column averaging kernel. We extract the vertical information from the diurnally-varying differences in these total column values and additional a priori information about the expected temporal covariance in the different partial columns based on known atmospheric behavior. This method allows us to extract information focused on the lower atmosphere where the trace gas DMF are most sensitive to surface exchange.

The uncertainty of this new method for retrieving partial column values is evaluated using comparisons with in situ vertical profile measurements. Section 3.2 describes the theory and parameters chosen for our retrieval, and the data used for the retrieval, validation, and comparison. Sections 3.3.1 through 3.3.3 present our validation data and a sensitivity study of the retrieval parameters. Section 3.3.4 presents an error and information content analysis. Finally, Sect. 3.3.5 gives examples of the data retrieved using this approach.

3.2 Methods

3.2.1 Total Carbon Column Observing Network

The Total Carbon Column Observing Network (TCCON) is a ground-based network of solar viewing Fourier transform spectrometers equipped with InGaAs and Si detectors that gather spectra for the 3900 to 15500 cm^{-1} spectral region (Wunch et al., 2011). Importantly for our work here on CO, some sites are now equipped with an InSb detector that simultaneously allows spectral measurement down to 2000 cm^{-1} at the expense of simultaneous observations using the Si detector. CO_2 and CO are retrieved simultaneously over several spectral windows (independent spectral bands). These windows are chosen to provide high sensitivity to the gas of interest while limiting interference from other atmospheric absorbers.

Column abundances of atmospheric species are computed from the measured spectra using a nonlinear least-squares fitting algorithm, GFIT, which minimizes the residuals between a measured spectrum and one calculated by uniformly scaling a priori vertical profiles for the fitted atmospheric species, yielding the optimal VMR (volume mixing ratio) scaling factors (VSF) of the fitted gases. The a priori profiles scaled by the VSF are integrated to calculate the total column abundance of a species. The retrieved scaled column abundances are converted to column dry mole fraction (DMF) by multiplying by 0.2095 and dividing by the column of O_2, retrieved from a different spectral window of the same spectrum. These retrievals are then quality-controlled and scaled to minimize both airmass dependence and the difference with simultaneously measured in situ profiles.

For each window and for each spectrum fit by GFIT, an associated column averaging kernel is computed that describes the sensitivity of the total column to changes in species abundance at each altitude (shown in Fig. 3.1). A perfect column averaging kernel would have values of one for all altitudes. More commonly, the kernels will vary slowly with altitude with a pressure weighted average value close to one. Values higher (lower) than 1 mean that the retrieval is more (less) sensitive to trace gas changes at that altitude. These

sensitivities vary with solar zenith angle (SZA) as the spectral absorption deepens at higher SZA. The vertical sensitivity of each window is a result of its spectral properties. Optically thin spectral regions (windows) tend to be more sensitive to the upper troposphere and the stratosphere while optically thick windows tend to be more sensitive to the lower troposphere. Since information about the stratosphere comes only from near the line center as a result of diminished collisional broadening, if the absorption at the line center is saturated (nearly zero transmission), the spectrum will contain little information about the stratosphere and hence the kernel will be low there. The differences in column averaging kernel shapes are the main source of information used in the TARDISS algorithm. The outputs of the VSF values, a priori profiles, total column DMF values, and vertical averaging kernels from standard TCCON processing are used as input for the TARDISS algorithm.

We will refer to the spectral retrievals as being the TCCON retrievals and the temporal partial column retrievals as the TARDISS fit. We also use the terms retrieval and fit interchangeably to refer to the TCCON or TARDISS methodology.

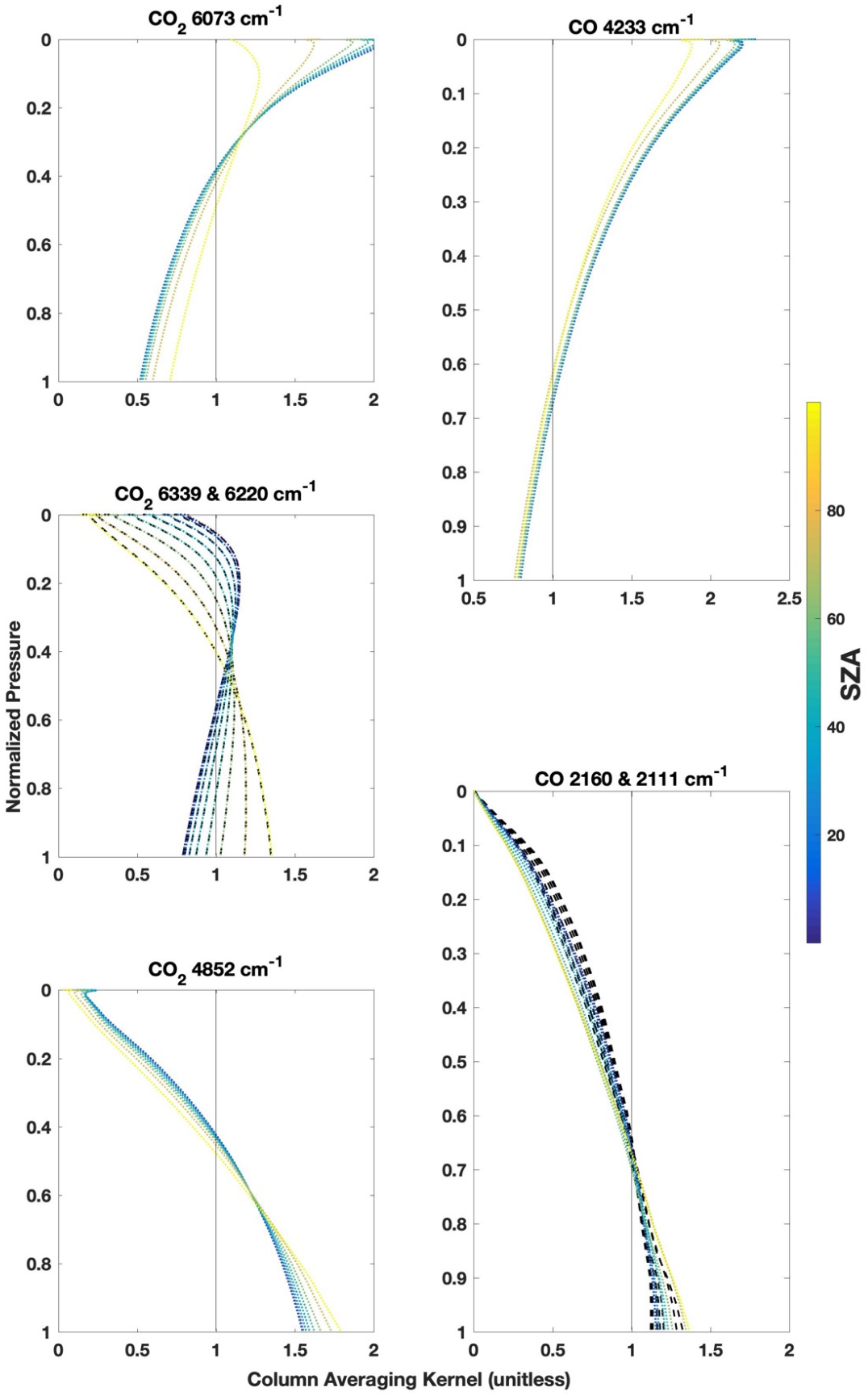
CO2 6073 cm-1
CO 4233 cm-1
CO2 6339 & 6220 cm-1
CO2 4852 cm-1
CO 2160 & 2111 cm-1
Normalized Pressure
Column Averaging Kernel (unitless)
SZA
20
40
60
80

Figure 3.1: Vertical sensitivities of the total column retrievals from GFIT used in our algorithm for both CO_2 (left column) and CO (right column) plotted against pressure normalized to the surface and color coded by the solar zenith angle (SZA). A column averaging kernel greater than 1 means that the total column is more sensitive to molecules at this pressure level than the average sensitivity. For example, if we move some of the CO_2 molecules from 200 hPa to the surface in our a priori profile, the retrieved total column and scale factor (VSF) will decrease for the 6073 cm^{-1} window and increase for the 4852 cm^{-1} window while the true and a priori total columns remain unchanged. The 6220 and 6339 cm^{-1} CO_2 and 2160 and 2111 cm^{-1} CO windows have near-identical kernels due to the CO_2 bands being almost identical in their line strengths, separations, widths, and temperature dependences. The 6339 cm^{-1} CO_2 is represented by black dashed lines behind the dotted lines representing the 6220 cm^{-1} sensitivities and the 2111 cm^{-1} CO is represented by black dashed lines behind the dotted lines representing the 2160 cm^{-1} sensitivities.

3.2.2 The TARDISS Algorithm

Traditional profile retrievals fit spectra by adjusting the abundance of the trace gases at multiple vertical levels to determine the vertical distribution of a specific atmospheric species (Pougatchev et al., 1995; Roche et al., 2021). Here, we describe the Temporal Atmospheric Retrieval Determining Information from Secondary Scaling (TARDISS) algorithm that optimizes the scaling of the profile of our target gas separated into two layers, one near the surface and the other at and above the typical well-mixed surface boundary layer. This is illustrated by the flowchart in Fig. 3.2. The algorithm minimizes the cost function (Equation 3.1) by finding the maximum a posteriori solution for a state vector containing upper and lower column scale factors for all TCCON observations in a given day. That is, if a day has n_s observations, the state vector will have n_s lower column scale factors and n_s upper column scale factors, for $2n_s$ elements total. These are constrained by TCCON column average mole fractions and an assumed temporal covariance. The Jacobian matrix for TARDISS combines the TCCON averaging kernels and the TCCON assumed vertical CO or CO_2 profiles in an operator which maps the upper and lower scale factors back to column average mole fractions. We define our cost function as:

$$\chi^2 = \left(\boldsymbol{y} - \boldsymbol{K}(\hat{\boldsymbol{x}}_\gamma - \boldsymbol{x}_{a,\gamma})\right)^T \boldsymbol{S}_\epsilon^{-1}\left(\boldsymbol{y} - \boldsymbol{K}(\hat{\boldsymbol{x}}_\gamma - \boldsymbol{x}_{a,\gamma})\right) + \left(\hat{\boldsymbol{x}}_\gamma - \boldsymbol{x}_{a,\gamma}\right)\boldsymbol{S}_a^{-1}\left(\hat{\boldsymbol{x}}_\gamma - \boldsymbol{x}_{a,\gamma}\right), \quad (3.1)$$

where **y** is the measurement vector, **K** is the Jacobian matrix, $\hat{\boldsymbol{x}}_\gamma$ is the retrieved state vector, $\boldsymbol{x}_{a,\gamma}$ is the a priori state vector, $\boldsymbol{S}_\epsilon$ is the model covariance matrix, and $\boldsymbol{S}_a$ is the prior covariance matrix. In the following sections, we will derive the necessary equations for the construction of the components of the cost function in detail. Table B.1 lists all the variable names in this work and their descriptions.

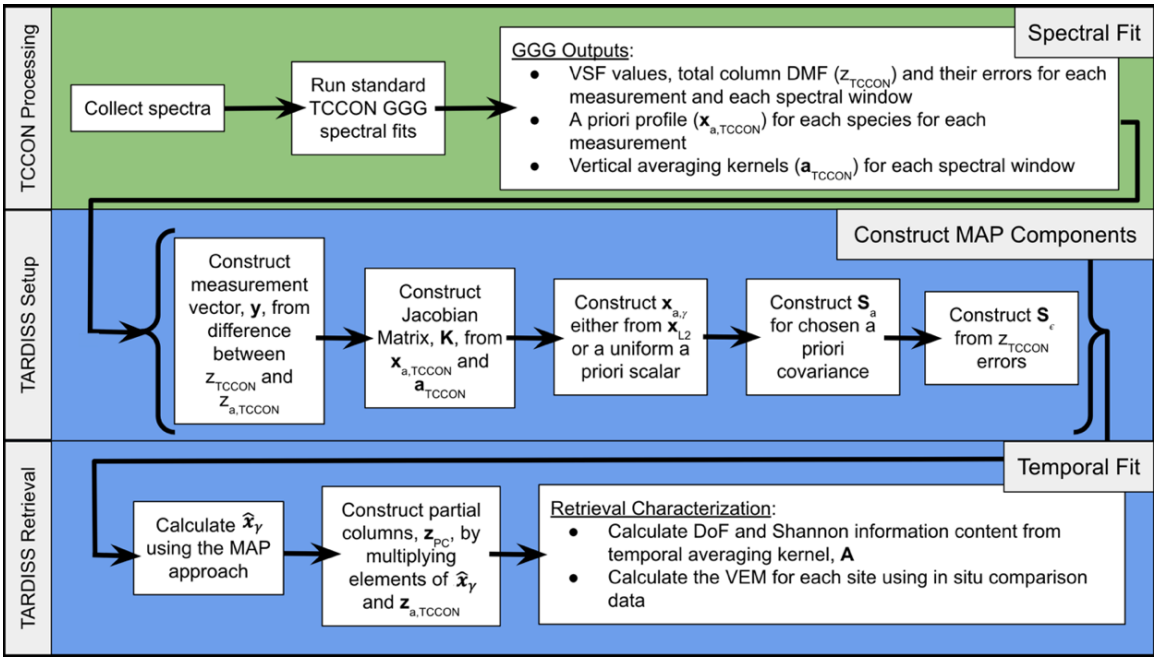

Figure 3.2: Flowchart illustrating the steps performed by of the TARDISS retrieval. The input to the TARDISS retrieval is the output of the spectral fitting done by the GGG2020 software suite represented by the green row. The setup of the components of the TARDISS algorithm from the output of the TCCON spectral fits is shown in Equations 3.11 through 3.14 and in the middle row. The TARDISS retrieval is performed using Equation 3.16, the output partial column DMF values are calculated using Equation 3.17, and the information content is calculated by Equation 3.18 and 3.19 as shown in the bottom row.

3.2.2.1 Derivation of the TARDISS Jacobian Matrix Components

We use the notation and concepts of Rodgers and Connor (2003) with vectors represented with bolded lower-case letters and matrices represented with bolded upper-case letters. We start in the vertical domain where Equations 3.3 through 3.9 are used for each spectral window, each TCCON measurement, and each species retrieved (CO and CO_2 in this work) in the TCCON fit. These equations are used to calculate the weights in the Jacobian matrix and values in the measurement vector for the temporal calculations in Equation 3.10 and beyond (represented by the middle and bottom row of Fig. 3.2). We will therefore keep Equations 3.3 through 3.9 agnostic of species and window for this description.

To derive the values used in the Jacobian matrix, K, we start by relating the atmospheric profile of CO or CO_2 to the column average mole fractions observed by TCCON. For TARDISS, we assume that the a posteriori atmospheric profile can be described as the profile output by the TCCON retrieval with the bottom q levels scaled separately from the top nl – q levels, where q is a chosen level index and nl is the number of vertical levels in the profile:

$$\mathbf{x}_{\text{part}} = \begin{bmatrix} \gamma_L \cdot x_{a,TCCON,1} \\ \vdots \\ \gamma_L \cdot x_{a,TCCON,q} \\ \gamma_U \cdot x_{a,TCCON,q+1} \\ \vdots \\ \gamma_U \cdot x_{a,TCCON,n_l} \end{bmatrix}. \tag{3.2}$$

Here, $x_{a,TCCON}$ is the TCCON a priori profile scaled by the median TCCON retrieved VSF across all the TCCON spectral windows for this gas, and the γ_L and γ_U values are the lower and upper column scale factors, respectively, which our algorithm retrieves. We relate this to the TCCON total column value using the standard equation from Rodgers and Connor (2003):

$$z_{TCCON} = z_{a,TCCON} + \boldsymbol{a}_{TCCON}^{\boldsymbol{\xi T}} (\boldsymbol{x}_{part} - \boldsymbol{x}_{a,TCCON}), \quad (3.3)$$

where z_{TCCON} is the total column DMF output of a chosen species in a particular window from the TCCON fit, $z_{a,TCCON}$ is the original vertical column DMF calculated from the a priori profile scaled by the median VSF of the windows used, and $\boldsymbol{a}_{TCCON}^{\boldsymbol{\xi}}$ is the vector of column averaging kernel values output from the TCCON processing weighted by the pressure thickness of each atmospheric layer. All components in Equation 3.3 are dry mole fractions except for the averaging kernel which is unitless. Equation 3.3 tells us how the retrieved DMF would change if the profile constructed from the two partial columns differed from $x_{a,TCCON}$.

The next step is to rearrange this equation so that our observed quantity is on the left-hand side, and the right-hand side is a linear combination of the two scaling factors. Subtracting $Z_{a,TCCON}$ from both sides and focusing on the rightmost term of Equation 3.3, the averaging kernel is multiplied by the difference of the a priori and scaled DMF profiles summed for each of the nl levels of the atmosphere.

$$z_{TCCON} - z_{a,TCCON} = \mathbf{a}_{TCCON}^{\xi T} \left(\mathbf{x}_{part} - \mathbf{x}_{a,TCCON}\right) = \sum_{i=1}^{nl} a_{TCCON,i} (x_{part,i} - x_{a,TCCON,i}). \quad (3.4)$$

Here, we assign $\boldsymbol{x}_{part}$ to be the TCCON a priori profile scaled by two independent values, one for the lower partial column and one for the upper partial column. To designate the partial columns, our method splits the total column at a specified altitude level index, q, and scales the a priori profile below and above the level q independently by the scalar values γ_L and γ_U such that:

$$z_{TCCON} - z_{a,TCCON} = \sum_{i=1}^{q} a_{TCCON,i} (\gamma_L x_{a,TCCON,i} - x_{a,TCCON,i}) + \sum_{i=q+1}^{nl} a_{TCCON,i} (\gamma_U x_{a,TCCON,i} - x_{a,TCCON,i}) \ . \quad (3.5)$$

Since Equation 3.5 is linear, we then group terms reducing the right side of Equation 3.5 to:

$$z_{TCCON} - z_{a,TCCON} = (\gamma_L - 1) \sum_{i=1}^{q} a_{TCCON,i}\, x_{a,TCCON,i} + (\gamma_U - 1) \sum_{i=q+1}^{n_l} a_{TCCON,i}\, x_{a,TCCON,i}\,. \quad (3.6)$$

Defining two new variables, k_L and k_U, we can write this as:

$$z_{TCCON} - z_{a,TCCON} = (\gamma_L - 1)\, k_L + (\gamma_U - 1)\, k_U, \quad (3.7)$$

where

$$k_L = \sum_{i=1}^{q} a_{TCCON,i}\, x_{a,TCCON,i} \quad (3.8)$$

and

$$k_U = \sum_{i=q+1}^{n} a_{TCCON,i}\, x_{a,TCCON,i} \quad (3.9)$$

and k_L and k_U are both scalar values.

Equation 3.7 is applicable to all spectral windows for each spectrum measured. For example, for our CO_2 retrieval, we use four separate spectral windows per measured spectrum and often have a few hundred spectra measured per day. In the case of the CO_2 retrieval, the left-hand side of Equation 3.7 and the k_L and k_U values will be calculated for each of the four spectral windows used for each spectrum fit by TCCON. These values are aggregated into the vectors and matrices described by Equations 3.10 – 3.14 in order to fit the spectra measured over an entire day at one time.

3.2.2.2 Deriving the Maximum A Posteriori Equation and Solution

While Equation 3.7 can be set up and solved for each spectrum using the total column value from each spectral window used in the TCCON fit, the TARDISS retrieval uses an entire day's worth of TCCON retrievals in order to increase the signal-to-noise and to utilize the information from the temporal variation in the kernels. Fitting over an entire day of TCCON retrievals reduces the retrieved partial column error values compared to fitting individual measurements using Equation 3.7. Section B.1 shows the influence of including multiple observations on the retrieved partial column errors. Let n_w denote the number of

windows and n_s the number of spectra over a day and w_i and s_i denote the ith window and spectrum. We combine the above equations into a matrix form:

$$\boldsymbol{y} = \boldsymbol{K}(\boldsymbol{x}_\gamma - \boldsymbol{x}_{\mathrm{a},\gamma}) + \boldsymbol{\epsilon}, \tag{3.10}$$

where $\boldsymbol{y}$ is the measurement vector composed of values from the left side of Equation 3.7,

$$\boldsymbol{y} = \begin{bmatrix} z_{TCCON,1,1} - z_{a,TCCON,1} \\ \vdots \\ z_{TCCON,w_i,s_i} - z_{a,TCCON,s_i} \\ \vdots \\ z_{TCCON,n_w,n_s} - z_{a,TCCON,n_s} \end{bmatrix}, \tag{3.11}$$

where **K** is the Jacobian matrix of the k_L and k_U values over a day,

$$\boldsymbol{K} = \begin{bmatrix} k_{L,1,1} & & 0 & k_{U,1,1} & & 0 \\ & \ddots & & & \ddots & \\ 0 & & k_{L,1,n_s} & 0 & & k_{U,1,n_s} \\ \vdots & \vdots & \vdots & \vdots & \vdots & \vdots \\ k_{L,n_w,1} & & 0 & k_{U,n_w,1} & & 0 \\ & \ddots & & & \ddots & \\ 0 & & k_{L,n_w,n_s} & 0 & & k_{U,n_w,n_s} \end{bmatrix}, \tag{3.12}$$

where $\boldsymbol{x}_\gamma$ is our state vector of partial column scalars which are the same for all windows in each measured spectrum,

$$\boldsymbol{x}_{\boldsymbol{\gamma}} = \begin{bmatrix} (\gamma_L - 1)_1 \\ \vdots \\ (\gamma_L - 1)_{n_s} \\ (\gamma_U - 1)_1 \\ \vdots \\ (\gamma_U - 1)_{n_s} \end{bmatrix}, \tag{3.13}$$

and $\boldsymbol{x}_{\mathrm{a},\gamma}$ is our vector of a priori partial column scalars,

$$\boldsymbol{x}_{\mathrm{a},\gamma} = \begin{bmatrix} (\gamma_{a,L} - 1)_1 \\ \vdots \\ (\gamma_{a,L} - 1)_{n_s} \\ (\gamma_{a,U} - 1)_1 \\ \vdots \\ (\gamma_{a,U} - 1)_{n_s} \end{bmatrix} . \tag{3.14}$$

With n_s measurements made in a day, n_w spectral windows, and two partial columns, the $\boldsymbol{y}$ vector is of the size 1 by $n_w n_s$, the $\boldsymbol{K}$ matrix is of the size $n_w n_s$ by $2n_s$ and the $\boldsymbol{x}_\gamma$ and $\boldsymbol{x}_{\mathrm{a},\gamma}$ vectors are of the size $2n_s$ by 1. So, for each spectrum, there is one γ_L value and one γ_U value, representing the partial column scale factors aggregated over the windows.

Since Equation 3.10 is linear, we can apply a basic linear least-squares method to solve for the partial column scalars:

$$\boldsymbol{x}_{L2} = \boldsymbol{x}_{\mathrm{a},\gamma} + (\boldsymbol{K}^T\boldsymbol{K})^{-1}\boldsymbol{K}^T\boldsymbol{y}, \tag{3.15}$$

While the linear least-squares method provides a useable solution to our retrieval, it also has partial column error values on the order of 10 ppm, due to the strong anti-correlation of the lower and upper partial columns, which render the solutions unsuitable for carbon cycle science. Including constraints through a Bayesian approach reduces the retrieved partial column error values as shown in Fig. B.1. In addition, the least-squares method does not allow us to utilize additional a priori information in the covariance of the partial columns.

We use the maximum a posteriori (MAP) approach (Rodgers, 2008) to calculate the most probable state vector from the given models and a priori information. In line with the assumptions of the MAP approach, we assume our problem is linear and follows a gaussian distribution. The MAP solution can take a few equivalent forms. In this work we use:

$$\hat{\boldsymbol{x}}_\gamma = \boldsymbol{x}_{a,\gamma} + \boldsymbol{S}_a\boldsymbol{K}^T(\boldsymbol{K}\boldsymbol{S}_a\boldsymbol{K}^T + \boldsymbol{S}_\epsilon)^{-1}(\boldsymbol{y} - \boldsymbol{K}\boldsymbol{x}_{a,\gamma}), \tag{3.16}$$

where $\boldsymbol{x}_{a,\gamma}$ is the a priori partial column scalar values, $\boldsymbol{S}_a$ is the a priori covariance matrix, $\boldsymbol{K}$ is the Jacobian matrix, $\boldsymbol{S}_\epsilon$ is the model covariance matrix, $\boldsymbol{y}$ is the measurement vector, and $\hat{\boldsymbol{x}}_\gamma$ is the output solution vector. The input components ($\boldsymbol{x}_{a,y}$, $\boldsymbol{S}_a$, and $\boldsymbol{S}_\epsilon$) are described in Sect. 3.2.3.2.

Once we have calculated the most likely solution for the partial column scalars as a vector in temporal space, $\hat{\boldsymbol{x}}_\gamma$, we reconstruct the partial column DMF values for the day for the lower and upper partial columns as:

$$\boldsymbol{z}_{PC} = \begin{bmatrix} z_{PC,L,1} \\ \vdots \\ z_{PC,L,n_s} \\ z_{PC,U,1} \\ \vdots \\ z_{PC,U,n_s} \end{bmatrix} = \begin{bmatrix} (\hat{x}_{\gamma L,1} + 1) \cdot z_{a,L,TCCON,1} \\ \vdots \\ (\hat{x}_{\gamma L,n_s} + 1) \cdot z_{a,L,TCCON,n_s} \\ (\hat{x}_{\gamma U,1} + 1) \cdot z_{a,U,TCCON,1} \\ \vdots \\ (\hat{x}_{\gamma U,n_s} + 1) \cdot z_{a,U,TCCON,n_s} \end{bmatrix} \tag{3.17}$$

where $z_{a,L,TCCON}$ and $z_{a,U,TCCON}$ are the values of the a priori partial column DMFs calculated by integrating the median TCCON a posteriori profiles for the measurements in a day using the same method as the standard TCCON full column retrievals (Wunch et al., 2011).

3.2.2.3 Calculating Informational Content

The MAP retrieval allows us to calculate the information content of the retrieval. In particular, we compare the degrees of freedom for our retrieval calculated by taking the trace of the averaging kernel of the fit, calculated as the following:

$$DoF = tr(\boldsymbol{A}) = tr((\boldsymbol{K}^T \boldsymbol{S}_\epsilon^{-1} \boldsymbol{K} + \boldsymbol{S}_a^{-1})^{-1} \boldsymbol{K}^T \boldsymbol{S}_\epsilon^{-1} \boldsymbol{K}), \tag{3.18}$$

as well as the Shannon information content derived from the natural log of the determinant of the difference between the averaging kernel and an identity matrix:

$$H = -\frac{1}{2} \ln (|\boldsymbol{I} - \boldsymbol{A}|). \tag{3.19}$$

Generally, profile retrieval averaging kernels represent the sensitivity of a specific level of a profile to the rest of the levels in the profile. The averaging kernel for the TARDISS inversion is a temporal averaging kernel relating how each partial column calculation relates to every other measurement during a day. The DoF value for a day of the retrieval represents how many individual pieces of partial column information we can infer over the day of measurements. We either report the number of degrees of freedom from the fit over a day or normalize the degrees of freedom by the number of measurements in each day for a more comparative understanding of the TARDISS degrees of freedom with respect to a traditional profile retrieval as well as between days with a large variation in the number of measurements.

3.2.2.4 In Situ Comparison Calculations

To evaluate the accuracy of our partial column retrieval, we use the smoothing calculation shown in Equation 3 of Wunch et al. (2010), altered to use the terminology of this work, to determine the value of the partial columns of the TCCON total columns used as input:

$$\hat{z}_s = z_{a,TCCON} + \boldsymbol{a}_{TCCON}^{\xi T}\left(\boldsymbol{x}_{true} - \boldsymbol{x}_{a,TCCON}\right), \tag{3.20}$$

where $\hat{z}_s$ is the smoothed column averaged DMF, $z_{a,TCCON}$ is the column averaged DMF of the scaled a priori profile, $\boldsymbol{a}_{TCCON}^{\xi}$ is the vertical averaging kernel for the specific spectral window dotted with an integration operator, $\boldsymbol{x}_{true}$ is the measured, in situ profile in DMF, and $\boldsymbol{x}_{a,TCCON}$ is the scaled a priori profile. We use this equation to create the smoothed partial column TCCON DMF values by integrating to the same split point, q, as in Equation 3.5. These values serve as a sort of null hypothesis to compare to the TARDISS retrieval to determine if the fits are effective in inferring partial column information.

In order to compare the partial column retrievals to in situ profiles for validation purposes, we calculate the vertical sensitivities of the TARDISS fit (shown in Fig. 3.8) using the gain

matrix, G, from the TARDISS inversion and the averaging kernel profiles from the TCCON measurement windows as:

$$\boldsymbol{G} = (\boldsymbol{K}^T \boldsymbol{S}_\epsilon^{-1} \boldsymbol{K} + \boldsymbol{S}_a^{-1})^{-1} \boldsymbol{K}^T \boldsymbol{S}_\epsilon^{-1} \quad . \tag{3.21}$$

$$\boldsymbol{A}_{vert} = \boldsymbol{G}\, \boldsymbol{\Xi}_{TCCON}, \tag{3.22}$$

where

$$\boldsymbol{\Xi}_{TCCON} = \begin{bmatrix} \boldsymbol{a}_{TCCON,1,1} \\ \vdots \\ \boldsymbol{a}_{TCCON,1,n_s} \\ \boldsymbol{a}_{TCCON,n_w,1} \\ \vdots \\ \boldsymbol{a}_{TCCON,n_w,n_s} \end{bmatrix} \quad , \tag{3.23}$$

and $\boldsymbol{a}_{TCCON}$ is the same vector of column averaging kernels from Equation 3.3 without the integration operator for each window used and $\boldsymbol{A}_{vert}$ is the vertical sensitivity of the partial column related to the profile. **G** has dimensions of $2n_s$ by $n_w n_s$, $\boldsymbol{\Xi}_{TCCON}$ has dimensions of $n_w n_s$ by 51, and $\boldsymbol{A}_{vert}$ has dimensions of $2n_s$ by 51. The gain matrix relates each measurement in a day to the upper and lower partial column calculation which is useful to calculate the temporal DoF but is not directly comparable to in situ vertical profiles. The $\boldsymbol{A}_{vert}$ term converts the temporal sensitivities of the gain matrix to vertical sensitivities using the TCCON vertical averaging kernel allowing us to compare with the in situ validation profiles. We apply the average vertical sensitivities for the measurements used in comparison with in situ profile measurements.

Since $\boldsymbol{a}_{TCCON}$ represents the change in TCCON total column DMF (also called X_{gas}) per change in true DMF at each level ($\frac{\boldsymbol{\delta X_{gas,TCCON}}}{\boldsymbol{\delta x_{true}}}$) and the gain matrix represents the change in partial column scalar per change in TCCON total column DMF ($\frac{\boldsymbol{\delta \gamma}}{\boldsymbol{\delta X_{gas,TCCON}}}$), $\boldsymbol{A_{vert}}$ has units of change in partial column scalar per change in level DMF value ($\frac{\boldsymbol{\delta \gamma}}{\boldsymbol{\delta x_{true}}}$) and relies on the difference between a 'true' in situ profile and the a priori profile used in the inversion.

For our TARDISS comparisons, we use an adjusted version of Equation 3.20 to determine the value the inversion would return if it were using the true profile instead of the scaled TCCON priors:

$$\hat{z}_s = z_{a,TCCON} + \boldsymbol{A}_{vert}\left(\boldsymbol{x}_{true} - \boldsymbol{x}_{a,TCCON}\right), \tag{3.24}$$

where $\boldsymbol{x}_{a,TCCON}$ is the a priori profile used in Equation 3.3 and $\boldsymbol{x}_{true}$ is the measured in situ profile in DMF. The in situ profile is interpolated to the same vertical levels as the TCCON a priori profile as shown in Fig. 3.4. After calculating the smoothed in situ profile, we integrate the profile from the surface to the vertical level at which the partial columns are separated, q in Equation 3.5, for the lower column. For the upper partial column, we integrate from the level q+1 to the top of the atmosphere for the upper column using the method outlined in Wunch et al. (2010). We then compare the integrated, smoothed, in situ partial column DMFs directly with the reconstructed lower and upper partial columns calculated by Equation 3.17.

3.2.2.5 Error Calculations

Finally, the error for the retrieval is made up of model parameter error, smoothing error, and retrieval noise (Rodgers, 2008). There are no model parameters in the state vector of the TARDISS retrieval, so the model parameter error is zero. The smoothing error is the square root of the diagonal of the following matrix:

$$\boldsymbol{S}_s = (\boldsymbol{K}^T\boldsymbol{S}_\epsilon^{-1}\boldsymbol{K} + \boldsymbol{S}_a^{-1})^{-1}\boldsymbol{S}_a^{-1}(\boldsymbol{K}^T\boldsymbol{S}_\epsilon^{-1}\boldsymbol{K} + \boldsymbol{S}_a^{-1})^{-1}, \tag{3.25}$$

and the retrieval noise is the square root of the diagonal of the matrix calculated by:

$$\boldsymbol{S}_r = (\boldsymbol{K}^T\boldsymbol{S}_\epsilon^{-1}\boldsymbol{K} + \boldsymbol{S}_a^{-1})^{-1}\boldsymbol{K}^T\boldsymbol{S}_\epsilon^{-1}\boldsymbol{K}(\boldsymbol{K}^T\boldsymbol{S}_\epsilon^{-1}\boldsymbol{K} + \boldsymbol{S}_a^{-1})^{-1}, \tag{3.26}$$

and the sum of the two are the total error for the fit.

In order to report an error for our retrieval that reflects the performance of the retrieval in the validation comparisons in Section 3.3.1, the retrieval output errors are multiplied by a scalar calculated from the 1-to-1 comparisons. Using the multiplier ensures that we are reporting a conservative estimate of the error in the retrieval. We use the 1-to-1 comparisons to scale our error values to the point where at least 50% of the comparison points are within the one standard deviation error range of the 1-to-1 line. We calculate the scalar values as:

$$VEM = Median(\frac{|\hat{\boldsymbol{z}}_{comp} - \hat{\boldsymbol{z}}_s|}{\boldsymbol{\sigma}}), \tag{3.27}$$

where $\hat{\boldsymbol{z}}_{comp}$ is the comparison partial column values, $\hat{\boldsymbol{z}}_s$ is the integrated, smoothed, in situ partial column values, $\boldsymbol{\sigma}$ is the output retrieval errors, and VEM is the calculated validation error multiplier that is unitless. The VEM is calculated and applied to all retrieved errors for each site so that the retrieved dataset for a site reflects the best representative error values. If a calculated VEM is less than one, we use a VEM of one instead to avoid spuriously reducing error values. A complete discussion of the retrieval error is in Section 3.3.4.2.

3.2.3 Algorithm Setup and Choices

3.2.3.1 Pre-processing of the TCCON Data

We begin by preprocessing the TCCON fits. We take the TCCON a priori profile and scale it by the median value of the TCCON output scalar values for each spectrum from the windows used so that our TARDISS fit is centered around the median TCCON a posteriori profile for each measurement point. The a posteriori errors from each window are not included in this calculation but are included in the formation of the measurement covariance matrix. This assumes that the true column-averaged VMR of a species is some linear combination of the VMRs calculated from the windows used in the TARDISS fit. Then, we calculate the a priori partial columns by integrating the scaled a priori profiles

over the respective pressure levels for the upper and lower partial column. Finally, we assemble the necessary matrices for the fit described by Equation 3.16.

3.2.3.2 Maximum a Posteriori Components

The different components of Equation 3.16 reflect where a priori information can be used in the algorithm and several additional choices can be made to improve the fit. The following describes our standard input for these components. We present tests of the retrieval's sensitivity to these choices in Sect. 3.3.2.

For the a priori covariance matrix, $\boldsymbol{S}_a$, we use an identity matrix for the lower partial column scalar portion of the covariance matrix, and we use an exponential decay over the day of measurements from the diagonal for the upper partial column scalar portion of the covariance matrix. This requires that upper column scalar values shift in relation to one another and prevents the upper partial column scalars changing too rapidly in time. The off-diagonal values of the upper partial column portion of the a priori covariance matrix decay with respect to the measurements made before and after them over the course of one-third of a day of measurement. We assume no correlation between the upper and lower partial columns, although this is a place for future study. Since the a priori covariance matrix is inverted in the calculations, decreasing the magnitude of the a priori covariance matrix scalar increases the constraints imposed during the calculations so that a scalar of 10^{-5} is a stricter constraint than a scalar of 10^{-4}. A discussion of the influence of the temporal covariance is in Sect. 3.3.4.1.

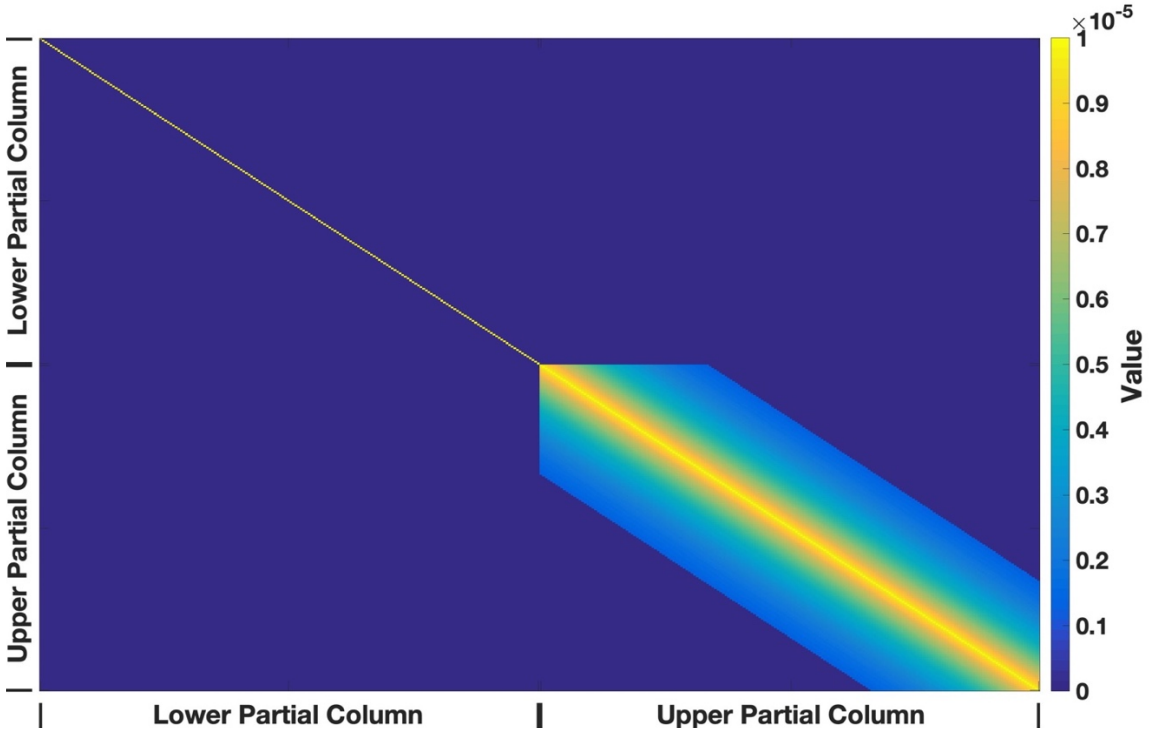

Figure 3.3: Example of an a priori covariance matrix color coded by the magnitude of the value. The axes represent the relationship of the contribution of each measurement to each partial column and each other measurement. The upper right and lower left quadrants are dark blue and represents zero assumed correlation between the upper and lower partial columns over a day of measurements. The diagonal is scaled to constrain the fit and the lower right quadrant shows the assumed correlation between upper partial column scalar values over a day of measurement. The lower partial column has an a priori covariance that is a scaled identity matrix, the upper partial column has an a priori covariance that decays over one third of the measurement day, and the cross covariances between the upper and lower partial columns are assumed to be zero.

The measurement error covariance matrix, $\boldsymbol{S}_{\epsilon}$, is a diagonal matrix composed of the squares of the TCCON errors for each spectral window so that measurements with smaller errors are weighted more heavily than those with larger errors.

CO_2 and CO use different values for the a priori TARDISS scale factors ($\boldsymbol{x}_{a,\gamma}$). For CO, we assume a uniform a priori scale factors of one for all observations. For CO_2 we use the solution to the least-squares method, $\boldsymbol{x}_{L2}$ from Equation 3.15 as $\boldsymbol{x}_{a,\gamma}$ in Equation 3.16. We

adopted different approaches for these two gases since using a static a priori partial column scalar of one for the CO_2 retrievals worsened the comparison to in situ data but improved the validation comparison for the CO retrievals (shown in Sect. 3.3.2).

3.2.3.3 Choosing Spectral Windows for the TARDISS Fit

The primary information content used in our algorithm is derived from the fact that the total column abundances retrieved from different spectral windows of the same species will differ due to differences in their kernels unless the shape of the a priori profile is perfect. Accordingly, for this method to have sufficient information, windows with different vertical averaging kernels are needed, such as those shown in Fig. 3.1. Preferably, the TARDISS retrieval would use a window that is more sensitive to the lower atmosphere and a window that is more sensitive to the upper atmosphere so that a larger amount of information is contained between them. While it is imperative to use windows that have differing averaging kernel profiles, it is also necessary to use windows that have sufficiently low error in the TCCON fit.

For the partial column CO_2 calculations, we use four spectral windows in the TCCON process centered at 6339, 6220, 4852, and 6073 cm^{-1} which were suggested for profile retrieval exploration by Connor et al. (2016). The 6339 cm^{-1} and 6220 cm^{-1} windows are spectroscopically similar and have column averaging kernel profiles that vary with solar zenith angle providing some vertical information over the course of a day (see Fig. 3.1). The 4852 cm^{-1} window has an averaging kernel profile that is largest at the surface and smallest at the upper troposphere and lower stratosphere and the 6073 cm^{-1} window has an averaging kernel profile that is effectively the opposite of the 4852 cm^{-1} window. Both the 4852 cm^{-1} and 6073 cm^{-1} window averaging kernels are largely independent of solar zenith angle with the exception of the highest levels in the 6073 cm^{-1} window profile.

For the partial column CO calculations, we use three spectral windows fit during the TCCON process. There is one window in the NIR region centered at 4233 cm^{-1} and two

windows in the MIR region centered at 2111 and 2160 cm^{-1}. The two MIR windows have similar averaging kernel profiles that maximize at the surface and drop to nearly zero at upper levels. The NIR window averaging kernel profile has a minimum at the surface and a maximum at the upper levels.

Unlike the CO_2 windows that are all observed by the InGaAs detector, the MIR CO windows are measured by a liquid nitrogen cooled InSb detector. For this reason, we only have results of the CO partial column fits at the Caltech, Lamont, and East Trout Lake TCCON sites and, due to the lack of in situ profiling data in Pasadena, we only have direct vertical profile comparison results from the Lamont and East Trout Lake TCCON site.

Other windows output by TCCON retrievals were considered for the partial column calculations for both species. However, they had high levels of error in the TCCON fit or had fits that were particularly sensitive to changes in temperature.

3.2.3.4 Choice of Partial Column Height

We chose the lower partial column to integrate from the surface through the first five vertical layers of the GEOS meteorological fields. Using this criterion, a site at sea level has a lower partial column from sea level to 2 km and the upper partial column from 2 to 70 km. While somewhat arbitrary, the choice of 2 km was made to have the lower partial column encompass the surface mixed layer at most locations while minimizing the dilution of surface exchange signals that would result from integrating over a larger partial column. If there are known significant enhancements species enhancement near the 2 km level (such as CO during wildfire events), the retrieval performance may be degraded, and a different partial column height may be a more appropriate choice.

3.2.4 Sites Used in this Work

In this study, we use data from the five TCCON sites located across North America. The data record extends from as early as 2011 to as recent as 2021 (Table 3.1). These sites are

located at Park Falls, Wisconsin; NASA Armstrong, Edwards Air Force Base, California; Lamont, Oklahoma (the Department of Energy Southern Great Plains Atmospheric Radiation Measurement site), the California Institute of Technology (Caltech), in Pasadena, California, and East Trout Lake, Saskatchewan.

Park Falls, WI hosts the first operational TCCON site (July 2004-present). The site is in a rural, heavily forested area and generally far from anthropogenic influence. The FTS does not have an InSb detector, so we are able to only retrieve partial column values for CO_2. We focus on data obtained since 2012, when the alignment of the instrument has been more consistent. The increased variance of the TARDISS retrieval for data before 2012 likely reflects the inconsistent alignment of the FTS.

We use similar data from the TCCON site located at NASA's Armstrong Flight Research Center (formerly the Dryden Flight Research Center) in California which has been operational since July 2013. We report CO_2 partial column values for the 2013 to 2021 time period. The Armstrong site is on the northwest edge of Rogers Dry Lake within the Edwards Air Force Base in the Mojave Desert.

The Lamont, OK TCCON site is surrounded by farmland. It has been operational since July 2008, and an InSb detector was installed in October 2016. We focus on data from Lamont obtained after 2011 after an issue with the instrument laser was resolved. We report CO_2 partial column values from 2011 to 2021 and CO partial column values from 2017 to 2021.

The TCCON site on the Caltech campus in Pasadena, CA has been operational since July 2012 with an InSb detector measuring since October 2016. We report CO_2 partial column values from 2012 to 2021 and CO partial column values from 2017 to 2021.

The East Trout Lake, SK, TCCON site is located in a remote, heavily forested area in the middle of the Saskatchewan Province. The instrument uses an InSb detector allowing us to

retrieve partial column CO values. It has been operational since October 2016, and we report partial column values for CO and CO_2 from 2017 to 2021.

Site	Location	Dates of Measurements Used	Data DOI
Park Falls, WI	45.945N, 90.273W	CO_2: 2012 - 2021	10.14291/tccon.ggg2020.parkfalls01.R0
NASA Armstrong, Edwards Air Force Base, CA	34.958N, 117.882W	CO_2: 2013 - 2021	10.14291/tccon.ggg2020.edwards01.R0
Lamont, OK	36.604N, 97.486W	CO_2: 2011 - 2021 CO: 2017- 2021	10.14291/tccon.ggg2020.lamont01.R0
Caltech, Pasadena, CA	34.1362N, 118.126W	CO_2: 2012 - 2021 CO: 2017 - 2021	10.14291/tccon.ggg2020.pasadena01.R0
East Trout Lake, SK	54.354 N, 104.987W	CO_2: 2017 – 2021 CO: 2017 – 2021	10.14291/tccon.ggg2020.easttroutlake01.R0

Table 3.1: Location, dates of measurement, and DOIs of the TCCON sites used in this work. CO measurements require an InSb detector to cover the 2160 and 2111 cm^{-1} windows, which has only been available since 2017 at Caltech, Lamont, and East Trout Lake.

3.2.5 Comparison Data

We use in situ data from multiple aircraft programs and AirCore flights between 2008 and 2020 (Cooperative Global Atmospheric Data Integration Project; (2019), Baier et al., 2021) to evaluate our partial column retrieval.

The aircraft CO_2 measurements are from the NASA Studies of Emissions and Atmospheric Composition, Clouds and Climate Coupling by Regional Surveys (SEAC4RS) campaign (Toon et al., 2016) using an AVOCET instrument, from the 2016 Atmospheric Tomography Mission (ATom) (Wofsy et al., 2021; Thompson et al., 2022) using a Picarro cavity ringdown spectroscopy (CRDS) trace gas analyzer (Crosson, 2008), from the Korea-United States Air Quality Study (KORUS-AQ) campaign using a non-dispersive IR spectrometer, and from measurements made by the Goddard Space Flight Center using a Picarro CRDS trace gas analyzer.

We use AirCore profiles from July and August of 2018 at the Armstrong, Lamont, and Park Falls sites (Baier et al., 2021). The AirCore sampling system is composed of coiled stainless-steel tubing that is open on one end while ascending on balloon to ~ 30 km, and passively samples ambient air as it descends to the ground on a parachute. This sample is then analyzed for CO_2, CH_4, and CO using a Picarro CRDS trace gas analyzer, and a fill dynamics model accounts for the effect of longitudinal mixing due to diffusion on vertical resolution (Karion et al., 2010; Tans, 2009; Tans, 2022).

Finally, we use CO and CO_2 data measured at the Lamont site (site code SGP) and at the East Trout Lake site (site code ETL) as a part of the NOAA Global Greenhouse Gas Reference Network (GGGRN) aircraft network in North America (Sweeney et al., 2015). Since these datasets do not include much data within the upper partial column, we compare with these measurements only to our retrieved lower partial column values and exclude them from the validation discussion in Section 3.3.2. Table B.2 provides a summary of the in situ data used in this work.

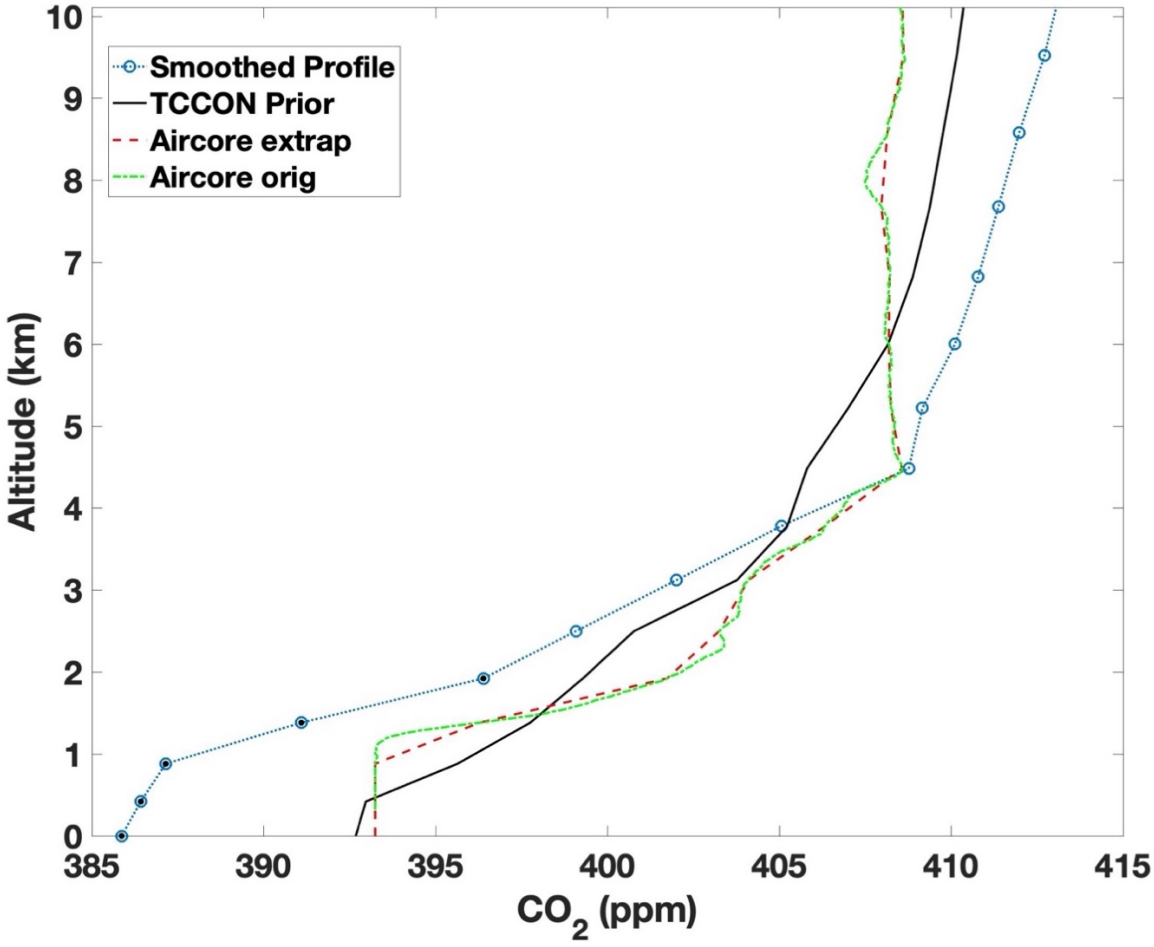

Figure 3.4: An example of the profiles used in the direct comparison calculations using data from the Park Falls site on July 27, 2018. The profile above 10 km is not shown. The solid black line is the TCCON a priori profile scaled by the median of the vertical scaling factors from the spectral windows used. The green dot-dashed line is the measured AirCore mole fraction. The red, dashed line is the AirCore measurements interpolated to the vertical spacing of the TCCON prior, and the blue, dotted line with circles is the smoothed, vertical sensitivity weighted profile that is integrated to calculate the partial column that the TARDISS retrieval would calculate if it had a 'true,' AirCore profile. The black dots within the blue circles represent the points of the profile that make up the lower partial column.

3.3 Results and Discussion

The TARDISS algorithm is very quick — taking only a minute of processing time per year of data for each species — because it does not repeat the spectral fitting. This speed enables the validation comparisons to be performed using many different model choices. Thus, we

evaluated the sensitivity of the TARDISS inversion by varying different forward model choices. The set of choices that we have designated as the operational setup for CO_2 inversion are:

- The covariance matrix, $\boldsymbol{S}_a$, is scaled by 10^{-5} to better constrain the fit
- The value of the a priori scalar for the lower and upper partial column scalar ($\boldsymbol{x}_{a,\gamma}$ in Equation 3.16) is the least squares solution for the respective column ($\boldsymbol{x}_{L2}$ in Equation 3.15).

For the CO inversion, the operational setup parameters are:

- A covariance matrix, $\boldsymbol{S}_a$, scaled by 10^{-4}
- An ideal a priori partial column scalar ($\boldsymbol{x}_{a,\gamma}$) of one.

We vary two aspects of the algorithm and observe the differences in the validation comparisons. The results of these tests are discussed in Sect. 3.3.2 and represented in Table 3.2 and Table 3.3.

3.3.1 Validation Comparisons

We compare retrieved partial column values from three of the five sites presented in this work using measurements from the same set of in situ data used to evaluate and derive the 'in situ scaling factor' of the TCCON retrievals (Wunch et al., 2011). For CO_2, there are twenty-four points of comparison obtained between 2013 to 2018. Twelve of those comparisons are from the Armstrong TCCON site, four profiles are available above the Park Falls TCCON site, and the remaining eight profiles are from the Lamont TCCON site. As the Lamont site is the only site in this work with an InSb detector and overlapping in situ measurements, the eight profiles measured at the Lamont site serve as the totality of the CO comparison dataset.

We also compare the partial columns calculated from the TCCON individual windows to further contextualize the performance of the TARDISS algorithm in Sect 3.3.3.1 and summarized in Table 3.4. The comparisons of the TCCON individual windows are performed in the same way as the TARDISS comparisons using Equation 3.20 to calculate the smoothed, in situ partial columns.

The comparison profiles were measured by aircraft-based instruments or AirCore measurements as described in Sect. 3.2.5 and Table B.2. We revert to the TCCON priors for parts of the profile not measured by in situ methods. For the errors associated with the aircraft measurements, we use the reported measurement error for the measured parts of the profile, and, for the unmeasured parts of the profile, we use the average reported measurement error and, to account for the errors involved with estimating the parts of the profiles not measured by in situ methods, we add in quadrature twice the standard deviation of the measured profile in the respective partial column. For the errors associated with the AirCore measurements, we use the same approach as for the aircraft measurement and include an extra error term to conservatively account for atmospheric variability as captured by duplicate AirCores launched at approximately the same time. The error for AirCore from atmospheric variability is 0.6 ppm for CO_2 and 8 ppb for CO compared to the analyzer error of 0.05 ppm and 3 ppb. The partial column error values are calculated by integrating a profile shifted by the error values and subtracting it from the integration of the original smoothed profile. The difference between these two integrated, smoothed partial columns provides a conservative error value that represents the unlikely occurrence that the profile at every altitude has 100% error.

We compare the TARDISS retrievals from spectra obtained within one hour of the in situ profile to the integrated, smoothed, in situ partial columns calculated using Equation 3.24. We report linear fits between the partial column retrievals and the integrated, smoothed, in situ partial columns. Since our retrieval is designed to be linear, we use fits with y-intercepts forced through zero. As there are only scaling values in our retrieval, a non-zero y-intercept would introduce spurious error into our analysis. Since the reported coefficient

of determination for this linear fit would be spuriously high, we take the ratio of our retrieved partial column to the integrated, smoothed, in situ measurement and subtract one to quantify how much they deviate from each other. We report the mean of the absolute value of the ratio as it deviates from one as the mean ratio deviation. For example, a one percent difference in values would give a mean ratio deviation of 0.01. This mean ratio deviation value gives a more direct understanding of how the partial column values compare.

We use these validation comparisons to perform sensitivity tests of our algorithm parameters and determine an operational set of parameters. We then use these optimal parameters for the CO_2 and CO retrievals to quantify the total error of our retrieval by calculating a validation error multiplier for each site. Validation error multipliers for each site and partial column are shown in Table 3.6.

3.3.2 Choice of Operational Parameters from Validation Comparison

Several terms in our retrieval do not have unambiguously correct values. To evaluate the sensitivity our retrieval to the choices made for these parameters, we have run our retrieval with alternate values and report the degrees of freedom and comparison to in situ data (specifically, the retrieval comparison error, slope of the zero-forced linear fit, and the mean ratio deviation value of the linear fit) for each test. We tested changes to two terms: the TARDISS a priori scale factors and the a priori covariance matrix scaling.

To test the sensitivity of the retrieval to the partial column scalar prior, we compare the changes in the validation when using $\boldsymbol{x}_{L2}$ from Equation 3.15 as the a priori partial column scalar (our operational choice for CO_2), the daily median of $\boldsymbol{x}_{L2}$, as well as the idealized scalar of unity (our operational choice for CO) to each other. In Tables 3.2 and 3.3, these are identified as "$\boldsymbol{x}_{L2}$," "$\boldsymbol{x}_{L2}$ daily median," and "static ideal prior," respectively.

We also test the sensitivity of the retrieval to how the a priori covariance matrix is scaled. This term changes how strongly the retrieval is constrained to the prior. In Table 3.2 (CO_2) and Table 3.3 (CO), we illustrate the influence of choosing $1x10^{-4}$, $5x10^{-5}$, and $1x10^{-5}$ as an a priori covariance matrix scalar. While other scaling values were tested, the resulting errors were large enough or the resulting degrees of freedom were small enough that the values were disregarded from further study.

TARDISS a priori Choice	A priori Covariance Matrix Scaling	DoF per measurement (overall)	Lower Column Error (ppm)	Lower Column Validation Slope	Lower Column Mean Ratio Deviation	Upper Column Error (ppm)	Upper Column Validation Slope	Upper Column Mean Ratio Deviation
$\boldsymbol{x}_{L2}$ daily median	10^{-5}	0.046 (2.12)	1.146	1.004	0.008	0.497	0.999	0.003
	10^{-4}	0.311 (15.1)	3.063	1.006	0.010	1.033	0.999	0.003
	$5x10^{-5}$	0.183 (8.48)	2.378	1.005	0.010	0.658	0.999	0.003
$\boldsymbol{x}_{L2}$	10^{-5}*	0.046 (2.12)	1.146	1.001	0.011	0.497	0.999	0.002
	10^{-4}	0.311 (15.1)	3.063	1.004	0.011	1.033	1.000	0.002
	$5x10^{-5}$	0.183 (8.48)	2.378	1.003	0.009	0.658	1.000	0.002
Static ideal prior	10^{-5}	0.046 (2.12)	1.146	1.012	0.014	0.497	0.997	0.003
	10^{-4}	0.311 (15.1)	3.063	1.013	0.010	1.033	0.997	0.003
	$5x10^{-5}$	0.183 (8.48)	2.378	1.013	0.013	0.658	0.997	0.003

Table 3.2: Variations in CO_2 retrieval upper and lower column validation slopes, upper and lower column mean ratio deviations, upper and lower column comparison errors, and DoF for different TARDISS a priori choices and a priori covariance matrix scaling values. The asterisk in the fourth row indicates that this is the operational set of parameter choices for the CO_2 retrieval.

The agreement between the in situ and TARDISS retrievals for CO and CO_2 change with both the a priori covariance matrix scaling and the a priori scalar choice. As we are trying to determine the parameters that give the best comparison results between the in situ and lower partial column retrieval data specifically, we chose the parameters that resulted in the validation slope closest to one for the lower partial column. For the lower partial column CO_2, the best result (slope of 1.001) comes from using the $\boldsymbol{x}_{L2}$ values as an a priori scalar and scaling the a priori covariance matrix by 10^{-5}. The validation slope for the upper column comparison with these parameters (0.999) is similar to values from other parameter choices. For the lower partial column CO, the best result for the lower column (slope of 0.999) results from the retrieval using a static a priori scalar of one and scaling the a priori covariance matrix by 10^{-4}. Over the two hours of the comparison, the degrees of freedom are about 2.12 for CO_2 and 3.51 for CO — consistent with between one and two DoF per hour of measurements. Since the largest variation in validation slopes in either partial column and either species is driven by the change in the a priori partial column scalar, we posit that the a priori partial column scalar choice is the most significant parameter in the retrieval for determining validation slopes while the a priori covariance matrix scaling is the most significant parameter for determining the degrees of freedom of the fit and the retrieval errors.

TARDISS A priori Choice	A priori Covariance Matrix Scaling	DoF per measurement (overall)	Lower Column Error (ppb)	Lower Column Validation Slope	Lower Column Mean Ratio Deviation	Upper Column Error (ppb)	Upper Column Validation Slope	Upper Column Mean Ratio Deviation
$\boldsymbol{x}_{L2}$ daily median	10-5	0.010 (0.402)	0.440	0.935	0.055	0.182	1.099	0.100
	10-4	0.088 (3.51)	1.334	0.938	0.052	0.370	1.122	0.128
	5x10-5	0.047 (1.88)	0.965	0.937	0.053	0.303	1.116	0.120
$\boldsymbol{x}_{L2}$	10-5	0.010 (0.402)	0.440	0.918	0.076	0.182	1.113	0.115
	10-4	0.088 (3.51)	1.334	0.921	0.074	0.370	1.133	0.142

	5x10-5	0.047 (1.88)	0.965	0.920	0.075	0.303	1.128	0.134
Static ideal prior	10-5	0.010 (0.402)	0.440	0.996	0.003	0.182	1.048	0.050
	10-4*	0.088 (3.51)	1.334	0.999	0.005	0.370	1.081	0.081
	5x10-5	0.047 (1.88)	0.965	0.998	0.004	0.303	1.073	0.075

Table 3.3: Variations in CO retrieval upper and lower column validation slopes, upper and lower column mean ratio values, upper and lower column comparison errors, and DoF for different TARDISS a priori choices and a priori covariance matrix scaling values. The asterisk in the second to last row indicates that this is the operational set of parameter choices for the CO retrieval.

3.3.3 TARDISS Performance Using Operational Parameters

3.3.3.1 Comparisons with Calculated TCCON Partial Columns

We compare the validation performance of the TARDISS partial column retrievals to the partial column validations of the TCCON individual windows used in the retrieval to demonstrate that TARDISS provides addition information about vertical distribution compared to the TCCON retrieval. We compute a partial column from the TCCON output by integrating the posterior TCCON CO or CO2 profile (i.e. the prior profile times the retrieved TCCON VSF) over the same pressure levels as the partial columns are calculated over for TARDISS. We compare the TCCON partial columns to the integrated, averaging kernel-smoothed, in situ partial columns calculated using Equation 3.20. The comparisons are shown in Table 3.4 and the slopes of the TCCON window partial column comparisons are shown as dotted lines in Fig. 3.5.

The comparisons show that the TARDISS retrieved partial columns for CO_2 have lower and upper partial columns slopes closer to one than the TCCON input windows. The mean ratio deviation for the lower column CO_2 is slightly larger than the mean ratio deviation for the TCCON input windows (0.011 compared to a TCCON average of 0.007) which is reflected in the error of the lower partial column CO_2 retrieval. The retrieved lower partial

column for CO has a slope much closer to one than the slopes of the TCCON input and with a much smaller mean ratio deviation (0.002 compared to a TCCON average of 0.024). The retrieved upper partial column CO has a slope that is between the slopes of the TCCON input windows but still has a smaller mean ratio deviation suggesting increased precision.

These comparisons suggest that, for CO, the TARDISS algorithm is very effective at separately inferring the lower partial column CO values since the validation slope is closer to one and the mean ratio deviation is smaller than the individual windows. The algorithm is limited in its retrieval of the upper partial column CO which is shown by its direct comparisons and mean ratio deviation being similar to the TCCON input window partial column. The performance of the algorithm suggests that the large variations in the CO vertical profile shapes benefit from the increased flexibility in the lower column but that there might be some spectroscopic biases to correct, particularly in the mid infrared windows.

For CO_2, the comparisons show that the algorithm can effectively infer upper partial column values but is less effective at retrieving the lower partial column CO_2 values. The lower partial columns benefit from the secondary scaling as they have less bias (a slope closer to one) than the individual windows but the slight increase in mean ratio deviation suggests that the retrieval cannot be as precise at adjusting for the surface errors in the a priori profile shape. The a priori profiles for CO_2 intentionally do not include variations of local sources or sinks at the surface but are quite accurate in the middle and upper troposphere. Accordingly, the secondary scaling of the upper partial column has improved accuracy and precision compared to the individual windows.

Finally, we compare the performance of the total column values calculated from the TARDISS scaled partial columns to the total column validations of the TCCON individual windows. The comparisons are shown in Fig. B.3 and summarized in Table B.3. The total column comparisons show similar trends as the upper column comparisons. This is likely

due to the upper partial column vertical sensitivity being much larger than the lower partial column sensitivities as is discussed in Sect. 3.3.4.1.

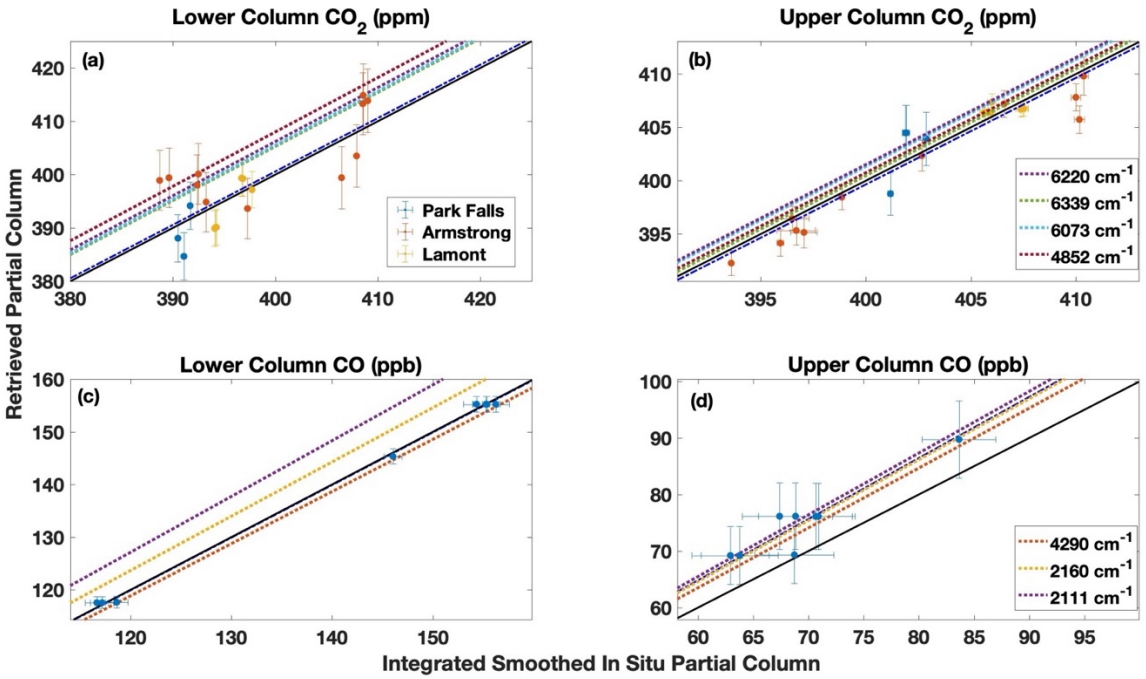

Figure 3.5: The direct comparisons between the partial column DMF values retrieved from the TARDISS fit and the integrated, smoothed in situ partial columns for CO_2 (a,b) and the CO (c,d) for the lower (a,c) and upper (b,d) columns. The CO_2 comparisons are color coded by site and the CO comparisons are solely from the Lamont site. The error bars in the x-direction are the reported errors from the aircraft data smoothed the same way as the in situ measurements and the error bars in the y-direction are the output errors from the TARDISS fit scaled by the VEM values. The black solid line is the 1-1 line and the blue dot-dash line is the linear fit of the data with the y-intercept forced through zero. The blue dot-dash line for the lower partial column CO fit is overlapping with the solid black line. The slopes of the partial column validation of the TCCON spectral windows used in the retrieval are represented by dashed lines.

TCCON Window (cm^{-1})	Lower Column Validation Slope	Lower Column Validation Slope Error	Lower Column Mean Ratio Deviation	Upper Column Validation Slope	Upper Column Validation Slope Error	Upper Column Mean Ratio Deviation
CO_2						
6220	1.016	0.004	0.007	1.004	0.0010	0.003
6339	1.013	0.004	0.005	1.001	0.0009	0.003
6073	1.014	0.004	0.009	1.003	0.0011	0.003
4852	1.020	0.006	0.007	1.002	0.0011	0.004
TARDISS CO_2	1.001	0.003	0.011	0.999	0.0008	0.002
CO						
4290	0.990	0.034	0.041	1.058	0.077	0.106
2160	1.031	0.019	0.052	1.077	0.024	0.095
2111	1.059	0.020	0.061	1.092	0.023	0.108
TARDISS CO	0.999	0.002	0.005	1.081	0.012	0.081

Table 3.4: Comparisons of the TARDISS partial column retrieval to the partial column comparisons of the fits of the TCCON spectral windows from TCCON used as input for the TARDISS algorithm. The data in the TARDISS row uses the operational parameters for the fit that are identified in Table 3.2 and 3.3 by an asterisk.

3.3.3.2 Comparisons with Low Altitude In Situ Profiles

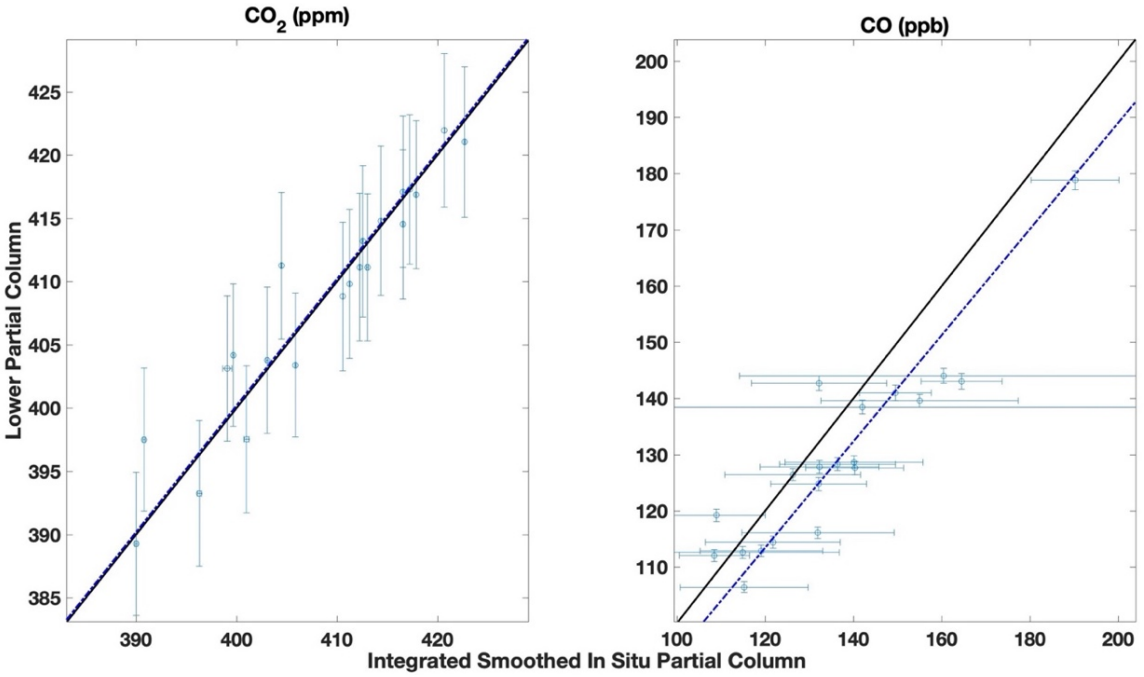

Figure 3.6: East Trout Lake site direct comparisons between the partial column DMF values retrieved from the TARDISS fit and the integrated, smoothed aircraft partial columns for lower column CO_2 and CO. The error bars in the x-direction are the integrated partial columns of the profile shifted by the error values and then subtracted from the original partial column integration. The error bars in the y-direction are the output errors from the TARDISS fit scaled by the VEM value for the site. The black solid line is the 1-1 line and the blue dot-dash line is the linear fit of the data with the y-intercept forced through zero. The slope for the fit is 1.001±0.002 for CO_2 and is 0.945±0.012 for CO.

In addition to the aircraft and AirCore validation data that include profile measurements at altitudes in the upper troposphere and lower stratosphere, we compare to aircraft data obtained as part of the NOAA GGGRN aircraft program at the Lamont and East Trout Lake sites. These measurements were made more frequently but do not include enough high-altitude measurements to compare with our retrieved upper partial column values, so we use them as an independent comparison to our validation data for our lower column CO_2 and CO retrievals. We use data obtained between the surface and 7 km from 26 of the 40 flights made between 2017 and 2020 at East Trout Lake. We also use data obtained between the surface and 6 km from 267 of the 399 flights performed at the Lamont site over the period of 2008 to 2018 and all 34 flights for CO made between 2017 and 2021.

Figure 3.6 (East Trout Lake) and Fig. 3.7 (Lamont) show the retrieved lower partial column DMF plotted against the integrated, smoothed, in situ columns similar to Fig. 3.5.

Similar to the validation comparison, we revert to the a priori profile for altitudes not measured by in situ methods. To account for the errors in using the a priori profile, we add twice the standard deviation of the partial column that is measured to the average measurement error in quadrature. Given the lower altitudes measured by the GGGRN program, the errors associated with the parts of the profile that use the a priori profile are higher and, therefore, the errors in the long-term comparative measurements tend to be much higher than the validation measurements as shown in the CO comparisons in Fig 3.6.

Despite the larger error values, the consistency of the statistical parameters (summarized in Table B.4) using the larger number of measurements in the long-term comparisons further motivates the use of the extended validation dataset. Some of the in situ profile comparisons occur during times with larger CO DMFs that suggest influences from sources not accounted for by the TCCON a priori profiles such as those from wildfires which likely resulted in the large VEM for the long-term CO comparisons. Although the comparisons with the long-term data are not used for validation, the long-term comparisons show that the validation comparisons are generally representative of the performance of the TARDISS algorithm overall.

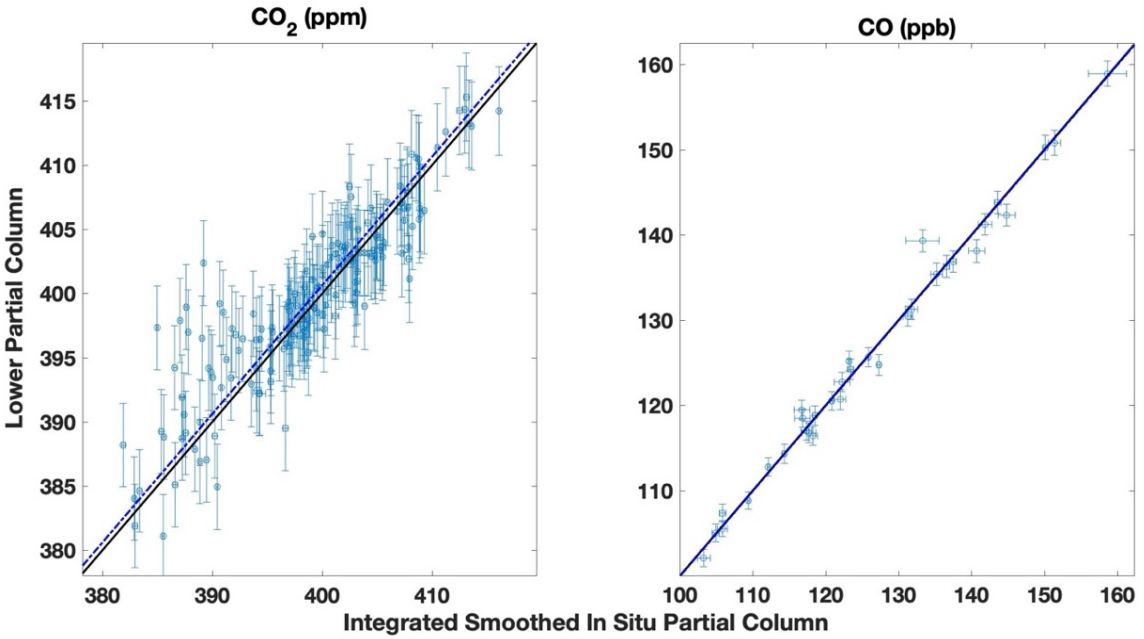

Figure 3.7: Lamont site direct comparisons between the partial column DMF values retrieved from the TARDISS fit and the integrated, smoothed airborne partial columns for lower column CO_2 and CO. The error bars in the x-direction are the integrated partial columns of the profile shifted by the error values and then subtracted from the original partial column integration. The error bars in the y-direction are the output errors from the TARDISS fit scaled by the VEM value for the site. The black solid line is the 1-1 line and the blue line is the linear fit of the data with the y-intercept forced through zero. The slope for the fit is 1.002±0.001 for CO_2 and is 1.000±0.002 for CO.

3.3.4 Retrieval Characterization

3.3.4.1 TARDISS Vertical Sensitivity and Temporal Covariance

TARDISS uses an a priori covariance matrix with temporal covariance between upper partial column scalars over the course of a day of measurement, as shown in Fig. 3.3. To determine how this constraint influences the retrievals, we compare the data above to the validation comparison from a CO_2 retrieval not constrained by a temporal covariance. The a priori covariance matrix without the temporal covariance is simply a diagonal matrix of the 10^{-5} scalar value. Table 3.5 shows that the retrievals without temporal constraints have a slightly poorer validation comparison overall, including larger errors and fewer degrees of freedom. However, the site-by-site differences in validation data show that the upper

column VEM values are smaller when using a temporally unconstrained fit, whereas the lower column VEM values are improved when implementing the temporal constraints. While the purpose of this study is to create a universally-applicable operational algorithm, local differences in the sources and meteorology may alter the effects of the a priori covariance matrix choice on the site VEMs. This suggests that site-by-site parameter choices may enable smaller errors and increased precision.

	Statistics	Temporally Constrained Upper Column	Temporally Unconstrained Upper Column
Validation DoF (Overall)		0.0462 (2.12)	0.0352 (1.59)
Lower Column CO_2			
	Error (ppm)	1.15	1.15
	Validation Slope	1.001	1.002
	Mean Ratio Deviation	0.011	0.009
	Park Falls VEM	3.25	3.75
	Armstrong VEM	2.98	4.42
	Lamont VEM	1.35	2.50
Upper column CO_2			
	Error (ppm)	0.497	0.956
	Validation Slope	0.999	0.998
	Mean Ratio Deviation	0.002	0.003
	Park Falls VEM	3.61	1.92
	Armstrong VEM	4.63	1.66
	Lamont VEM	2.70	1

Table 3.5: Validation comparison DoF, error, validation slope and mean ratio deviation and site VEM values for lower and upper column CO_2 for retrievals using a temporally constrained upper column and a temporally unconstrained upper column. The retrievals are performed with the operational parameters denoted by asterisks in Table 3.2.

The temporal covariance impacts our validation comparison through the partial column vertical sensitivities described in Equation 3.22 via the gain matrix (Equation 3.21). To assess the importance of the choice of a priori covariance matrix, we compare the vertical

sensitivities for a temporally constrained upper column and a temporally unconstrained upper column (shown in Fig. 3.8) for a representative day (July 27th, 2018, at the Lamont site).

Without the temporal constraint, the upper column sensitivities are on the same order as the lower column sensitivities with values between -0.05 and 0.18. The upper column sensitivity peaks around the 15 km level at low solar zenith angles and the peak moves toward the surface at higher solar zenith angles consistent with the changing kernel of the 6220 and 6339 cm^{-1} bands. The lower column sensitivities always peak near the surface (~2 km or below) and the sensitivity increases at higher solar zenith angles.

With the temporal constraint, the altitude of the maximum sensitivities with respect to SZA remains similar but the upper column sensitivities are roughly twice the value and the lower column sensitivities are half the value as the temporally unconstrained values. The imposed temporal covariance constrains the upper column to vary slowly over the span of a measurement day so that a change in the column at one measurement point induces changes at other measurement points, thereby increasing the vertical sensitivities in the upper column over the entire day. This constraint is also stringent enough that it propagates into the sensitivity of the lower column scalar. Since our goal is to retrieve a lower partial column, it seems counterintuitive that using sensitivities with an order of magnitude difference provides a better validation comparison. However, for this method we assume that we know the shape and behavior of the upper column fairly well and that most of the change occurs near the surface. Given these assumptions, constraining the upper column more heavily by introducing expected daily patterns through the a priori covariance matrix allows for the lower column retrieval to have improved comparisons with in situ data despite the decreased vertical sensitivities.

While we test retrievals simply with and without temporal covariance, the possible choice of a priori covariance matrix shape could be much more complex. Future study could include using model generated or back trajectory based temporal covariances to include

outside information in the retrieval dynamically. For an operational retrieval product, we will include the temporal covariance in the a priori covariance matrix as an operational parameter.

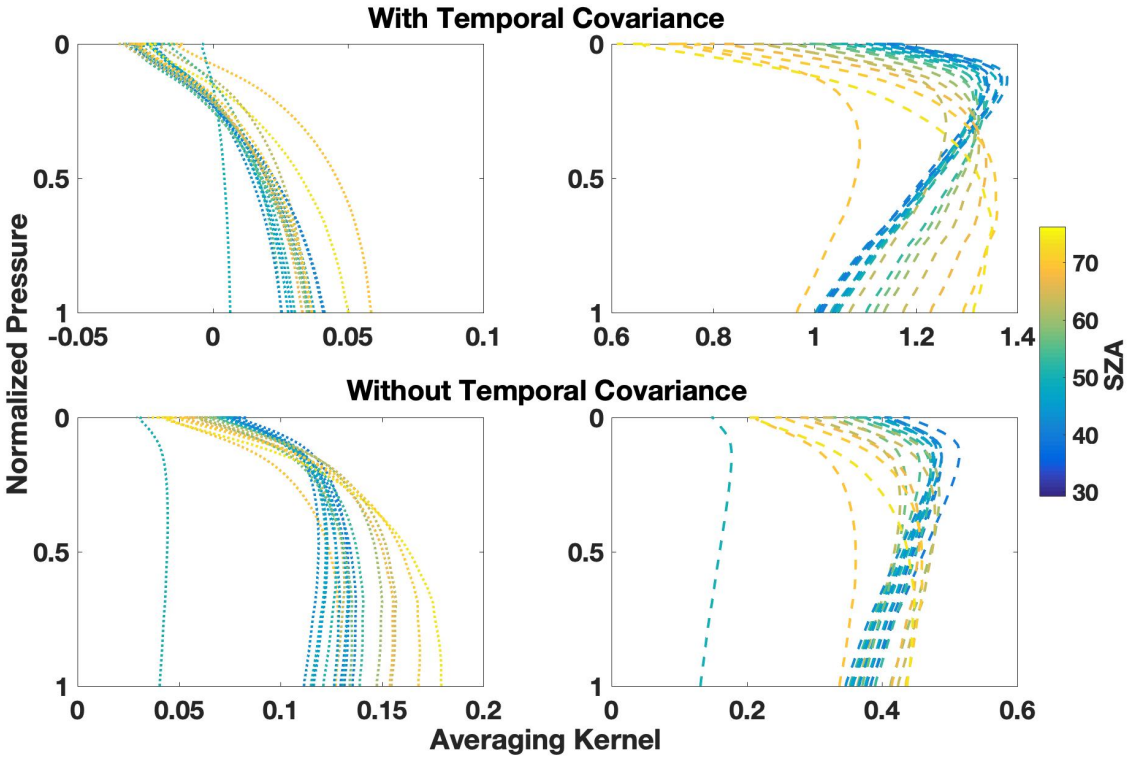

Figure 3.8: Vertical sensitivities of the lower partial column (left column) and upper partial column (right column) scalars color coded by solar zenith angle in degrees. The sensitivities calculated when using a temporally covariant a priori covariance matrix are shown in the top row and when using a non-temporally covariant a priori covariance matrix are shown in the bottom row.

3.3.4.2 Error Analysis

Using the information from the validation comparison, we can evaluate the errors of the entire dataset from each of the five sites. The output of the retrieval is the partial column scalar and the error retrieved is the standard deviation of the partial column scalar calculated from the retrieval variance and represented as another scalar value. To convert our partial column scalar error to a dry air mole fraction, we multiply the error scalar value by the a priori partial column mixing ratio ($z_{a,TCCON}$ in Equation 3.17). Error varies from

site to site due to variations in the TCCON total column errors that are input to the measurement covariance matrix and due to how well the a priori partial column DMF matches the (generally unknown) actual partial column DMF. We report the total retrieval error, retrieval error components, and the error contribution from the validation comparison measurements in Table 3.6.

The retrieval error values range from 1.16 ppm to 1.41 ppm for lower column CO_2 and from 0.26 ppm to 1.33 ppm for the upper column CO_2. For CO retrievals, the average total retrieval error ranges from 0.48 ppb to 14.0 ppb for the lower column and 0.032 ppb to 2.23 ppb for the upper column. In general, the errors vary minimally over the record, but there is a distinct seasonality for both lower column CO and CO_2 retrievals with the highest errors during the summer perhaps as a result of errors in the near surface a priori profiles (Fig. B.4). The absolute errors for CO_2 generally increase over time since simply because CO_2 is increasing due to anthropogenic emissions. Fractionally, the errors remain similar across the dataset for both CO and CO_2 (Fig. B.5).

Because the model parameter error goes to zero in our implementation, the current total retrieval error is the square root of the sum of the smoothing error (Equation 3.25) and the retrieval noise (Equation 3.26). The smoothing error is 94.0% to 96.5% of the total retrieval error on average for CO_2 and 81.6% to 87.8% of the total retrieval error on average for CO depending on the site and is directly related to the scaling of the a priori covariance matrix. While using a more constrained a priori covariance matrix increases the smoothing error, it also results in a reduction to the total retrieval error. Furthermore, the fit of the lower partial column CO_2 benefits from a stronger constraint since the slope of the lower partial column CO_2 validation is closest to one when using the tightest covariance matrix as shown in Table 3.2. The retrieval noise is 3.5% to 6.0% of the total retrieval error on average for CO_2 and 18.4% to 12.2% of the total retrieval error on average for CO depending on the site and has the opposite relationship to the scaling of the a priori covariance matrix. The retrieval noise reflects the effect of the model covariance matrix that is composed of the

TCCON total column measurement errors and therefore reducing these errors would also reduce the retrieval noise.

Using the operational setup for our TARDISS fit, we calculate the site specific VEM values using Equation 3.27 (Tables 3.5 and 3.6). These values are used to scale the error of the TARDISS fit for all the comparisons in this work. The VEM scaled errors serve as a conservative estimate for the retrieval errors and should be reevaluated with additional in situ profile measurements as they become available. For CO_2 at Park Falls, the lower and upper column VEM are 3.61 and 3.25, at Armstrong, the lower and upper column values are 4.63 and 2.98, and at Lamont the values are 2.70 and 1.35 for the lower and upper column, respectively. Since Caltech and East Trout Lake do not have comparison data, we apply error multiplier values of 4.63 and 3.25 as they are the largest multiplier values from among the other sites. For CO, the Lamont site multiplier values are 1.00 and 15.4, which we use for the Caltech and East Trout Lake site CO retrieval data as well.

Since the TARDISS retrieval cannot fully optimize the shape of the partial profile, the site-to-site differences in VEM are likely due to the variation in the accuracy of the TCCON priors which by design do not capture the local source, sink, and transport complexities. For CO_2, the upper column VEM and retrieval error values are consistently smaller than the associated lower column values suggesting that these data support the assumption that the shape of the profile of the upper partial column is generally much more accurately captured by the TCCON priors.

The total error for each site is determined by multiplying the retrieved errors by the site and partial column respective VEM values. After implementing the VEMs, the errors for the lower partial column CO_2 retrieval range from 3.38 ppm to 5.88 ppm and from 1.22 ppb to 1.96 ppb for CO across all sites and data. As the Caltech and East Trout Lake sites have no validation comparisons, we use the largest validation error multiplier (that of the lower column Armstrong and upper column Park Falls comparison) as a higher bound.

Since the overall biases are small with validation slopes close to one, the errors are sufficiently small that the TARDISS retrievals have skill in evaluating CO_2 fluxes at TCCON sites. The error compared to the overall lower partial column DMF is small, 1.25% on average across the five sites for CO_2.

Site	Retrieval Noise (% of total)	Smoothing Error (% of total)	Mean Lower/Upper Column Retrieval Error (ppm for CO2; ppb for CO)	Lower/Upper Column Validation Error Multiplier (unitless)	Mean Total Lower/Upper Column Error (ppm for CO_2; ppb for CO)
CO_2 Retrievals					
Park Falls	3.5	96.5	1.257/0.655	3.61/3.25	4.54/2.13
Armstrong	6.0	94.0	1.253/0.500	4.63/2.98	5.80/1.49
Lamont	4.5	95.5	1.252/0.582	2.70/1.35	3.38/0.786
Caltech	4.5	95.5	1.271/0.568	4.63/3.25	5.88/1.85
East Trout Lake	5.4	94.6	1.268/0.514	4.63/3.25	5.87/1.67
CO Retrievals					
Lamont	12.2	87.8	1.34/0.447	1.00/15.4	1.34/6.88
Caltech	18.4	81.6	1.96/0.318	1.00/15.4	1.96/4.90
East Trout Lake	15.7	84.3	1.22/0.355	1.00/15.4	1.22/5.47

Table 3.6: Errors in the CO and CO_2 lower partial column retrievals of each site shown as the average of the entire data time series and broken down into total retrieval error, retrieval noise, smoothing error, validation error multiplier, and total error. The values for total retrieval error and total error represent one standard deviation.

3.3.4.3 Information Content Analysis

The information content of the retrieval is determined by the DoF and Shannon information content (H) of the retrieval, each calculated from the averaging kernel. The DoF represent

the independent pieces of information that can be retrieved from a measurement. We report our DoF values both normalized by the number of measurements made in a day, as well as the daily overall DoF. Since the DoF are calculated as the trace of the averaging kernel, we isolate and report the DoF from the upper and lower column separately along with the total. The Shannon information content is a single value to represent the effectiveness of the retrieval to recover information from the model with respect to the variance in the data. Higher Shannon information content values correspond to a retrieval with a higher possible effectiveness.

The information content is summarized for each site in Table 3.7. The overall average lower column DoF per measurement across all sites and collected data is 0.047 for CO_2 and 0.15 for CO. The lowest DoF average value of 0.034 is in Park Falls and the highest DoF average value of 0.061 is in Armstrong for CO_2 and, between the three sites with CO retrievals, Caltech has the highest average lower column DoF of 0.18 compared to 0.12 for Lamont and 0.15 for East Trout Lake. The retrievals of CO have much larger DoF compared to CO_2 primarily since the CO_2 requires a stronger scaling constraint of the a priori covariance matrix limiting the amount of information that can be inferred.

Ideally, DoF values greater than one are desired for traditional profile retrievals. However, the temporal aspect of our retrieval complicates the discussion. If we consider the CO_2 retrievals, the five sites used in this work made an average of 172 measurements per day so that the DoF value average of 0.0470 per measurement yields 8.08 independent pieces of information about the lower partial column per day which provides significant information on the diurnal variation and the fluxes into and out of the lower column.

The information content shown in the DoF are mirrored in the Shannon information content. Similar to the DoF, Park Falls has the lowest and Armstrong has the highest Shannon information content on average for CO_2. These differences are likely driven by the combination of the TCCON retrieval errors and how well the a priori covariance matrix matches the temporal aspects of local meteorology, such as cloud cover or upper

tropospheric transport, or the magnitude and time scales of the local carbon fluxes in the boreal forest versus the lack of such fluxes in the Mojave Desert. For CO, the Caltech retrieval has the highest DoF and Shannon information content of the three sites. While the differences in Shannon information content and DoF between sites are not necessarily directly comparable, these differences also might be due to the TCCON retrieval errors and how well the chosen a priori covariance matrix constrains the solution.

Site	Total Degrees of Freedom per Measurement (per day)	Lower Column DoF per Measurement (per day)	Upper Column DoF per Measurement (per day)	Average Measurements per day	Shannon Information Content per day
CO_2 Retrievals					
Park Falls	0.151 (14.0)	0.0338 (4.30)	0.117 (9.72)	116	9.96
Armstrong	0.165 (33.2)	0.0613 (14.3)	0.104 (18.9)	227	24.7
Lamont	0.163 (20.6)	0.0444 (7.22)	0.119 (13.4)	155	15.0
Caltech	0.156 (23.1)	0.0452 (8.45)	0.111 (14.7)	180	17.0
East Trout Lake	0.181 (25.5)	0.0503 (10.2)	0.131 (15.3)	181	19.0
Overall	0.163 (23.2)	0.0470 (8.89)	0.116 (14.4)	172	17.1
CO Retrievals					
Lamont	0.236 (26.1)	0.123 (15.7)	0.113 (10.4)	120	17.5
Caltech	0.227 (43.6)	0.184 (36.9)	0.0431 (6.76)	194	26.8
East Trout Lake	0.263 (43.4)	0.146 (29.5)	0.113 (13.8)	178	26.2
Overall	0.242 (37.7)	0.151 (27.4)	0.0910 (10.3)	164	23.5

Table 3.7: Degrees of freedom per measurement (and per day) for the lower column, upper column, and total retrieval, in addition to the Shannon information content separated by site for the CO and CO_2 retrievals.

The informational content of the retrieval assists in evaluating the TARDISS algorithm, but also serves as a diagnostic of the effectiveness of the retrieval for each day of measurement. Figure 3.9 shows the long-term comparisons between the retrieved lower partial column and the smoothed, integrated, in situ data at the Lamont site color-coded by the DoF per measurement for each point. The comparisons with higher DoF per measurement generally sit closer to the 1-to-1 line as expected and suggest that days with higher DoF per measurement have lower associated VEM. Figure B.7 shows the VEM calculated after removing days that have DoF per measurement values below a specific threshold. The VEM calculated for the long-term comparison data decreases consistently with increasing DoF filters until it reaches one at ~0.07 DoF per measurement. This, however, excludes roughly 90% of the data. As a first step, the data could be filtered for low DoF or low Shannon information content. In the future, the information content could be used to create more dynamic VEM values for our datasets and provide more precise error values than the conservative, static VEM per site reported in Table 3.6.

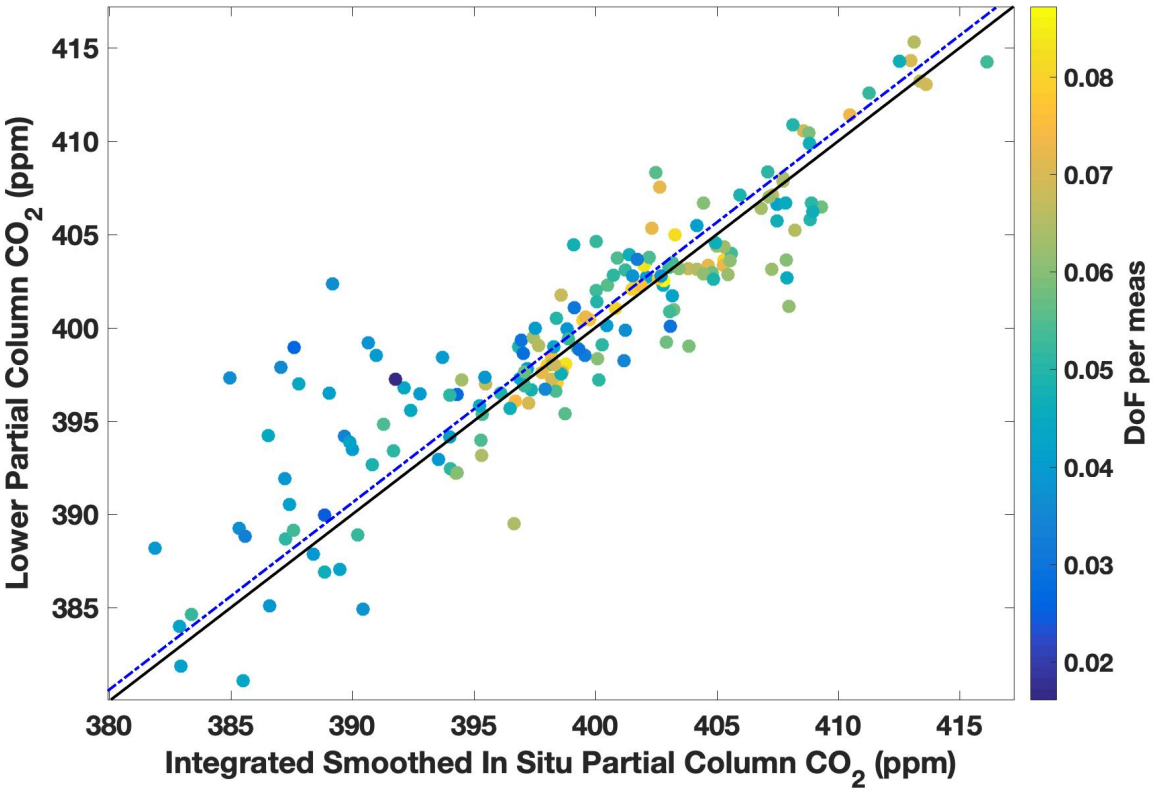

Figure 3.9: The same comparison shown in Fig. 3.7 is shown here without error bars and color coded by the DoF per measurement for the comparison day retrieval. The blue dot-dash line above the black 1-to-1 line is the linear fit of the data with the y-intercept forced through zero with a slope of 1.002±0.001.

3.3.5 Time Series of the TARDISS Retrieval

The TARDISS algorithm is applicable to any spectra reported as TCCON data with the correct detector requirements (InGaAs for CO_2 and both InGaAs and InSb for CO). Overall, there are at least nine years of CO_2 data at each site in this work and approximately five years of CO data at the East Trout Lake, Lamont, and Caltech sites.

Figure 3.10 shows the monthly mean lower and upper partial column data retrieved from spectra obtained over the last decade at the North American TCCON sites. These upper columns reflect the global seasonal patterns in CO_2. The lower column at Park Falls and East Trout Lake reflect the local influences on CO_2 in the sharp decline in surface CO_2 when the surrounding forest is most photosynthetically active. In contrast, the lower column Caltech trace shows a consistent urban enhancement over the global trends of ~5 ppm. All five upper column traces are generally consistent with one another and have a ~6 ppm seasonal fluctuation.

Figure 3.11 shows the monthly median retrieved lower and upper partial column CO data from the East Trout Lake, Lamont, and Caltech site. We observe a slight seasonality at each site with maximums in the winter months and minimums in the summer months. The CO lower partial column data from the Caltech site tends to be larger than those from the Lamont site due to the urban enhancement despite the recent decreasing trend. An example of effect of the urban enhancement on total and partial column values is shown in Fig. B.8.

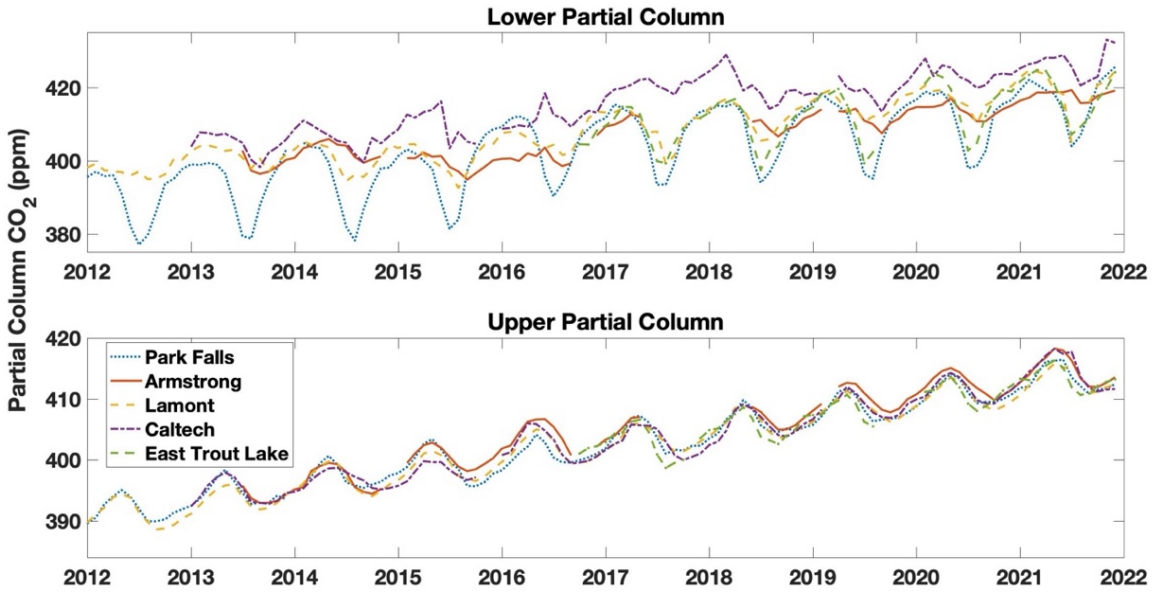

Figure 3.10: Time series plot of the monthly median lower (top) and upper (bottom) partial column values of CO_2 in ppm for the five sites used in the work from 2012 (or the start of measurement) to the end of 2021. Data from before 2012 measured in Park Falls and 2011 in Lamont are not used due to instrument alignment issues and laser issues.

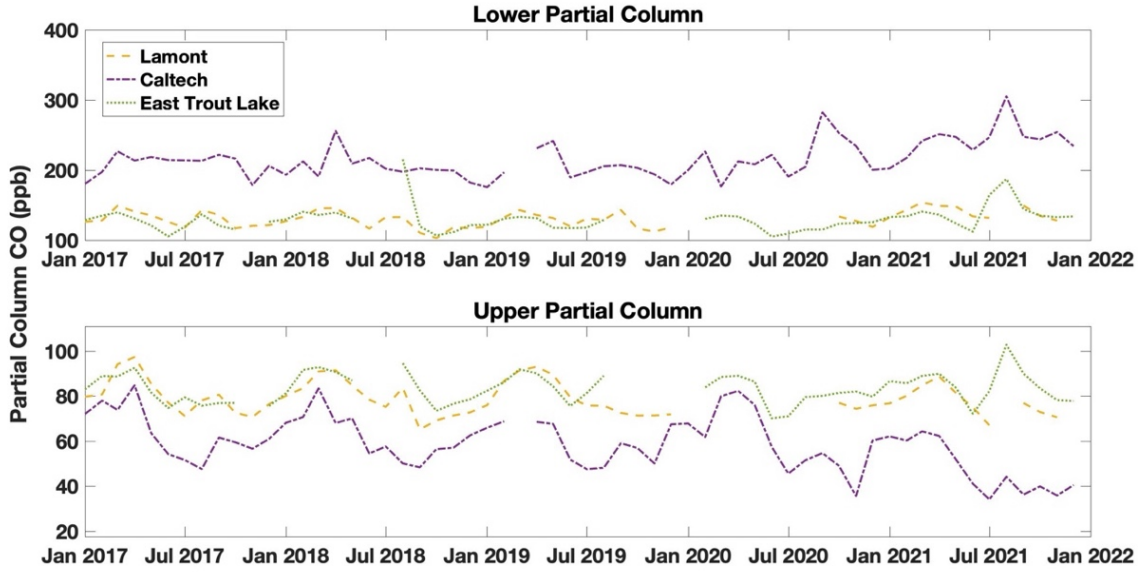

Figure 3.11: Time series plot of the monthly median lower (top) and upper (bottom) partial column values of CO in ppb for the three sites used in the work that have the InSb detector from 2017 to the end of 2021. CO has been declining in most of the US cities due to emissions control technologies.

3.4 Conclusions

The TARDISS retrieval algorithm enables partial column information to be derived from the TCCON total column observations of CO_2 and CO derived from different absorption bands with different vertical averaging kernels. Compared to traditional vertical retrieval approaches, the algorithm relaxes the requirement of very accurate meteorology knowledge, is less biased by spectroscopic errors, and is computationally inexpensive to run since it does fit spectra directly. By inferring information from the differences between total column DMF values from spectral windows that are quality controlled, the retrieval is restricted to imposing small changes to the partial and total columns. This effectively limits the amount of informational content that can be retrieved but also mitigates the issues of oscillation or large deviations in the retrieved vertical profile, partial columns in this case. Finally, this algorithm takes advantage of the temporal dimension by fitting over an entire day of measurements to retrieve enough information to infer temporal changes in the lower (surface to ~2 km) and upper (2 to 70 km) partial columns which also allows for the input of external, a priori, temporal information that is shown to improve the information content in the lower partial column fit.

Using measurements from the five North American TCCON sites, we compare our retrieved partial columns of CO and CO_2 DMF to the partial columns calculated from integrated, smoothed in situ data measured by aircraft and AirCore. We report slopes of 1.001 ± 0.003 and 0.999 ± 0.001 for the lower and upper partial column CO_2 comparisons, respectively, and slopes of 0.999 ± 0.002 and 1.081 ± 0.012 for the lower and upper partial column CO comparisons, respectively. The retrieved partial columns have improved direct comparisons and precision compared to the partial columns calculated from the original TCCON spectral windows.

We use the comparison data to calculate validation error multiplier (VEM) values to scale retrieved errors to be representative of the in situ comparisons. The average VEM scaled

errors for the lower partial column CO and CO_2 retrievals are 1.51 ppb (~2%) and 5.09 ppm (~1.25%), respectively. The magnitudes of these error values suggest that the TARDISS retrieval will be useful in its current state for understanding surface fluxes of CO and will have some power for evaluating surface fluxes of CO_2.

The Bayesian TARDISS algorithm enables the informational content of the retrieval to be estimated. The average DoF for the lower partial column retrievals are 8.89 and 27.4 degrees of freedom so that ~9 and ~27 lower partial column values can be retrieved over a day of measurement for CO_2 and CO, respectively. The information content is affected by the parameters of the retrieval so that there is a tradeoff between retrieved error and the DoF of the retrieval. Furthermore, the daily DoF normalized by the number of measurements made in a day could serve as a quality control variable.

Future implementations of the retrieval could use the DoF values to create dynamic VEM to provide error values that are more precise than the static VEM. Similarly, future work could improve the effectiveness of the retrieval of lower partial column CO_2 using the TARDISS algorithm with the input of external information through the a priori covariance matrix, a priori partial column scalar, or the inclusion of the other parameters in the state vector.

Acknowledgements

We thank NASA via 80NSSC22K1066 for support of retrievals from the TCCON stations. A portion of this research was carried out at the Jet Propulsion Laboratory, California Institute of Technology, under a contract with the National Aeronautics and Space Administration (80NM0018D0004). BB is supported by NASA grant 80NSSC18K0898. The authors thank the ObsPack team and data providers for the in situ profile data used for validation. The data were downloaded from https://gml.noaa.gov/ccgg/obspack/data.php?id=obspack_co2_1_GLOBALVIEWplus_v5.0_2019-08-12 and were most recently accessed on September 2nd, 2022. In particular, we thank the NASA LaRC AVOCET and DACOM groups for the KORUS-AQ CO_2 and CO

data, respectively; NASA Goddard for the Picarro CO_2 data at the Armstrong AFB; the SEAC4RS and ATom groups for the CO_2 data; the NOAA Global Monitoring Laboratory for the AirCore CO_2 and CO data, and the long term aircraft CO_2 and CO at the SGP and ETL sites.

Data Availability

The data used in this study are made up of TARDISS retrieval products from five TCCON stations. The retrieval data are publicly available through CaltechDATA (https://doi.org/10.22002/pn9de-cry27) and the data input into the retrieval are publicly available via https://tccondata.org/. Retrieval code is also available through CaltechDATA (https://doi.org/10.22002/dakd7-cdp29).

Author Contributions

HP wrote the TARDISS algorithm following an approach suggested by PW. HP retrieved the data with it and prepared the paper with thorough feedback from the coauthors. JL developed the theoretical framework for the TARDISS algorithm. CR retrieved the TCCON data using GGG for the Lamont, Caltech, and Park Falls sites. GCT gave input on the retrieval algorithm. DW gave input on the validation data and method. LTI and JRP maintain the Armstrong site. KM and BB provided insight and in situ data for the validation. All authors contributed to the review and editing of the work.

Competing Interests

The authors declare they have no conflicts of interest.

References

Andrews, A. E., Kofler, J. D., Trudeau, M. E., Williams, J. C., Neff, D. H., Masarie, K. A., Chao, D. Y., Kitzis, D. R., Novelli, P. C., Zhao, C. L., Dlugokencky, E. J., Lang, P. M., Crotwell, M. J., Fischer, M. L., Parker, M. J., Lee, J. T., Baumann, D. D., Desai, A. R., Stanier, C. O., De Wekker, S. F. J., Wolfe, D. E., Munger, J. W., and Tans, P. P.: CO2, CO, and CH4 measurements from tall towers in the NOAA Earth System Research Laboratory's Global Greenhouse Gas Reference Network: instrumentation, uncertainty

analysis, and recommendations for future high-accuracy greenhouse gas monitoring efforts, Atmos. Meas. Tech., 7, 647–687, https://doi.org/10.5194/amt-7-647-2014, 2014.

Baier, B., Sweeney, C., Newberger, T., Higgs, J., Wolter, S., and NOAA Global Monitoring Laboratory: NOAA AirCore atmospheric sampling system profiles (20210813), https://doi.org/10.15138/6AV0-MY81, 2021a.

Baier, B., Sweeney, C., Newberger, T., Higgs, J., Wolter, S., and NOAA Global Monitoring Laboratory: NOAA AirCore atmospheric sampling system profiles (20210813), https://doi.org/10.15138/6AV0-MY81, 2021b.

Berger, B. W., Davis, K. J., Yi, C., and Bakwin, P. S.: Long-Term Carbon Dioxide Fluxes from a Very Tall Tower in a Northern Forest: Flux Measurement Methodology, JOURNAL OF ATMOSPHERIC AND OCEANIC TECHNOLOGY, 18, 14, 2001.

Buchholz, R., Deeter, M., Worden, H., Gille, J., Edwards, D., Hannigan, J., Jones, N., Paton-Walsh, C., Griffith, D., Smale, D., Robinson, J., Strong, K., Conway, S., Sussmann, R., Hase, F., Blumenstock, T., Mahieu, E., and Langerock, B.: Validation of MOPITT carbon monoxide using ground-based Fourier transform infrared spectrometer data from NDACC, Faculty of Science, Medicine and Health - Papers: part A, 1927–1956, https://doi.org/10.5194/amt-10-1927-2017, 2017.

Connor, B. J., Boesch, H., Toon, G., Sen, B., Miller, C., and Crisp, D.: Orbiting Carbon Observatory: Inverse method and prospective error analysis: OCO INVERSE METHOD, Journal of Geophysical Research: Atmospheres, 113, n/a-n/a, https://doi.org/10.1029/2006JD008336, 2008.

Connor, B. J., Sherlock, V., Toon, G., Wunch, D., and Wennberg, P. O.: GFIT2: an experimental algorithm for vertical profile retrieval from near-IR spectra, Atmospheric Measurement Techniques, 9, 3513–3525, https://doi.org/10.5194/amt-9-3513-2016, 2016.

Cooperative Global Atmospheric Data Integration Project: Multi-laboratory compilation of atmospheric carbon dioxide data for the period 1957-2017; obspack_co2_1_GLOBALVIEWplus_v4.2_2019-03-19, https://doi.org/10.25925/20190319, 2018.

Crawford, J. H., Ahn, J.-Y., Al-Saadi, J., Chang, L., Emmons, L. K., Kim, J., Lee, G., Park, J.-H., Park, R. J., Woo, J. H., Song, C.-K., Hong, J.-H., Hong, Y.-D., Lefer, B. L., Lee, M., Lee, T., Kim, S., Min, K.-E., Yum, S. S., Shin, H. J., Kim, Y.-W., Choi, J.-S., Park, J.-S., Szykman, J. J., Long, R. W., Jordan, C. E., Simpson, I. J., Fried, A., Dibb, J. E., Cho, S., and Kim, Y. P.: The Korea–United States Air Quality (KORUS-AQ) field

study, Elementa: Science of the Anthropocene, 9, 00163, https://doi.org/10.1525/elementa.2020.00163, 2021.

Crosson, E. R.: A cavity ring-down analyzer for measuring atmospheric levels of methane, carbon dioxide, and water vapor, Appl. Phys. B, 92, 403–408, https://doi.org/10.1007/s00340-008-3135-y, 2008.

Deeter, M. N.: Vertical resolution and information content of CO profiles retrieved by MOPITT, Geophys. Res. Lett., 31, L15112, https://doi.org/10.1029/2004GL020235, 2004.

Emmons, L. K., Pfister, G. G., Edwards, D. P., Gille, J. C., Sachse, G., Blake, D., Wofsy, S., Gerbig, C., Matross, D., and Nédélec, P.: Measurements of Pollution in the Troposphere (MOPITT) validation exercises during summer 2004 field campaigns over North America, J. Geophys. Res., 112, D12S02, https://doi.org/10.1029/2006JD007833, 2007.

Hedelius, J. K., Toon, G. C., Buchholz, R. R., Iraci, L. T., Podolske, J. R., Roehl, C. M., Wennberg, P. O., Worden, H. M., and Wunch, D.: Regional and urban column CO trends and anomalies as observed by MOPITT over 16 years, Geophys Res Atmos, https://doi.org/10.1029/2020JD033967, 2021.

Holben, B. N., Eck, T. F., Slutsker, I., Tanré, D., Buis, J. P., Setzer, A., Vermote, E., Reagan, J. A., Kaufman, Y. J., Nakajima, T., Lavenu, F., Jankowiak, I., and Smirnov, A.: AERONET—A Federated Instrument Network and Data Archive for Aerosol Characterization, Remote Sensing of Environment, 66, 1–16, https://doi.org/10.1016/S0034-4257(98)00031-5, 1998.

Iraci, L. T., Podolske, J. R., Roehl, C., Wennberg, P. O., Blavier, J.-F., Allen, N., Wunch, D., and Osterman, G. B.: TCCON data from Edwards (US), Release GGG2020.R0 (R0), https://doi.org/10.14291/TCCON.GGG2020.EDWARDS01.R0, 2022.

Karion, A., Sweeney, C., Tans, P., and Newberger, T.: AirCore: An Innovative Atmospheric Sampling System, Journal of Atmospheric and Oceanic Technology, 27, 1839–1853, https://doi.org/10.1175/2010JTECHA1448.1, 2010.

Keppel-Aleks, G., Wennberg, P. O., and Schneider, T.: Sources of variations in total column carbon dioxide, Atmos. Chem. Phys., 11, 3581–3593, https://doi.org/10.5194/acp-11-3581-2011, 2011.

Keppel-Aleks, G., Wennberg, P. O., Washenfelder, R. A., Wunch, D., Schneider, T., Toon, G. C., Andres, R. J., Blavier, J.-F., Connor, B., Davis, K. J., Desai, A. R., Messerschmidt, J., Notholt, J., Roehl, C. M., Sherlock, V., Stephens, B. B., Vay, S. A., and Wofsy, S. C.: The imprint of surface fluxes and transport on variations in total

column carbon dioxide, Biogeosciences, 9, 875–891, https://doi.org/10.5194/bg-9-875-2012, 2012.

Kerzenmacher, T., Dils, B., Kumps, N., Blumenstock, T., Clerbaux, C., Coheur, P.-F., Demoulin, P., García, O., George, M., Griffith, D. W. T., Hase, F., Hadji-Lazaro, J., Hurtmans, D., Jones, N., Mahieu, E., Notholt, J., Paton-Walsh, C., Raffalski, U., Ridder, T., Schneider, M., Servais, C., and De Mazière, M.: Validation of IASI FORLI carbon monoxide retrievals using FTIR data from NDACC, Atmospheric Measurement Techniques, 5, 2751–2761, https://doi.org/10.5194/amt-5-2751-2012, 2012.

Kuai, L., Wunch, D., Shia, R.-L., Connor, B., Miller, C., and Yung, Y.: Vertically constrained CO2 retrievals from TCCON measurements, Journal of Quantitative Spectroscopy and Radiative Transfer, 113, 1753–1761, https://doi.org/10.1016/j.jqsrt.2012.04.024, 2012.

Masarie, K. A., Peters, W., Jacobson, A. R., and Tans, P. P.: ObsPack: a framework for the preparation, delivery, and attribution of atmospheric greenhouse gas measurements, Earth Syst. Sci. Data, 6, 375–384, https://doi.org/10.5194/essd-6-375-2014, 2014.

Olsen, S. C.: Differences between surface and column atmospheric CO 2 and implications for carbon cycle research, J. Geophys. Res., 109, D02301, https://doi.org/10.1029/2003JD003968, 2004.

Parrish, D. D., Xu, J., Croes, B., and Shao, M.: Air quality improvement in Los Angeles—perspectives for developing cities, Frontiers of Environmental Science & Engineering, 10, 1–13, https://doi.org/10.1007/s11783-016-0859-5, 2016.

Pougatchev, N. S., Connor, B. J., and Rinsland, C. P.: Infrared measurements of the ozone vertical distribution above Kitt Peak, J. Geophys. Res., 100, 16689, https://doi.org/10.1029/95JD01296, 1995.

Roche, S., Strong, K., Wunch, D., Mendonca, J., Sweeney, C., Baier, B., Biraud, S. C., Laughner, J. L., Toon, G. C., and Connor, B. J.: Retrieval of atmospheric CO2 vertical profiles from ground-based near-infrared spectra, Atmos. Meas. Tech., 14, 3087–3118, https://doi.org/10.5194/amt-14-3087-2021, 2021.

Rodgers, C. D.: Inverse methods for atmospheric sounding: theory and practice, Repr., World Scientific, Singapore, 240 pp., 2008.

Rodgers, C. D. and Connor, B. J.: Intercomparison of remote sounding instruments, Journal of Geophysical Research: Atmospheres, 108, n/a-n/a, https://doi.org/10.1029/2002JD002299, 2003.

Shan, C., Wang, W., Liu, C., Guo, Y., Xie, Y., Sun, Y., Hu, Q., Zhang, H., Yin, H., and Jones, N.: Retrieval of vertical profiles and tropospheric CO2 columns based on high-resolution FTIR over Hefei, China, Opt. Express, 29, 4958, https://doi.org/10.1364/OE.411383, 2021.

Sweeney, C., Karion, A., Wolter, S., Newberger, T., Guenther, D., Higgs, J. A., Andrews, A. E., Lang, P. M., Neff, D., Dlugokencky, E., Miller, J. B., Montzka, S. A., Miller, B. R., Masarie, K. A., Biraud, S. C., Novelli, P. C., Crotwell, M., Crotwell, A. M., Thoning, K., and Tans, P. P.: Seasonal climatology of CO2 across North America from aircraft measurements in the NOAA/ESRL Global Greenhouse Gas Reference Network, Journal of Geophysical Research, 36, https://doi.org/10.1002/2014JD022591, 2015.

Tans, P.: System and method for providing vertical profile measurements of atmospheric gases, , 15, 2009.

Tans, P.: Fill dynamics and sample mixing in the AirCore, Atmos. Meas. Tech., 15, 1903–1916, https://doi.org/10.5194/amt-15-1903-2022, 2022.

Thompson, C. R., Wofsy, S. C., Prather, M. J., Newman, P. A., Hanisco, T. F., Ryerson, T. B., Fahey, D. W., Apel, E. C., Brock, C. A., Brune, W. H., Froyd, K., Katich, J. M., Nicely, J. M., Peischl, J., Ray, E., Veres, P. R., Wang, S., Allen, H. M., Asher, E., Bian, H., Blake, D., Bourgeois, I., Budney, J., Bui, T. P., Butler, A., Campuzano-Jost, P., Chang, C., Chin, M., Commane, R., Correa, G., Crounse, J. D., Daube, B., Dibb, J. E., DiGangi, J. P., Diskin, G. S., Dollner, M., Elkins, J. W., Fiore, A. M., Flynn, C. M., Guo, H., Hall, S. R., Hannun, R. A., Hills, A., Hintsa, E. J., Hodzic, A., Hornbrook, R. S., Huey, L. G., Jimenez, J. L., Keeling, R. F., Kim, M. J., Kupc, A., Lacey, F., Lait, L. R., Lamarque, J.-F., Liu, J., McKain, K., Meinardi, S., Miller, D. O., Montzka, S. A., Moore, F. L., Morgan, E. J., Murphy, D. M., Murray, L. T., Nault, B. A., Neuman, J. A., Nguyen, L., Gonzalez, Y., Rollins, A., Rosenlof, K., Sargent, M., Schill, G., Schwarz, J. P., Clair, J. M. St., Steenrod, S. D., Stephens, B. B., Strahan, S. E., Strode, S. A., Sweeney, C., Thames, A. B., Ullmann, K., Wagner, N., Weber, R., Weinzierl, B., Wennberg, P. O., Williamson, C. J., Wolfe, G. M., and Zeng, L.: The NASA Atmospheric Tomography (ATom) Mission: Imaging the Chemistry of the Global Atmosphere, Bulletin of the American Meteorological Society, 103, E761–E790, https://doi.org/10.1175/BAMS-D-20-0315.1, 2022.

Toon, O. B., Maring, H., Dibb, J., Ferrare, R., Jacob, D. J., Jensen, E. J., Luo, Z. J., Mace, G. G., Pan, L. L., Pfister, L., Rosenlof, K. H., Redemann, J., Reid, J. S., Singh, H. B., Thompson, A. M., Yokelson, R., Minnis, P., Chen, G., Jucks, K. W., and Pszenny, A.: Planning, implementation, and scientific goals of the Studies of Emissions and Atmospheric Composition, Clouds and Climate Coupling by Regional Surveys (SEAC4RS) field mission, J. Geophys. Res. Atmos., 121, 4967–5009, https://doi.org/10.1002/2015JD024297, 2016.

Van Rooy, P., Tasnia, A., Barletta, B., Buenconsejo, R., Crounse, J. D., Kenseth, C., Meinardi, S., Murphy, S., Parker, H., Schulze, B., Seinfeld, J. H., Wennberg, P. O., Blake, D. R., and Barsanti, K. C.: Observations of Volatile Organic Compounds in the Los Angeles Basin during COVID-19, ACS Earth Space Chem., acsearthspacechem.1c00248, https://doi.org/10.1021/acsearthspacechem.1c00248, 2021.

Wennberg, P. O., Roehl, C.M., Wunch, D, Blavier, J.-F., Toon, G. C., Allen, N. T., Treffers, R., and Laughner, J.: TCCON data from Caltech (US), Release GGG2020.R0 (R0), https://doi.org/10.14291/TCCON.GGG2020.PASADENA01.R0, 2022a.

Wennberg, P. O., Wunch, D., Roehl, C. M., Blavier, J.-F., Toon, G. C., and Allen, N. T.: TCCON data from Lamont (US), Release GGG2020.R0 (R0), https://doi.org/10.14291/TCCON.GGG2020.LAMONT01.R0, 2022b.

Wennberg, P. O., Roehl, C. M., Wunch, D., Toon, G. C., Blavier, J.-F., Washenfelder, R., Keppel-Aleks, G., and Allen, N. T.: TCCON data from Park Falls (US), Release GGG2020.R0 (R0), https://doi.org/10.14291/TCCON.GGG2020.PARKFALLS01.R0, 2022c.

Wiacek, A., Taylor, J. R., Strong, K., Saari, R., Kerzenmacher, T. E., Jones, N. B., and Griffith, D. W. T.: Ground-Based Solar Absorption FTIR Spectroscopy: Characterization of Retrievals and First Results from a Novel Optical Design Instrument at a New NDACC Complementary Station, J. Atmos. Oceanic Technol., 24, 432–448, https://doi.org/10.1175/JTECH1962.1, 2007.

Wofsy, S. C., Afshar, S., Allen, H. M., Apel, E. C., Asher, E. C., Barletta, B., Bent, J., Bian, H., Biggs, B. C., Blake, D. R., Blake, N., Bourgeois, I., Brock, C. A., Brune, W. H., Budney, J. W., Bui, T. P., Butler, A., Campuzano-Jost, P., Chang, C. S., Chin, M., Commane, R., Correa, G., Crounse, J. D., Cullis, P. D., Daube, B. C., Day, D. A., Dean-Day, J. M., Dibb, J. E., DiGangi, J. P., Diskin, G. S., Dollner, M., Elkins, J. W., Erdesz, F., Fiore, A. M., Flynn, C. M., Froyd, K. D., Gesler, D. W., Hall, S. R., Hanisco, T. F., Hannun, R. A., Hills, A. J., Hintsa, E. J., Hoffman, A., Hornbrook, R. S., Huey, L. G., Hughes, S., Jimenez, J. L., Johnson, B. J., Katich, J. M., Keeling, R. F., Kim, M. J., Kupc, A., Lait, L. R., McKain, K., Mclaughlin, R. J., Meinardi, S., Miller, D. O., Montzka, S. A., Moore, F. L., Morgan, E. J., Murphy, D. M., Murray, L. T., Nault, B. A., Neuman, J. A., Newman, P. A., Nicely, J. M., Pan, X., Paplawsky, W., Peischl, J., Prather, M. J., Price, D. J., Ray, E. A., Reeves, J. M., Richardson, M., Rollins, A. W., Rosenlof, K. H., Ryerson, T. B., Scheuer, E., Schill, G. P., Schroder, J. C., Schwarz, J. P., St.Clair, J. M., Steenrod, S. D., Stephens, B. B., Strode, S. A., Sweeney, C., Tanner, D., Teng, A. P., Thames, A. B., Thompson, C. R., Ullmann, K., Veres, P. R., Wagner, N. L., Watt, A., Weber, R., Weinzierl, B. B., Wennberg, P. O., Williamson, C. J., Wilson, J. C., et al.: ATom: Merged Atmospheric Chemistry, Trace Gases, and Aerosols, Version 2, https://doi.org/10.3334/ORNLDAAC/1925, 2021.

Wolfe, G. M., Kawa, S. R., Hanisco, T. F., Hannun, R. A., Newman, P. A., Swanson, A., Bailey, S., Barrick, J., Thornhill, K. L., Diskin, G., DiGangi, J., Nowak, J. B., Sorenson, C., Bland, G., Yungel, J. K., and Swenson, C. A.: The NASA Carbon Airborne Flux Experiment (CARAFE): instrumentation and methodology, Atmos. Meas. Tech., 11, 1757–1776, https://doi.org/10.5194/amt-11-1757-2018, 2018.

Wunch, D., Toon, G. C., Wennberg, P. O., Wofsy, S. C., Stephens, B. B., Fischer, M. L., Uchino, O., Abshire, J. B., Bernath, P., Biraud, S. C., Blavier, J.-F. L., Boone, C., Bowman, K. P., Browell, E. V., Campos, T., Connor, B. J., Daube, B. C., Deutscher, N. M., Diao, M., Elkins, J. W., Gerbig, C., Gottlieb, E., Griffith, D. W. T., Hurst, D. F., Jiménez, R., Keppel-Aleks, G., Kort, E. A., Macatangay, R., Machida, T., Matsueda, H., Moore, F., Morino, I., Park, S., Robinson, J., Roehl, C. M., Sawa, Y., Sherlock, V., Sweeney, C., Tanaka, T., and Zondlo, M. A.: Calibration of the Total Carbon Column Observing Network using aircraft profile data, Atmospheric Measurement Techniques, 3, 1351–1362, https://doi.org/10.5194/amt-3-1351-2010, 2010.

Wunch, D., Toon, G. C., Blavier, J.-F. L., Washenfelder, R. A., Notholt, J., Connor, B. J., Griffith, D. W. T., Sherlock, V., and Wennberg, P. O.: The Total Carbon Column Observing Network, Philosophical Transactions of the Royal Society A: Mathematical, Physical and Engineering Sciences, 369, 2087–2112, https://doi.org/10.1098/rsta.2010.0240, 2011.

Xu, K., Pingintha-Durden, N., Luo, H., Durden, D., Sturtevant, C., Desai, A. R., Florian, C., and Metzger, S.: The eddy-covariance storage term in air: Consistent community resources improve flux measurement reliability, Agricultural and Forest Meteorology, 279, 107734, https://doi.org/10.1016/j.agrformet.2019.107734, 2019.

Zhou, M., Langerock, B., Vigouroux, C., Sha, M. K., Ramonet, M., Delmotte, M., Mahieu, E., Bader, W., Hermans, C., Kumps, N., Metzger, J.-M., Duflot, V., Wang, Z., Palm, M., and De Mazière, M.: Atmospheric CO and CH4 time series and seasonal variations on Reunion Island from ground-based in situ and FTIR (NDACC and TCCON) measurements, Atmos. Chem. Phys., 18, 13881–13901, https://doi.org/10.5194/acp-18-13881-2018, 2018.

Zhou, M., Langerock, B., Vigouroux, C., Sha, M. K., Hermans, C., Metzger, J.-M., Chen, H., Ramonet, M., Kivi, R., Heikkinen, P., Smale, D., Pollard, D. F., Jones, N., Velazco, V. A., García, O. E., Schneider, M., Palm, M., Warneke, T., and De Mazière, M.: TCCON and NDACC XCO measurements: difference, discussion and application, Atmos. Meas. Tech., 12, 5979–5995, https://doi.org/10.5194/amt-12-5979-2019, 2019.

Chapter 4

ASSESSING SURFACE FLUXES OF CARBON DIOXIDE USING A NOVEL REMOTE-SENSING DATASET

Abstract.

We describe the use of novel Temporal Atmospheric Retrieval Determining Information from Secondary Scaling (TARDISS) retrieved lower partial column CO_2 (0-2km), $\langle CO_2 \rangle_{LPC}$, to estimate surface fluxes at Park Falls, WI. We compare these estimates with surface flux estimates obtained from in situ observations made on the WLEF tall tower by the Chequamegon Ecosystem-Atmosphere Study (ChEAS). We show that the TARDISS upper (free troposphere / stratosphere) CO_2 partial columns are well correlated with free troposphere meteorological tracers while showing little correlation with the diurnally varying fluxes in the lower partial column. Monthly aggregated Net Ecosystem Exchange (NEE) calculated from the diurnal variation in $\langle CO_2 \rangle_{LPC}$ compare well to NEE values estimated at Park Falls from in situ observations with a fit slope of 1.05 ± 0.11 and an offset of -3.3 ± 0.6 μmol m-2 s-1. The $\langle CO_2 \rangle_{LPC}$ has high day-to-day variance similar in magnitude to the variation in the total column CO_2 suggesting common influences on both total and partial column fluxes. Likewise, we find that surface fluxes calculated from $\langle CO_2 \rangle_{LPC}$ in the Mojave Desert have large enough day-to-day variations to suggest that temporally aggregating $\langle CO_2 \rangle_{LPC}$ derived NEE fluxes is beneficial regardless of site location. Future $\langle CO_2 \rangle_{LPC}$ retrievals can incorporate in situ information to better constrain the calculations of surface fluxes.

4.1 Introduction

Accurate knowledge of atmospheric carbon fluxes is required to predict future climate, to inform climate policy, and to understand anthropogenic influences on climate and the biosphere. Carbon fluxes are estimated from total column CO_2 dry mole fractions (DMF),

denoted as $<CO_2>_{TC}$, from space and ground-based measurements with varying degrees of success depending on location and the available observation density (Basu et al., 2018; Keppel-Aleks et al., 2012; Torres et al., 2019; Feldman et al., 2023; Schwandner et al., 2017; Wu et al., 2020b; Wunch et al., 2013). For example, column measurements from the North American boreal forest deal with issues of retrieval errors and seasonally varying sensitivities that can obscure the surface fluxes and lead to unrepresentative flux calculations (Byrne et al., 2017; Mitchell et al., 2023). As these remote measurements use model derived a priori values that include influences of surface sources and sinks of carbon informed from remote measurements, comparisons with local, in situ measurements of surface fluxes are crucial to ensure accurate representation of fluxes across different scales of analysis.

TCCON $<CO_2>_{TC}$ measurements have been used to estimate surface fluxes but still face issues from influences of non-local sources. Even in heavily forested regions, transport by synoptic weather systems generates variations in $<CO_2>_{TC}$ that are the same magnitude or larger than those produced by more local biosphere-driven surface fluxes. The influence of the large-scale gradients can be partially mitigated against with use of meteorological tracers that are used to determine the latitudinal origin of an air mass. Furthermore, intraday variability of $<CO_2>_{TC}$ driven by small-scale weather activity can also have a significant effect on calculated fluxes that is not directly correlated to the meteorological tracers (Keppel-Aleks et al., 2011, 2012; Torres et al., 2019). The imprint of the large and small gradients, primarily in the free troposphere of the total column, limits the effectiveness of the subsequently calculated fluxes.

In this study, we use lower partial column CO_2 data retrieved by the TARDISS algorithm (Parker et al., 2022) applied to TCCON total column data to calculate surface carbon fluxes and compare these to fluxes derived from in situ data obtained from the WLEF tall tower site in Park Falls, WI (Berger et al., 2001; Desai et al., 2015). Since the partial column data represent the mean CO2 dry volume mixing ratio between 1) the surface and 2 km and 2) between 2 km and the top of the atmosphere, the effects of free tropospheric variations in

CO_2 should be more isolated from the variations in the lower partial column. We compare the fluxes calculated from the lower partial column data to various reported fluxes from different vertical positions on the tower to further understand what influences the partial column fluxes and what biases may exist. We also use fluxes calculated from another TCCON site in the Mojave Desert, where biogenic surface fluxes are minimal, to understand the limitations of the method.

4.2 Methodology and Data

4.2.1 TARDISS Lower Partial Column Data

We use lower partial column CO_2 DMF data, denoted as $<CO_2>_{LPC}$, retrieved using the TARDISS algorithm from TCCON $<CO_2>_{TC}$ observations (Wunch et al., 2011) made at TCCON sites located in Park Falls, WI and at the NASA Armstrong, Edwards Air Force Base in California. The TARDISS algorithm uses the differences in the quality controlled, World Meteorological Organization (WMO) calibrated TCCON total column DMF values retrieved from spectral windows with differing vertical sensitivities to infer the $<CO_2>_{LPC}$ values. The $<CO_2>_{LPC}$ values are the average DMF of CO_2 for the column of the atmosphere from the surface to 2 km altitude (~800 hPa) with errors that are scaled on a site-by-site basis from validation comparisons to in situ profile measurements. For hours with a minimum of 20 min of observations, we bin the measurements to produce hourly averages of $<CO_2>_{LPC}$. This filtering retains 62% to 84% of the data for the Park Falls and Armstrong site, respectively.

Since the partial columns are split at 2 km altitude, the $<CO_2>_{LPC}$ values are more isolated from the CO_2 variations in the free troposphere and are more strongly influenced by surface CO_2 fluxes. $<CO_2>_{TC}$ values are significantly influenced by synoptic scale changes due to advection of air masses across latitudinal CO_2 gradients (Keppel-Aleks et al., 2011, 2012; Torres et al., 2019; Geels et al., 2004). These temporal gradients are strongly tied to the advection of free tropospheric gradients and are diagnosed by changes in the potential temperature (θ). θ is a good dynamical tracer of the latitudinal origin of measured air

masses and the influence of these advective fluxes on changes in the total column values (Keppel-Aleks et al., 2011, 2012). Figure 4.1 shows the free tropospheric potential temperature and the upper and lower partial column DMF values ($<CO_2>_{UPC}$, $<CO_2>_{LPC}$) that have been detrended by subtracting a thirty-day running mean. The partial column data allows us to separate some of the influences of variation in the free troposphere and above from those at the surface particularly during the growing season (June through August) as shown by the comparisons in Fig. C.1-C.3.

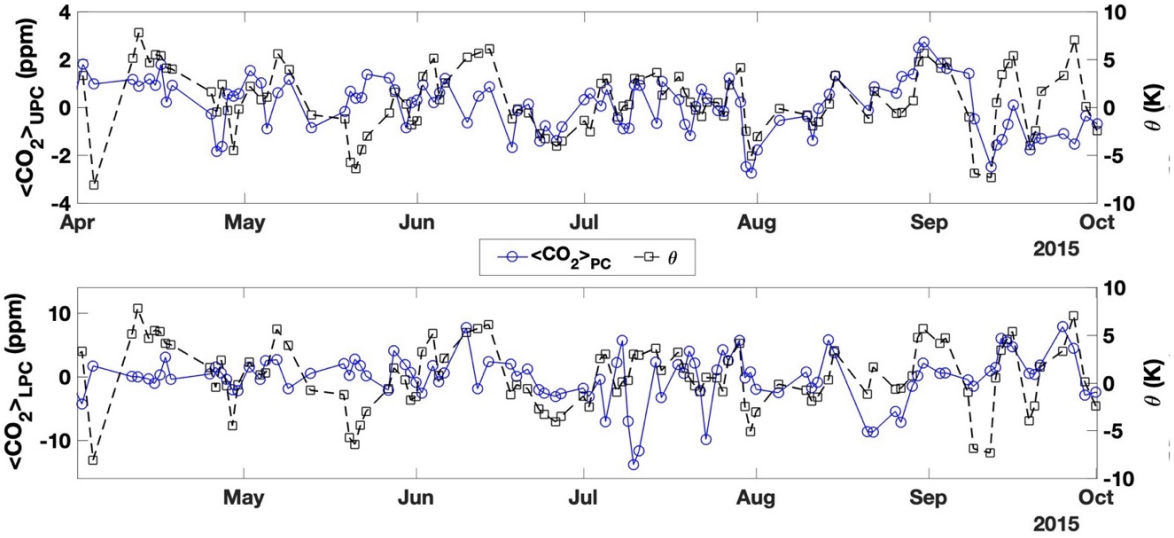

Figure 4.1: Selected time series of daily average TARDISS upper (top panel) and lower (bottom panel) partial column CO_2 (left axis, blue circles) and the free tropospheric temperature (right axis, black squares) at the Park Falls, WI, TCCON detrended using a 30-day moving mean.

4.2.2 Estimating Net Ecosystem Exchange from Lower Partial Column Data

We use the method outlined in Keppel-Aleks et al., 2012 altered for partial columns to estimate the net flux of CO_2 (in Park Falls, this is dominated by ecosystem exchange (NEE)). We define the mass of the partial column of a gas as the DMF of that gas multiplied by the dry mass of the atmosphere in the partial column:

$$C_G = \langle G \rangle_{LPC} \cdot C_{air} \approx \langle G \rangle_{LPC} \cdot \frac{P_{s,LPC} - P_{q,LPC}}{g \cdot M_{air}}, \quad (4.1)$$

where $\langle G \rangle_{LPC}$ is the lower partial column DMF of the species of interest, C_{air} is the lower partial column of dry air, g is the gravitational constant, and M_{air} is the molecular mass of dry air. $Ps_{,LPC}$ is the pressure contribution of the lower partial column calculated as:

$$P_{s,LPC} = P_s \cdot \frac{\langle O_2 \rangle_{LPC}}{\langle O_2 \rangle_{TC}}, \tag{4.2}$$

where P_s is the surface pressure measured at the TCCON station which is multiplied by the ratio of the lower partial column O_2 to the total partial column O_2 retrieved from the TCCON measurements. Since the proportion of O_2 should be independent of altitude, this ratio provides a reasonable ratio of the mass relating to the lower partial column.

$P_{q,LPC}$ is the pressure contribution of the lower partial column water values calculated as:

$$P_{q,LPC} = \langle H_2O \rangle_{LPC} \cdot \frac{P_{s,LPC}}{AK_{H_2O,LPC}}, \tag{4.3}$$

where $\langle H_2O \rangle_{LPC}$ is the lower partial column DMF of water retrieved from TCCON and $AK_{H2O,LPC}$ is the mean value of the averaging kernel for the lower partial column of the water retrieval. We divide by the averaging kernel since the lower partial column water values are calculated from the total column values, not rescaled by the TARDISS algorithm, and the total column retrieval has different sensitivities to different parts of the atmosphere. The TARDISS retrieved lower partial column values are assumed to have averaging kernel values of one for this application. We differentiate Eq. (4.1) to get the change in the lower partial column mass of CO_2 over the day. Assuming this change is due to uptake and release of carbon from the biosphere, it is equivalent to NEE:

$$Flux_{FTS} = \frac{\partial C_{CO_2}}{\partial t} = \frac{\Delta \langle CO_2 \rangle_{LPC}}{\Delta t} \cdot \frac{P_{s,LPC} - P_{q,LPC}}{g \cdot M_{air}}. \tag{4.4}$$

We calculate $\Delta\langle CO_2\rangle_{LPC}$ as the difference between the averages before and after solar noon (roughly 1pm local) and C_{air} is the daily average partial column mass. We propagate the errors from the $\langle CO_2\rangle_{LPC}$ and the hourly, daily, and monthly averages as necessary to calculate the errors for the $Flux_{FTS}$ calculations, also referred to as TARDISS fluxes going forward. We filter out measurement days where the degrees of freedom of signal per measurement for the TARDISS retrieval are below 0.02 and 0.06 for the lower partial column and upper partial column retrievals, respectively. We also filter out measurement days that have less than three hours of measurement in either the morning or afternoon. Finally, we require that measurement days have a similar number (no more than two hours difference) of measurements in the morning and afternoon and that monthly aggregations have more than three days of data. These filters leave ~37% of the measurement days for comparison.

4.2.3 Tall Tower Net Ecosystem Exchange

We compare our calculations to coincident hourly flux estimates obtained from in situ observations made from the WLEF tall tower (447 m) in Park Falls, WI (Desai et al., 2015). At multiple altitudes on the tower, the concentrations and eddy covariation fluxes of CO_2 and water are obtained using infrared gas analyzers (Li-COR Inc., Lincoln, Nebraska model Li-6262 and Li-7000) and wind speed and temperature measured using a sonic anemometer (Applied Technologies Inc., Boulder, Colorado, model K).

The Park Falls installation is a component of the Chequamegon Ecosystem-Atmosphere Study (ChEAS) research cooperative and Ameriflux network (Ankur Desai, 2023; Novick et al., 2018). The fluxes are calculated from the sum of the storage fluxes and eddy covariance fluxes reported at 30m, 120m, and 396m levels on the tower (Desai et al., 2015; Site Info for US-PFa, 2023). Storage fluxes are calculated as the integrated change in time of the interpolated vertical profile of tower CO_2 measurements and accounts for the change in carbon below the eddy covariance measurement level on the tower. Eddy covariance fluxes are calculated from the covariant fluctuations of CO_2 measurements and

measurements of vertical wind speeds. With meteorological conditions that are sufficiently turbulent, the eddy covariance fluxes measure the instantaneous vertical carbon fluxes. The full details of the calculations and discussions of the regional representation of the tower flux measurements are found in other work (Berger et al., 2001; Chu et al., 2021; Desai et al., 2015; Novick et al., 2018; Papale et al., 2006; Xu et al., 2019). For these calculations, influences of horizontal advection on the fluxes are assumed to be zero over daily or longer time scales (Xu et al., 2019; Yi et al., 2000) and the 'preferred' NEE values are calculated using an algorithm developed by Davis et al., 2003 that uses measurements of turbulence and atmospheric conditions to determine the contributions from the available measurement levels on the tower. We compare our calculated fluxes to the daily averages of the 'preferred', quality controlled, gap-filled, spatially-aggregated NEE values. We also compare our estimates with the individual storage eddy covariance, and NEE fluxes at different levels of the tower.

We use coincident hourly measurements between the tower and TARDISS measurements from the Park Falls site between 2011 and 2020. For discussions involving the Armstrong site, we use TARDISS measurements between 2013 and 2021.

4.3 Results and Discussion

4.3.1 Comparing Surface Fluxes Derived from In Situ and Partial Column Data

The diurnal changes in the TARDISS lower partial column behave similarly to those seen in the total column calculations described in Keppel-Aleks et al., 2012. Our comparison of $Flux_{FTS}$ estimated from the change in the $<CO_2>_{LPC}$ with the daily average tower NEE derived from the in situ data has high variance which decreases with monthly aggregation. As discussed in Keppel-Aleks et al., 2012, influences from intraday mesoscale variability in the free tropospheric CO_2 impact surface exchange estimates for individual days but tend to average away at monthly averages. For the TARDISS data, the variance in the $<CO_2>_{LPC}$ driven by transport may be muted but nevertheless adds noise to the estimate of the decrease in CO_2 driven by surface exchange, particularly during colder months (November

– April) when changes in $\langle CO_2 \rangle_{LPC}$ are correlated with changes in θ (Fig. C.2). Influences on the flux calculations from variation of CO_2 in the free troposphere as described by Keppel-Aleks et al., 2012 should theoretically be reduced in the partial columns so that the change in the free tropospheric CO_2 concentrations do not influence flux calculations made with lower partial column data. These influences also exist independently in the lower partial column, however, errors from the upper partial column could also affect the lower partial column due to a small, but non-zero, covariance between the upper and lower partial columns. There also likely exist errors in the prior profile shape used in the TCCON, and therefore TARDISS retrievals, between the surface and 2 km height that could also contribute to day-to-day variation in compared flux values.

On a monthly aggregated scale, the TARDISS Flux calculations compare well with the tower NEE values as shown in Fig. 4.2. The in situ estimated NEE explains more than half of the variation in the estimated $\langle CO_2 \rangle_{LPC}$ variations calculated in the TARDISS data with a correlation coefficient of 0.61 using data from all seasons. While the NEE estimated from the total column data are larger than the NEE calculated from the in situ data (slope = 1.5 ± 0.2 and bias of -4.3 ± 0.7 μmol m^{-2} s^{-1}), fluxes estimated from the TARDISS data are more similar and have a smaller root mean square (slope = 1.05 ± 0.11 and bias of -3.3 ± 0.6 μmol m^{-2} s^{-1}). This comparison suggests that $\langle CO_2 \rangle_{LPC}$ is more effective than the total column at capturing the signals of surface carbon fluxes. The bias in the comparison between the TARDISS flux and that estimated from the total column changes is similar, suggesting a common source of error in either the in situ or FTS estimates of the surface exchange.

The differences between the TARDISS fluxes and in situ NEE estimates may reflect a larger horizontal footprint for the FTS data than the in situ data (Belikov et al., 2017; Chu et al., 2021; Kljun et al., 2015). The related influence of advection in the mixed layer is assumed to be negligible in the in situ measurements (Xu et al., 2019; Yi et al., 2000) which may lead to an overall offset in the calculations from the remotely-sensed values. Nevertheless, we find that the daily and monthly differences are not significantly

correlated with wind speed, wind direction, temperature, daily temperature change, atmospheric friction, or other meteorological measurements made by the tower or at the TCCON site.

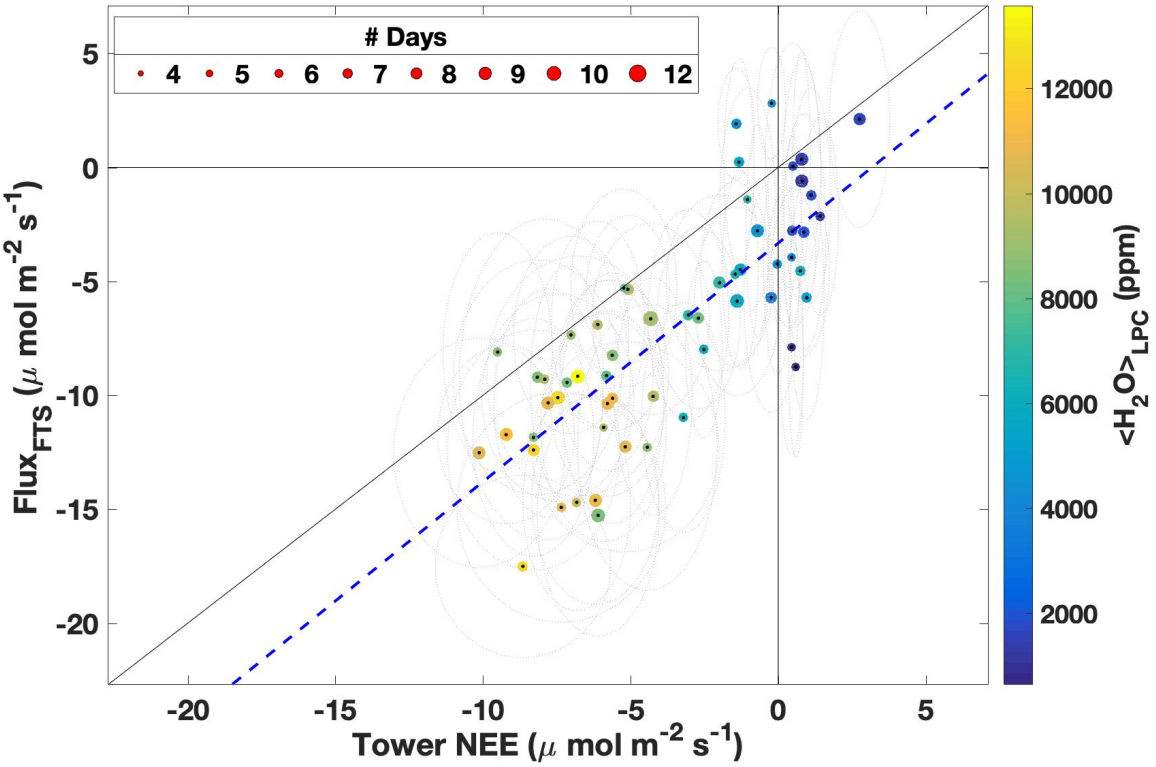

Figure 4.2: Monthly aggregated estimates of $Flux_{FTS}$ and the NEE calculated from in situ measurements (Tower NEE) color-coded by the lower partial column water column and sized by the number of days measured in each month. The blue dashed line represents the linear fit between the two measurements of NEE. The grey ellipses represent the errors in the x- and y-direction to one standard deviation. The solid diagonal black line is the 1-1 comparison line, and the solid vertical and horizontal lines are at the values of zero for the tower and FTS NEE, respectively.

4.3.2 Comparing with Components of the NEE Fluxes derived from the In Situ Data

We also compare the NEE estimated from the TARDISS data to the storage, eddy covariance, and total NEE fluxes at each level of the tower. The 'preferred' NEE values at a tower site are calculated using an algorithm that uses measurements of atmospheric conditions to determine the tower level that is most representative of the fluxes (Davis et

al., 2003). In Fig. 4.2, we use the preferred NEE values for the overall flux comparisons, but here we study the component fluxes of NEE derived from the in situ data. The TARDISS fluxes are most tightly correlated with the storage fluxes (the diurnally estimated change in the CO_2 below the top level of the tower). Regardless of which level of the tower they were measured at, the correlation between the TARDISS fluxes and the eddy covariance fluxes is quite weak.

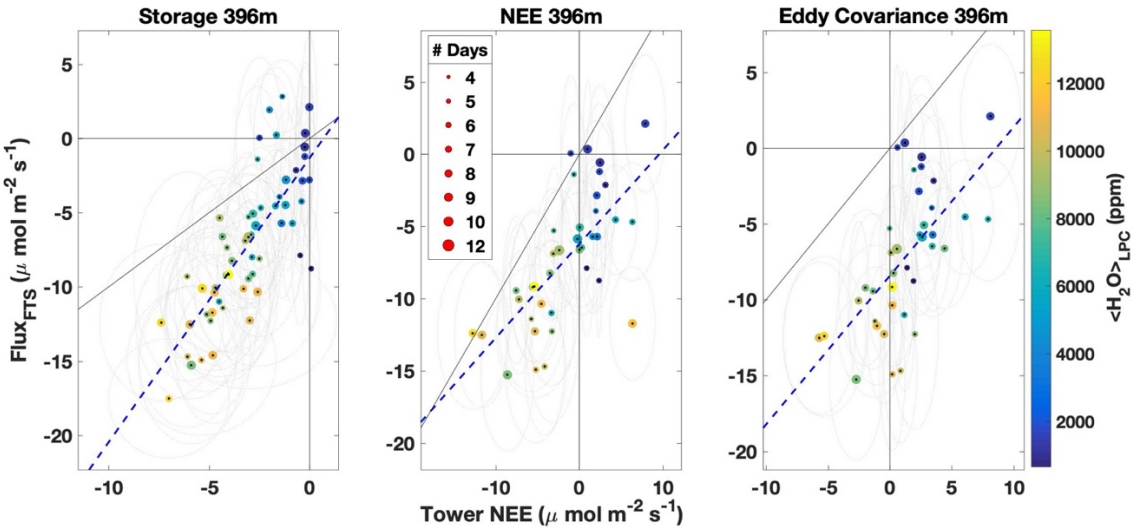

Figure 4.3: Direct comparison of the monthly aggregations of the TARDISS derived $Flux_{FTS}$ and the storage fluxes (left panel), eddy covariance fluxes (right panel), and total NEE fluxes (middle panel) reported from the 396m level of the tall tower color-coded by the lower partial column water column and sized by the number of days measured in each month. The blue dashed lines represent the linear fit between the data. The grey ellipses represent the errors in the x- and y-direction to one standard deviation. The solid diagonal black line is the 1-1 comparison line, and the solid vertical and horizontal lines are at the values of zero for the tower and FTS fluxes, respectively.

The strong correlation between the storage fluxes, which represent the changes in the amount of CO_2 below the height of the tower, and the TARDISS estimated NEE likely reflects the similarity in the observational approach. Likewise, comparisons of TARDISS fluxes with tower storage fluxes consistently have a smaller offset and a larger fit slope than comparisons to eddy covariance fluxes as shown in Fig. 4.3, Fig. C.4-C.5, and Table C.1. The storage fluxes estimated at the 396 m level are expected to measure carbon fluxes

from a portion of the atmospheric boundary layer. The slope of 1.9 ± 0.20 between the tower-derived and TARDISS-derived fluxes suggests that the change in the CO_2 below 396 m accounts for about 50% of the total decrease in CO_2 in the lower column — a reasonable fraction given the mean height of the mixed layer during the day.

The eddy covariance fluxes represent the instantaneous fluxes of CO_2 at the measurement level of the tower given an effectively turbulent atmosphere and large enough eddies. Since the canopy level is generally near the lowest level of measurement on the tower, the eddy covariance fluxes measure the instantaneous vertical carbon fluxes through the level but to estimate the total flux at the surface, an additional term representing the change in the amount of CO_2 in the atmosphere below the tower (the storage flux) is required. The TARDISS estimated total change in CO_2 in the lower atmosphere are somewhat uncorrelated with the eddy covariance fluxes from the 396m level (Fig. 4.3). The nominal slope of the fit is 0.98 ± 0.20 but with a large offset (-8.41 ± 0.63 μmol m^{-2} s^{-1}). The TARDISS data have similar correlation (or lack thereof) for the in situ estimates of flux type at all vertical measurement levels on the tower (Fig. C.4-C.5 and Table C.1). As the NEE fluxes are the sum of the storage and eddy covariance fluxes, the comparison with the TARDISS fluxes have comparable statistics which reinforces our choice to use the gap-filled, quality-controlled NEE flux measurements for comparison.

4.3.3 Investigating Fluxes from Another TCCON Site

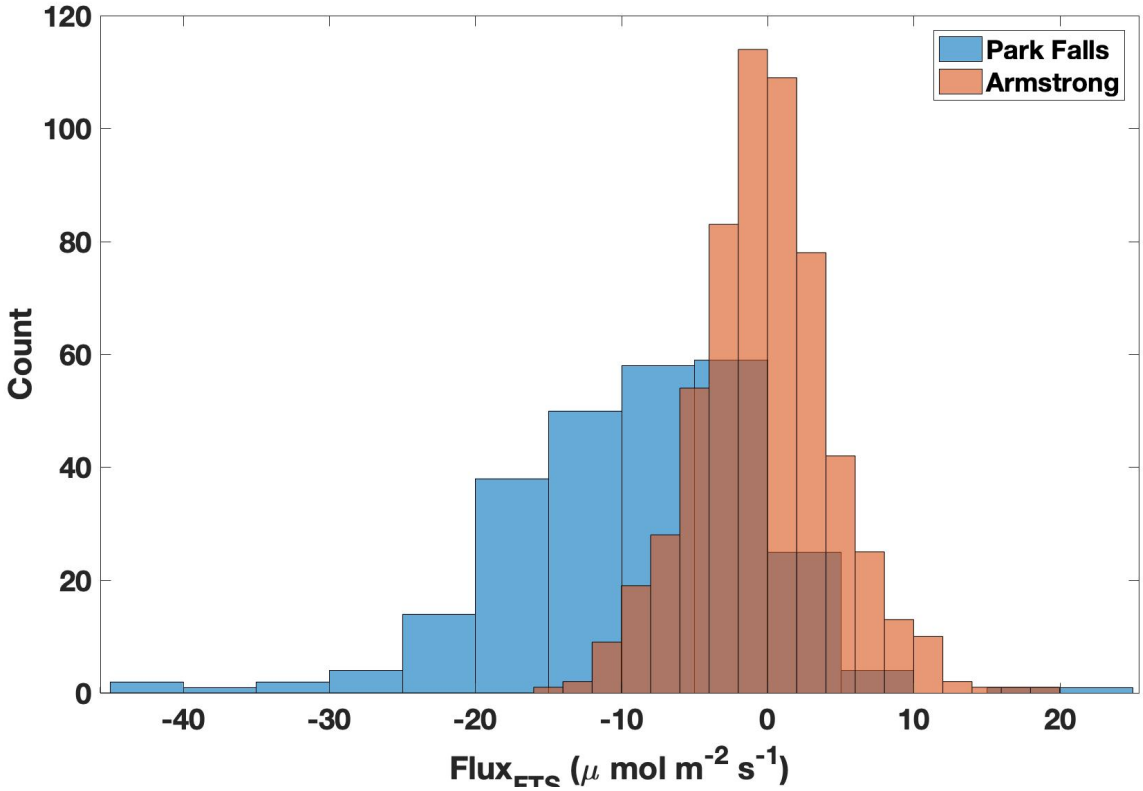

Figure 4.4: Histogram of the daily $Flux_{FTS}$ values measured at the Park Falls and Armstrong TCCON sites.

As a check on our method of using the TARDISS retrievals to evaluate diurnal changes in the lower column CO_2, we used the retrievals to estimate the diurnal fluxes at the Armstrong TCCON site in the Mojave Desert which is much less influenced by biospheric carbon fluxes than the Park Falls site. The statistics of the overall $Flux_{FTS}$ values from the Armstrong and Park Falls sites are summarized in Table C.2. Figure 4.4 shows the histograms of the daily $Flux_{FTS}$ values for each site and illustrates the influence of the biosphere on the fluxes calculated at the Park Falls site. The distribution of the fluxes calculated at the Armstrong site is mostly symmetric with the average yearly fluxes near zero (-0.635 μ mol m^{-2} s^{-1}) and a fairly large standard deviation (4.95 μ mol m^{-2} s^{-1}).

The mean Armstrong $Flux_{FTS}$ values shift from 1.14 μmol m^{-2} s^{-1} in the summer to -3.39 μmol m^{-2} s^{-1} in the winter (Fig. C.6) while the Park Falls $Flux_{FTS}$ data have a much larger

range between seasons as expected from the influence of the carbon uptake of the boreal forest. Notably the standard deviation of the daily Armstrong $Flux_{FTS}$ values does not change much from season to season suggesting that the local fluxes are similar all year round. The seasonal shift in mean flux values may be influenced by the seasonal changes in CO_2 concentrations as they occur on the daily timescale. As the seasonal standard deviations of the daily $Flux_{FTS}$ values are generally larger than the seasonal shifts in the mean, the variance in Armstrong $Flux_{FTS}$ values may represent the limit for estimating fluxes from TARDISS $<CO_2>_{LPC}$ at this point. In summary, the flux estimates from the $<CO_2>_{LPC}$ TARDISS retrievals are generally representative of the expected surface fluxes but with moderate variability that requires temporal aggregation.

4.4 Conclusions and Future Work

In this work, we compare NEE fluxes from the WLEF tall tower site with NEE flux calculations retrieved by the TARDISS algorithm from TCCON total column data from the collocated Park Falls, WI TCCON site. We use the methodology of total column flux calculation from Keppel-Aleks et al., 2012 adapted for the partial column data and compare it to the quality controlled, gap-filled, spatially-aggregated NEE values and the NEE, storage, and eddy covariance flux values at different levels on the tower.

Overall, the surface exchange estimated from the TARDISS and total column-derived data are similar, reflecting the challenge in observing the small change in CO_2 in the face of high synoptic variability. The monthly aggregated comparisons are, however, quite consistent with the surface exchange estimated from in situ data measured in Park Falls. The upper partial column follows meteorological tracers consistent with much of the variation in the $<CO_2>_{UPC}$ resulting from advection of CO_2 in free troposphere. The lower partial column is influenced by this advection, but also is strongly influenced by surface fluxes. The TARDISS estimated exchange is well correlated with the so-called ‘storage flux’ representing the change in CO_2 between the surface and 396 m. There is little

correlation between the TARDISS estimated exchange and the measured fluxes on the tower (eddy covariance).

Future work will focus on the TARDISS retrieval and integrating additional data to better understand the surface carbon fluxes. The advective signals present in the TARDISS retrievals could use data from back trajectory models and the relationship of the free tropospheric temperature to the upper column CO_2 (Fig. C.3) as prior information to further inform how to diagnose changes in $<CO_2>_{LPC}$. Other TCCON sites are collocated with tower measurements and could be used to further understand the site-by-site variances in TARDISS calculated surface CO_2 fluxes and the associated local influences. These surface flux calculations can be compared to and used to inform model simulation estimates of net ecosystem exchange. Finally, we suggest joint study of the CO_2 and water exchange to understand whether the water use efficiency could be diagnosed from the TARDISS data.

Acknowledgements

We thank NASA via 80NSSC22K1066 for support of retrievals from the TCCON stations. A portion of this research was carried out at the Jet Propulsion Laboratory, California Institute of Technology, under a contract with the National Aeronautics and Space Administration (80NM0018D0004). The in situ, tall tower data were downloaded from https://ameriflux.lbl.gov/data/download-data/?request=policy:CCBY4.0;site_id:US-PFa. We thank Ankur Desai for managing the Park Falls/WLEF tower site and for the helpful correspondences about the data.

References

Ankur Desai: AmeriFlux BASE US-PFa Park Falls/WLEF (Ver. 23-5), https://doi.org/10.17190/AMF/1246090, n.d.

Basu, S., Baker, D. F., Chevallier, F., Patra, P. K., Liu, J., and Miller, J. B.: The impact of transport model differences on CO2 surface flux estimates from OCO-2 retrievals of column average CO2, Atmos. Chem. Phys., 18, 7189–7215, https://doi.org/10.5194/acp-18-7189-2018, 2018.

Belikov, D. A., Maksyutov, S., Ganshin, A., Zhuravlev, R., Deutscher, N. M., Wunch, D., Feist, D. G., Morino, I., Parker, R. J., Strong, K., Yoshida, Y., Bril, A., Oshchepkov, S., Boesch, H., Dubey, M. K., Griffith, D., Hewson, W., Kivi, R., Mendonca, J., Notholt, J., Schneider, M., Sussmann, R., Velazco, V. A., and Aoki, S.: Study of the footprints of short-term variation in XCO2 observed by TCCON sites using NIES and FLEXPART atmospheric transport models, Atmos. Chem. Phys., 17, 143–157, https://doi.org/10.5194/acp-17-143-2017, 2017.

Berger, B. W., Davis, K. J., Yi, C., and Bakwin, P. S.: Long-Term Carbon Dioxide Fluxes from a Very Tall Tower in a Northern Forest: Flux Measurement Methodology, JOURNAL OF ATMOSPHERIC AND OCEANIC TECHNOLOGY, 18, 14, 2001.

Byrne, B., Jones, D. B. A., Strong, K., Zeng, Z.-C., Deng, F., and Liu, J.: Sensitivity of CO2 surface flux constraints to observational coverage: sensitivity to observational coverage, J. Geophys. Res. Atmos., 122, 6672–6694, https://doi.org/10.1002/2016JD026164, 2017.

Chu, H., Luo, X., Ouyang, Z., Chan, W. S., Dengel, S., Biraud, S. C., Torn, M. S., Metzger, S., Kumar, J., Arain, M. A., Arkebauer, T. J., Baldocchi, D., Bernacchi, C., Billesbach, D., Black, T. A., Blanken, P. D., Bohrer, G., Bracho, R., Brown, S., Brunsell, N. A., Chen, J., Chen, X., Clark, K., Desai, A. R., Duman, T., Durden, D., Fares, S., Forbrich, I., Gamon, J. A., Gough, C. M., Griffis, T., Helbig, M., Hollinger, D., Humphreys, E., Ikawa, H., Iwata, H., Ju, Y., Knowles, J. F., Knox, S. H., Kobayashi, H., Kolb, T., Law, B., Lee, X., Litvak, M., Liu, H., Munger, J. W., Noormets, A., Novick, K., Oberbauer, S. F., Oechel, W., Oikawa, P., Papuga, S. A., Pendall, E., Prajapati, P., Prueger, J., Quinton, W. L., Richardson, A. D., Russell, E. S., Scott, R. L., Starr, G., Staebler, R., Stoy, P. C., Stuart-Haëntjens, E., Sonnentag, O., Sullivan, R. C., Suyker, A., Ueyama, M., Vargas, R., Wood, J. D., and Zona, D.: Representativeness of Eddy-Covariance flux footprints for areas surrounding AmeriFlux sites, Agricultural and Forest Meteorology, 301–302, 108350, https://doi.org/10.1016/j.agrformet.2021.108350, 2021.

Davis, K. J., Bakwin, P. S., Yi, C., Berger, B. W., Zhao, C., Teclaw, R. M., and Isebrands, J. G.: The annual cycles of CO2 and H2O exchange over a northern mixed forest as observed from a very tall tower: CO2 AND H2O EXCHANGE OVER A NORTHERN FOREST, Global Change Biology, 9, 1278–1293, https://doi.org/10.1046/j.1365-2486.2003.00672.x, 2003.

Desai, A. R., Xu, K., Tian, H., Weishampel, P., Thom, J., Baumann, D., Andrews, A. E., Cook, B. D., King, J. Y., and Kolka, R.: Landscape-level terrestrial methane flux observed from a very tall tower, Agricultural and Forest Meteorology, 201, 61–75, https://doi.org/10.1016/j.agrformet.2014.10.017, 2015.

Feldman, A. F., Zhang, Z., Yoshida, Y., Chatterjee, A., and Poulter, B.: Using Orbiting Carbon Observatory-2 (OCO-2) column CO2 retrievals to rapidly detect and estimate biospheric surface carbon flux anomalies, Atmos. Chem. Phys., 23, 1545–1563, https://doi.org/10.5194/acp-23-1545-2023, 2023.

Keppel-Aleks, G., Wennberg, P. O., and Schneider, T.: Sources of variations in total column carbon dioxide, Atmos. Chem. Phys., 11, 3581–3593, https://doi.org/10.5194/acp-11-3581-2011, 2011.

Keppel-Aleks, G., Wennberg, P. O., Washenfelder, R. A., Wunch, D., Schneider, T., Toon, G. C., Andres, R. J., Blavier, J.-F., Connor, B., Davis, K. J., Desai, A. R., Messerschmidt, J., Notholt, J., Roehl, C. M., Sherlock, V., Stephens, B. B., Vay, S. A., and Wofsy, S. C.: The imprint of surface fluxes and transport on variations in total column carbon dioxide, Biogeosciences, 9, 875–891, https://doi.org/10.5194/bg-9-875-2012, 2012.

Kljun, N., Calanca, P., Rotach, M. W., and Schmid, H. P.: A simple two-dimensional parameterisation for Flux Footprint Prediction (FFP), Geosci. Model Dev., 8, 3695–3713, https://doi.org/10.5194/gmd-8-3695-2015, 2015.

Metzger, S.: Surface-atmosphere exchange in a box: Making the control volume a suitable representation for in-situ observations, Agricultural and Forest Meteorology, 255, 68–80, https://doi.org/10.1016/j.agrformet.2017.08.037, 2018.

Mitchell, K. A., Doney, S. C., and Keppel-Aleks, G.: Characterizing Average Seasonal, Synoptic, and Finer Variability in Orbiting Carbon Observatory-2 XCO2 Across North America and Adjacent Ocean Basins, JGR Atmospheres, 128, https://doi.org/10.1029/2022JD036696, 2023.

Novick, K. A., Biederman, J. A., Desai, A. R., Litvak, M. E., Moore, D. J. P., Scott, R. L., and Torn, M. S.: The AmeriFlux network: A coalition of the willing, Agricultural and Forest Meteorology, 249, 444–456, https://doi.org/10.1016/j.agrformet.2017.10.009, 2018.

Papale, D., Reichstein, M., Aubinet, M., Canfora, E., Bernhofer, C., Kutsch, W., Longdoz, B., Rambal, S., Valentini, R., Vesala, T., and Yakir, D.: Towards a standardized processing of Net Ecosystem Exchange measured with eddy covariance technique: algorithms and uncertainty estimation, Biogeosciences, 3, 571–583, https://doi.org/10.5194/bg-3-571-2006, 2006.

Parker, H. A., Laughner, J. L., Toon, G. C., Wunch, D., Roehl, C. M., Iraci, L. T., Podolske, J. R., McKain, K., Baier, B., and Wennberg, P. O.: Inferring the vertical distribution of CO and CO2 from TCCON total column values using the TARDISS algorithm,

Gases/Remote Sensing/Data Processing and Information Retrieval, https://doi.org/10.5194/amt-2022-322, 2022.

Schwandner, F. M., Gunson, M. R., Miller, C. E., Carn, S. A., Eldering, A., Krings, T., Verhulst, K. R., Schimel, D. S., Nguyen, H. M., Crisp, D., O'Dell, C. W., Osterman, G. B., Iraci, L. T., and Podolske, J. R.: Spaceborne detection of localized carbon dioxide sources, Science, 358, eaam5782, https://doi.org/10.1126/science.aam5782, 2017.

Site Info for US-PFa: https://ameriflux.lbl.gov/sites/siteinfo/US-PFa, last access: 26 April 2023.

Torres, A. D., Keppel-Aleks, G., Doney, S. C., Fendrock, M., Luis, K., De Mazière, M., Hase, F., Petri, C., Pollard, D. F., Roehl, C. M., Sussmann, R., Velazco, V. A., Warneke, T., and Wunch, D.: A Geostatistical Framework for Quantifying the Imprint of Mesoscale Atmospheric Transport on Satellite Trace Gas Retrievals, JGR Atmospheres, 124, 9773–9795, https://doi.org/10.1029/2018JD029933, 2019.

Wu, D., Lin, J. C., Oda, T., and Kort, E. A.: Space-based quantification of per capita CO 2 emissions from cities, Environ. Res. Lett., 15, 035004, https://doi.org/10.1088/1748-9326/ab68eb, 2020.

Wunch, D., Toon, G. C., Blavier, J.-F. L., Washenfelder, R. A., Notholt, J., Connor, B. J., Griffith, D. W. T., Sherlock, V., and Wennberg, P. O.: The Total Carbon Column Observing Network, Philosophical Transactions of the Royal Society A: Mathematical, Physical and Engineering Sciences, 369, 2087–2112, https://doi.org/10.1098/rsta.2010.0240, 2011.

Wunch, D., Wennberg, P. O., Messerschmidt, J., Parazoo, N. C., Toon, G. C., Deutscher, N. M., Keppel-Aleks, G., Roehl, C. M., Randerson, J. T., Warneke, T., and Notholt, J.: The covariation of Northern Hemisphere summertime CO2 with surface temperature in boreal regions, Atmos. Chem. Phys., 13, 9447–9459, https://doi.org/10.5194/acp-13-9447-2013, 2013.

Xu, K., Pingintha-Durden, N., Luo, H., Durden, D., Sturtevant, C., Desai, A. R., Florian, C., and Metzger, S.: The eddy-covariance storage term in air: Consistent community resources improve flux measurement reliability, Agricultural and Forest Meteorology, 279, 107734, https://doi.org/10.1016/j.agrformet.2019.107734, 2019.

Yi, C., Davis, K. J., Bakwin, P. S., Berger, B. W., and Marr, L. C.: Influence of advection on measurements of the net ecosystem-atmosphere exchange of CO2 from a very tall tower, J. Geophys. Res., 105, 9991–9999, https://doi.org/10.1029/2000JD900080, 2000.

Chapter 5

OUTLOOK

This thesis described a new method (the TARDISS algorithm) for retrieving partial column profile information from TCCON total column measurements, as well as an example of its data in use and motivation for future applications. As with any new approach, there are many avenues for future development and use of the TARDISS algorithm, and, since the algorithm can retrieve partial column data for both CO and CO_2, the applications span the topics of air quality and climate research.

The TARDISS algorithm is a useful tool and opens up a new approach to obtaining remotely-sensed profile information for atmospheric species through secondary processing, but it is still in its infancy and there are many possible ways that may improve the method that should be explored. Currently, the TARDISS algorithm uses a simple a priori covariance matrix that utilizes the temporal domain to constrain the partial column retrievals. Future implementations of the retrieval should explore the use of back trajectory models to inform the a priori covariance matrix (Wu et al., 2018). By better matching the constraints of the retrieval to the known or expected changes in the atmosphere, the partial column errors could be reduced, or the information retrieved could be improved.

In addition to exploring different a priori information applications, data from other TCCON sites around the world should be explored. The experiments in this work use data from five different TCCON sites all located in North America. Retrievals from sites in the southern hemisphere may have different information content since the CO_2 column has fluxes in the free troposphere that are largely influenced by the emissions in the northern hemisphere. Furthermore, sites worldwide located near metropolitan areas could use the partial column CO to explore emissions related to air quality.

The TARDISS algorithm focuses on retrieving information from near the surface (0-2 km), however the retrieved upper partial column is quite large (2-70 km) and further splitting it into other partial columns should be explored, particularly for CO_2. Similar to Saad et al., 2014, the connection between HF and CO_2 could be used to attempt to estimate the partial column amounts of CO_2 in the free troposphere and in the stratosphere. Isolating free tropospheric and stratospheric fluxes could further inform the use of remote sensing data to calculate carbon fluxes.

In Chapter 4, we use the TARDISS lower partial column CO_2 values to estimate the surface carbon fluxes at the heavily forested Park Falls, WI TCCON site. Our monthly aggregated flux estimates compare well to monthly averages of the 'preferred' net ecosystem exchange (NEE) fluxes estimated from collocated tall tower measurements of CO_2 and eddy covariance fluxes obtained as a part of the Chequamegon Ecosystem-Atmosphere Study (ChEAS) research cooperative and Ameriflux network (Ankur Desai, 2023; Novick et al., 2018). Again, these comparisons offer many possibilities for further exploration of the use of the partial column data.

The surface carbon fluxes in Park Falls have large influences from the biosphere that should also be correlated with measurements of photosynthetically active radiation (PAR) measured on the collocated tower and solar induced fluorescence (SIF) measured by satellite (Zhang et al., 2018). Coupling the analysis of the TARDISS derived surface flux estimates with the biospheric tracers of PAR and SIF could help us understand the influences of local uptake and mesoscale variability on flux estimates and their comparison to in situ estimates (Wu et al., 2020a).

This analysis method will also be useful at other TCCON sites with collocated in situ measurements. The TCCON sites in Lamont, Oklahoma, and East Trout Lake, Saskatchewan used in Chapter 3 both have collocated in situ measurements that could be used for comparison. East Trout Lake is similarly forested as Park Falls and would offer further insight into carbon uptake by the boreal forest and the Lamont TCCON site is

influenced by surrounding farmland and local oil and gas activity (Tribby et al., 2022) that could be explored. Similar applicable in situ measurements are made at TCCON sites worldwide and could be used for comparison with partial column data outside of flux estimates.

Chapter 2 offers a look at the changes in air quality in the South Coast Air Basin (SoCAB) from changes in traffic amounts due to the COVID-19 stay-at-home orders. The large shift in vehicular behavior led to an overall improvement in air quality with some places in the basin exhibiting signs of being NOx-limited. CO is both directly emitted in the atmosphere, is a result of the oxidation of volatile organic compounds (VOCs), and has a long lifetime compared to other pollutants, and is therefore a useful metric for understanding air quality. In SoCAB in particular, measured amounts of CO have been declining by roughly 6-8% per year (Pollack et al., 2013, Parrish et al., 2016).

As the influence of vehicular emissions on air quality is expected to continue to decrease, the importance of other emission sources will only increase as has been shown by McDonald et al., 2018. TARDISS retrievals of lower partial column CO from the TCCON site in Pasadena, CA could be coupled with local air quality measurements of particulate matter (PM), aerosol optical depth (AOD), and other VOC measurements to examine the changes in atmospheric photochemistry of SoCAB since 2016.

Further, the partial column CO and CO_2 data could be used to estimate emissions in SoCAB to compare with bottom-up estimates made by local governmental agencies. These estimates have been calculated using total column values (Wunch et al., 2009) but the use of the partial column data may reveal more insights into emission sources due to enhanced sensitivity to changes at the surface.

Overall, there is much work to be done with the TARDISS algorithm and the data derived from it. The TARDISS algorithm applied to existing TCCON data creates decades of new data to be used for comparison in both existing and novel approaches. Improvements in the

methodology would provide novel, interesting datasets that would help fill in the gaps of understanding between in situ and remote sensing methods.

References

Ankur Desai: AmeriFlux BASE US-PFa Park Falls/WLEF (Ver. 23-5), https://doi.org/10.17190/AMF/1246090, n.d.

McDonald, B. C., de Gouw, J. A., Gilman, J. B., Jathar, S. H., Akherati, A., Cappa, C. D., Jimenez, J. L., Lee-Taylor, J., Hayes, P. L., McKeen, S. A., Cui, Y. Y., Kim, S.-W., Gentner, D. R., Isaacman-VanWertz, G., Goldstein, A. H., Harley, R. A., Frost, G. J., Roberts, J. M., Ryerson, T. B., and Trainer, M.: Volatile chemical products emerging as largest petrochemical source of urban organic emissions_SI, Science, 359, 760–764, https://doi.org/10.1126/science.aaq0524, 2018.

Novick, K. A., Biederman, J. A., Desai, A. R., Litvak, M. E., Moore, D. J. P., Scott, R. L., and Torn, M. S.: The AmeriFlux network: A coalition of the willing, Agricultural and Forest Meteorology, 249, 444–456, https://doi.org/10.1016/j.agrformet.2017.10.009, 2018.

Parrish, D. D., Xu, J., Croes, B., and Shao, M.: Air quality improvement in Los Angeles—perspectives for developing cities, Frontiers of Environmental Science & Engineering, 10, 1–13, https://doi.org/10.1007/s11783-016-0859-5, 2016.

Pollack, I. B., Ryerson, T. B., Trainer, M., Neuman, J. A., Roberts, J. M., and Parrish, D. D.: Trends in ozone, its precursors, and related secondary oxidation products in Los Angeles, California: A synthesis of measurements from 1960 to 2010: OZONE TRENDS IN LA FROM 1960 TO 2010, Journal of Geophysical Research: Atmospheres, 118, 5893–5911, https://doi.org/10.1002/jgrd.50472, 2013.

Saad, K. M., Wunch, D., Toon, G. C., Bernath, P., Boone, C., Connor, B., Deutscher, N. M., Griffith, D. W. T., Kivi, R., Notholt, J., Roehl, C., Schneider, M., Sherlock, V., and Wennberg, P. O.: Derivation of tropospheric methane from TCCON CH₄ and HF total column observations, Atmospheric Measurement Techniques, 7, 2907–2918, https://doi.org/10.5194/amt-7-2907-2014, 2014.

Tribby, A. L., Bois, J. S., Montzka, S. A., Atlas, E. L., Vimont, I., Lan, X., Tans, P. P., Elkins, J. W., Blake, D. R., and Wennberg, P. O.: Hydrocarbon Tracers Suggest Methane Emissions from Fossil Sources Occur Predominately Before Gas Processing and That Petroleum Plays Are a Significant Source, Environ. Sci. Technol., acs.est.2c00927, https://doi.org/10.1021/acs.est.2c00927, 2022.

Wu, D., Lin, J. C., Fasoli, B., Oda, T., Ye, X., Lauvaux, T., Yang, E. G., and Kort, E. A.: A Lagrangian approach towards extracting signals of urban CO2 emissions from satellite observations of atmospheric column CO2 (XCO2): X-Stochastic Time-Inverted Lagrangian Transport model ("X-STILT v1"), Geosci. Model Dev., 11, 4843–4871, https://doi.org/10.5194/gmd-11-4843-2018, 2018.

Wu, D., Lin, J. C., Oda, T., and Kort, E. A.: Space-based quantification of per capita CO_2 emissions from cities, Environ. Res. Lett., 15, 035004, https://doi.org/10.1088/1748-9326/ab68eb, 2020.

Wunch, D., Wennberg, P. O., Toon, G. C., Keppel-Aleks, G., and Yavin, Y. G.: Emissions of greenhouse gases from a North American megacity: GREENHOUSE GAS EMISSIONS IN LA, Geophysical Research Letters, 36, n/a-n/a, https://doi.org/10.1029/2009GL039825, 2009.

Zhang, Y., Joiner, J., Alemohammad, S. H., Zhou, S., and Gentine, P.: A global spatially contiguous solar-induced fluorescence (CSIF) dataset using neural networks, Biogeosciences, 15, 5779–5800, https://doi.org/10.5194/bg-15-5779-2018, 2018.

Appendix A

SUPPLEMENTAL INFORMATION FOR IMPACTS OF TRAFFIC REDUCTIONS ASSOCIATED WITH COVID-19 ON SOUTHERN CALIFORNIA AIR QUALITY

A.1 Caltech Air Quality Station (CITAQS)

The Caltech Air Quality Station (CITAQS) contains a set of high sensitivity Teledyne air quality sensors including continuous measurements of PM_{10} and $PM_{2.5}$ (Teledyne T640); trace gas measurements of NO and NO_y (Teledyne T200U), CO (Teledyne M300EU2), SO_2 (Teledyne T100U); and optical trace gas measurements of O_3 (Teledyne T400) and NO_2 (Teledyne T500U) that reports at a one-minute temporal resolution. The CITAQS was deployed outside the Linde Robinson Building on Caltech campus in Pasadena, CA on March 20,2020 to continue measuring indefinitely.

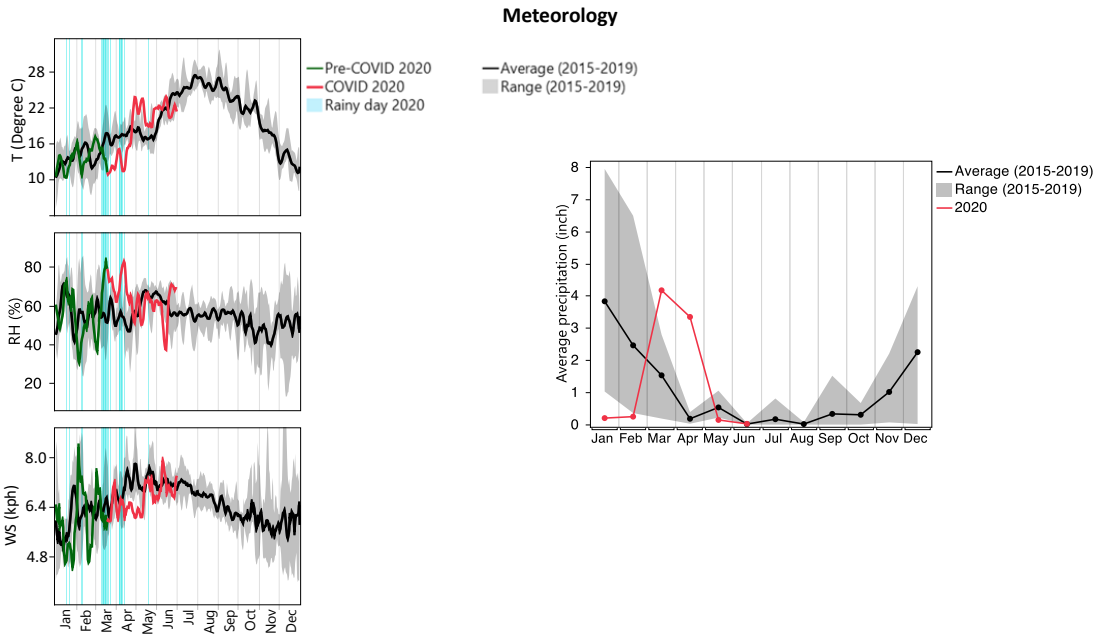

Figure A.1: Left: 7-day moving average temperature (top), relative humidity (middle), and wind speed (bottom) in 2020 and 2015 to 2019 in the South Coast Air Basin. For 2020, measurements before 19 March are in green and after 19 March are in red. The averages of the measurements for 2015 to 2019 are in black with the associated range as grey

shading. Right: Monthly average precipitation in the South Coast Air Basin in 2020 and 2015 to 2019 in centimeters per month.

Air Monitoring Site	O3	NOx	PM2.5
Anaheim	✓	✓	✓
Azusa	✓	✓	×
Banning Airport	✓	✓	✓
Compton	✓	✓	×
Central LA	✓	✓	✓
Crestline	×	×	✓
Fontana	✓	✓	×
Glendora	✓	✓	✓
La Habra	✓	✓	×
Lake Elsinore	✓	✓	✓
LAX	✓	✓	×
Mira Loma	✓	✓	✓
Pasadena	✓	✓	×
Pico Rivera	✓	✓	×
Pomona	✓	✓	×
Reseda	✓	✓	✓
Rubidoux	✓	✓	✓
San Bernardino	✓	✓	×
Santa Clarita	✓	✓	✓
South Long Beach	×	×	✓
Upland	✓	✓	✓
West LA	✓	✓	×
Temecula	×	×	✓

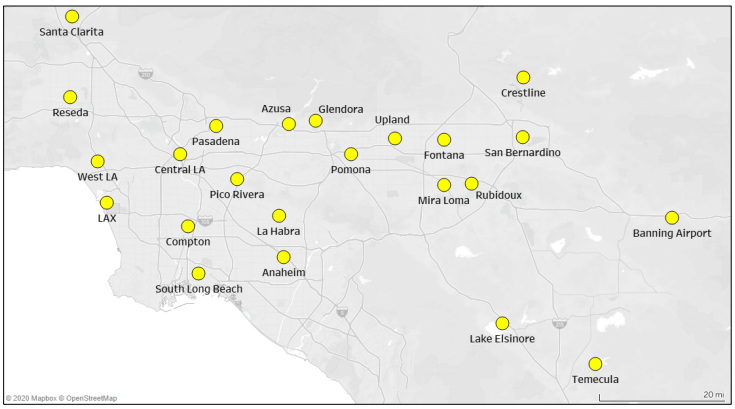

Figure A.2: Left: Breakdown of monitoring sites and the measurements included in the analysis. Right: Map of the locations of the sites described in the table on the left.

Site Name	Latitude	Longitude	2000 - 2019 NO2 trend (%/yr)	2000 - 2019 O3 trend (%/yr)	2000 - 2019 Ox trend (%/yr)	2020 NO2 Anomaly (%, ppb)	2020 O3 Anomaly (%, ppb)	2020 Ox Anomaly (%, ppb)
Banning	33.92086	-116.85841	-9.08	-0.39	-0.91	15, 0.3 (22, 0.4)	-5, -3.3 (-1, -0.4)	-3, 2.2 (1, 0.6)
San Bernardino	34.106678	-117.274063	-6.26	0.64	-0.62	-8, -0.5 (-4, -0.3)	2, 1.4 (10, 6.4)	4, 2.8 (9, 7.8)
Lake Elsinore	33.67649	-117.33098	-7.38	-0.87	-1.28	-29, -0.5 (-10, -0.2)	-6, -3.1 (-1, -0.7)	-5, -3.0 (-1,-0.4)
Fontana	34.10002	-117.49201	-6.11	0.01	-1.22	10, 0.7 (13, 0.9)	0, -0.2 (8, 4.9)	4, 3.6 (11, 7.6)
Upland	34.10374	-117.62914	-8.09	0.45	-1.22	10, 0.6 (23, 1.2)	0, 0.3 (8, 5.6)	6, 3.88 (14, 9.71)
Pomona	34.06703	-117.7514	-6.96	0.44	-1.53	-18, -1.3 (-15, -1.1)	8, 4.7 (17, 9.9)	11, 6.9 (19, 11.7)
Glendora	34.14435	-117.85036	-6.67	0.11	-1.35	-20, -1.5 (-12, -0.9)	4, 2.7 (12, 7.8)	5, 3.3 (13, 8.9)
Azusa	34.1365	-117.92391	-5.24	0.41	-1.00	-26, -2.4 (-20, -1.8)	4, 2.1 (11, 6.7)	2, 1.5 (10, 6.6)
La Habra	33.92513	-117.95264	-7.14	0.17	-1.28	-9, -0.4 (-1, 0.0)	-1, -0.7 (4, 2.2)	2, 0.8 (7, 3.8)
Pasadena	34.1326	-118.1272	-6.56	0.11	-1.53	-16, -1.0 (-14, -0.7)	16, 8.6 (20, 12.6)	16, 9.4 (23, 13.2)
Central LA	34.06659	-118.22688	-4.90	-0.09	-1.43	-31, -2.5 (-24, -1.9)	-3, -1.4 (5, 2.4)	-6, -3.1 (2, 1.1)
West LA	34.05111	-118.45636	-6.83	-0.18	-0.93	95, 2.5 (176, 3.7)	-13, -6.5 (-10, -4.8)	-6, -3.1 (0, -0.1)
Reseda	34.19925	-118.53276	-5.70	0.46	-0.39	-33, -1.3 (-34, -1.4)	-8, -5.0 (-3, -1.8)	-7, -4.8 (-3, -2.0)
Average East of 117.75 W			-7.38	-0.03	-1.05	0, 0 (9, 0.2)	-2, -1.3 (5, 2.6)	1, 0.3 (7, 3.9)
Average West of 117.75 W			-6.35	0.18	-1.21	-7, -0.9 (7, -0.3)	-2, -0.5 (7, 4.5)	2, 1.6 (9, 5.9)
Average			-6.82	0.07	-1.13	-4, -0.6 (8, -0.2)	-2, 0.0 (6, 3.9)	2, 1.2 (8, 5.3)

Table A.1: 2000 to 2019 trends and 2020 anomalies in afternoon (12:00 - 16:00 local) NO2, O3, and Ox concentrations for sites in the basin that have measurements of both NO2 and O3 for the 2000 to 2020 period. Anomalies represent the difference between values observed during 2020 COVID period afternoons and the values expected from a 2000-2019 fit of COVID period afternoons. Values in parentheses represent the anomaly values for the 19 April to 30 June period instead of the 19 March to 30 June period.

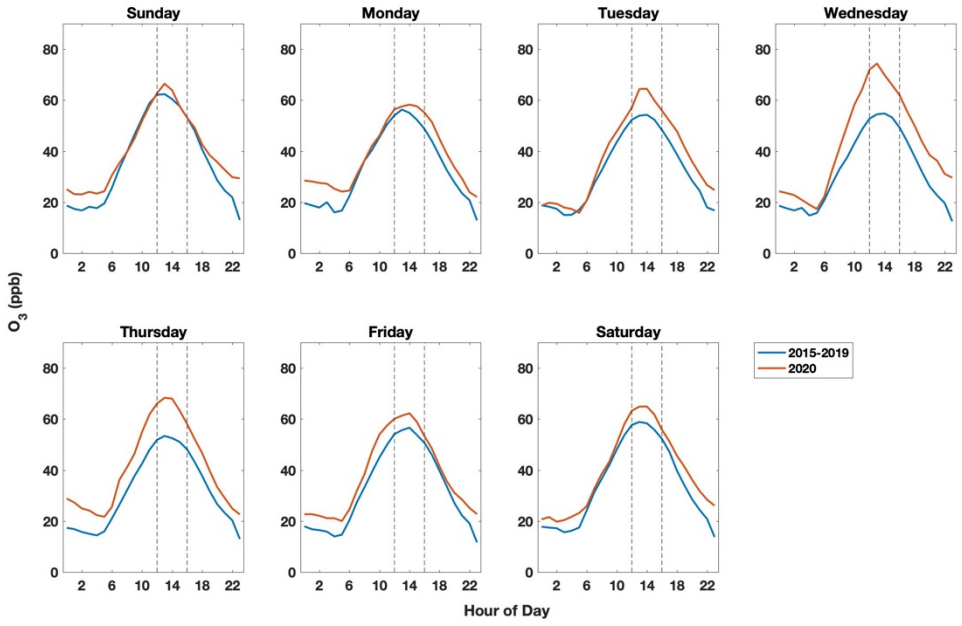

Figure A.3: Plots of mean O3 concentrations by hour of day and day of week in Pasadena for our analysis period in 2020 and the average of 2015 to 2019. Vertical lines mark 12pm and 4pm respectively in each plot.

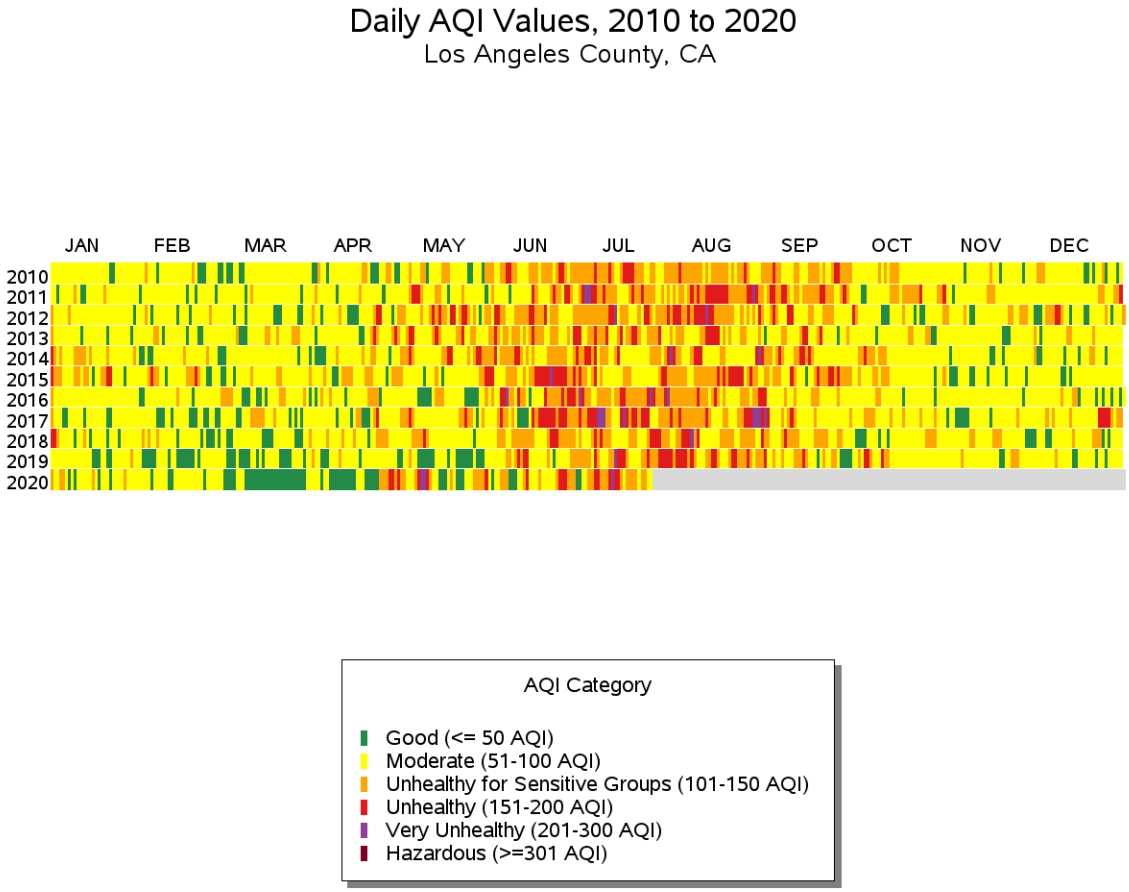

Figure A.4: Air quality index time series for daily AQI values for LA county for 2010 to 2020 generated on the EPA website (https://www.epa.gov/outdoor-air-quality-data/air-data -multiyear-tile-plot).

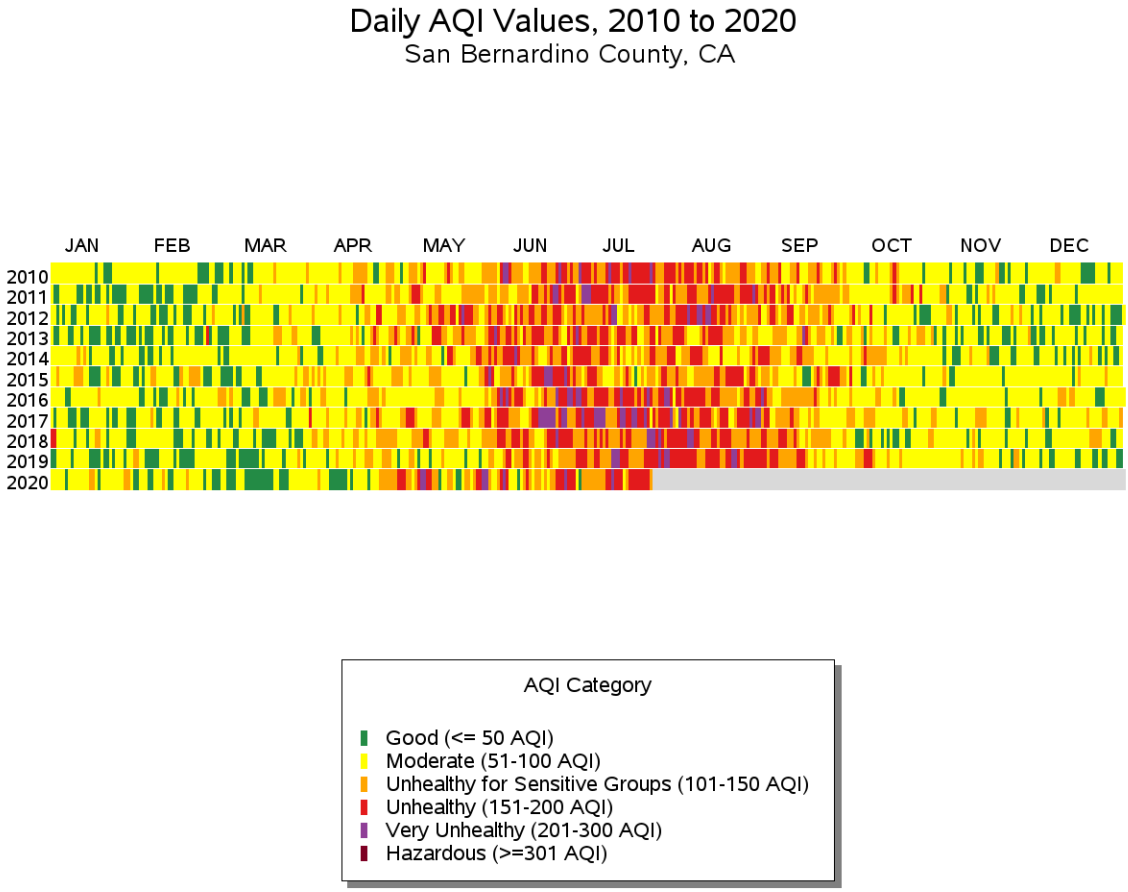

Figure A.5: Air quality index time series for daily AQI values for San Bernardino County for 2010 to 2020 generated on the EPA website (https://www.epa.gov/outdoor-air-quality-data/ air-data-multiyear-tile-plot).

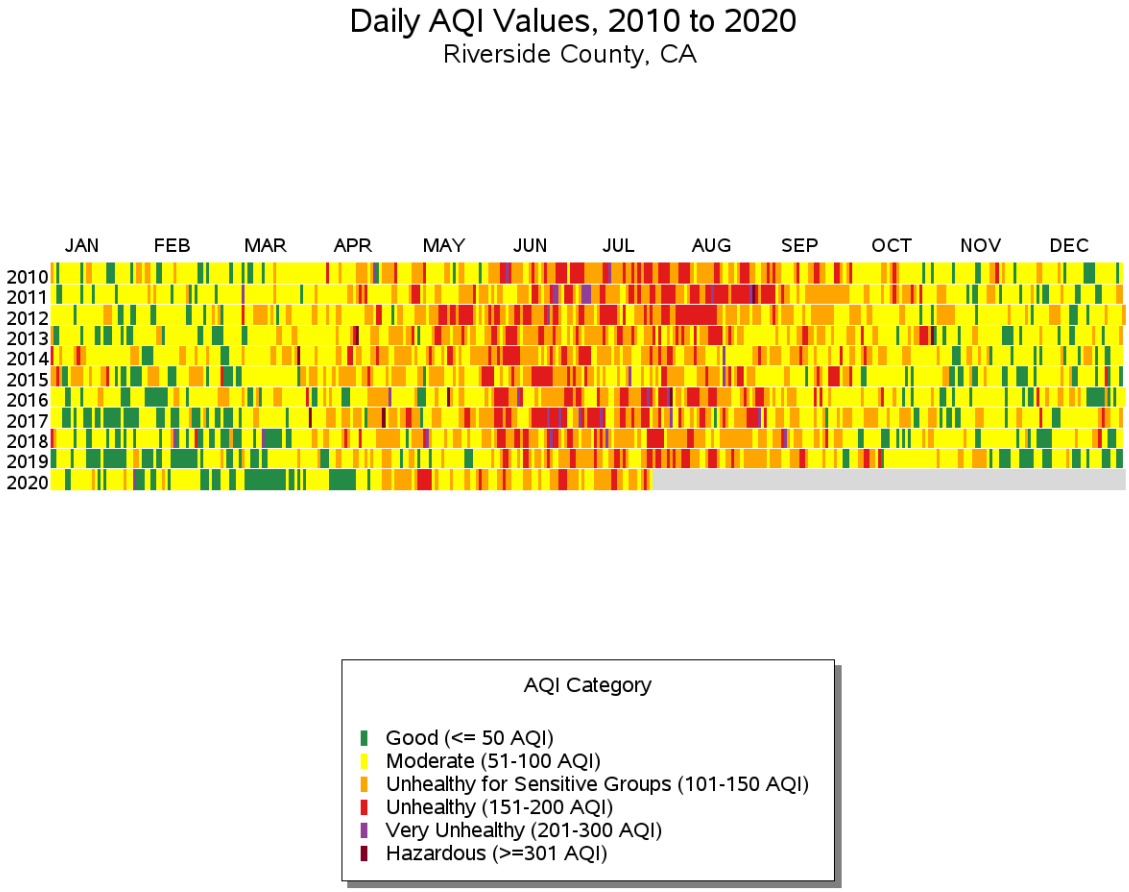

Figure A.6: Air quality index time series for daily AQI values for Riverside County for 2010 to 2020 generated on the EPA website (https://www.epa.gov/outdoor-air-quality-data/ air-data-multiyear-tile-plot).

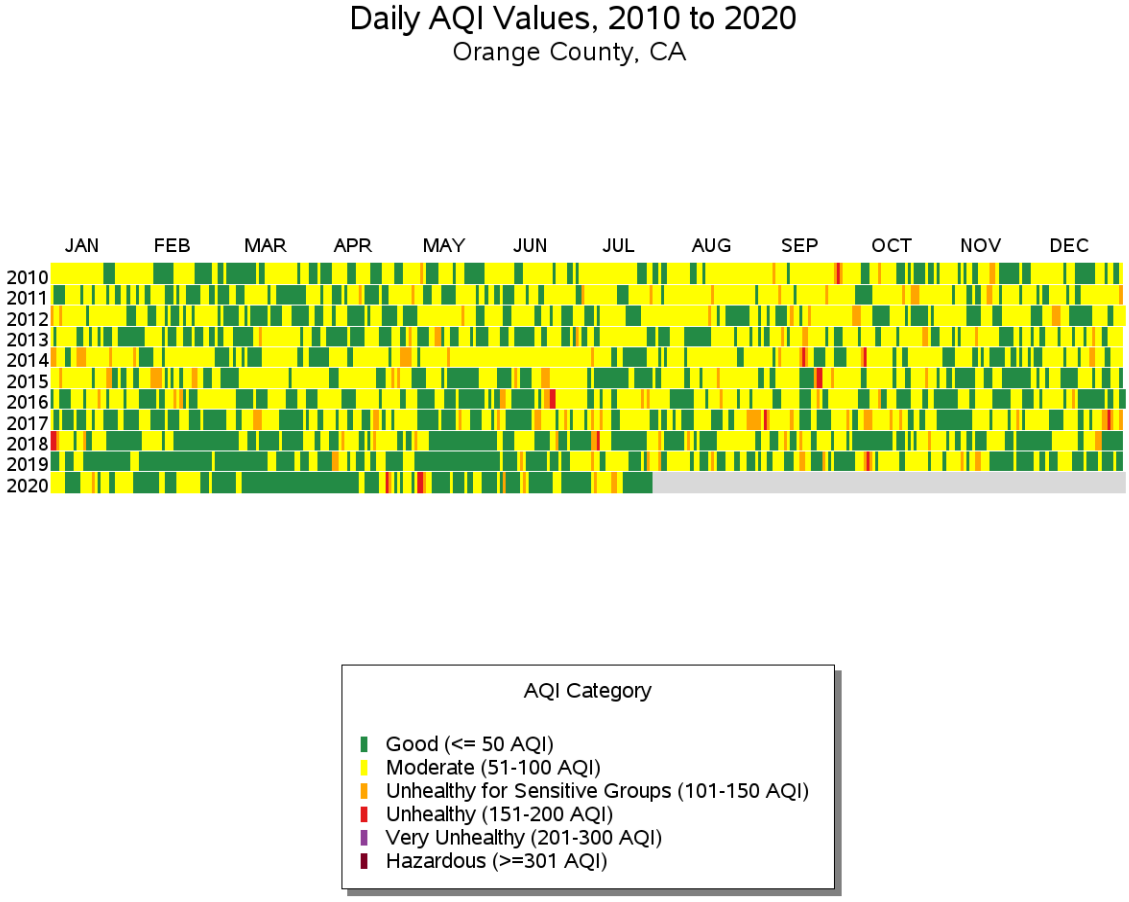

Figure A.7: Air quality index time series for daily AQI values for Orange County for 2010 to 2020 generated on the EPA website (https://www.epa.gov/outdoor-air-quality-data/ air-data-multiyear-tile-plot).

Basin Maximum

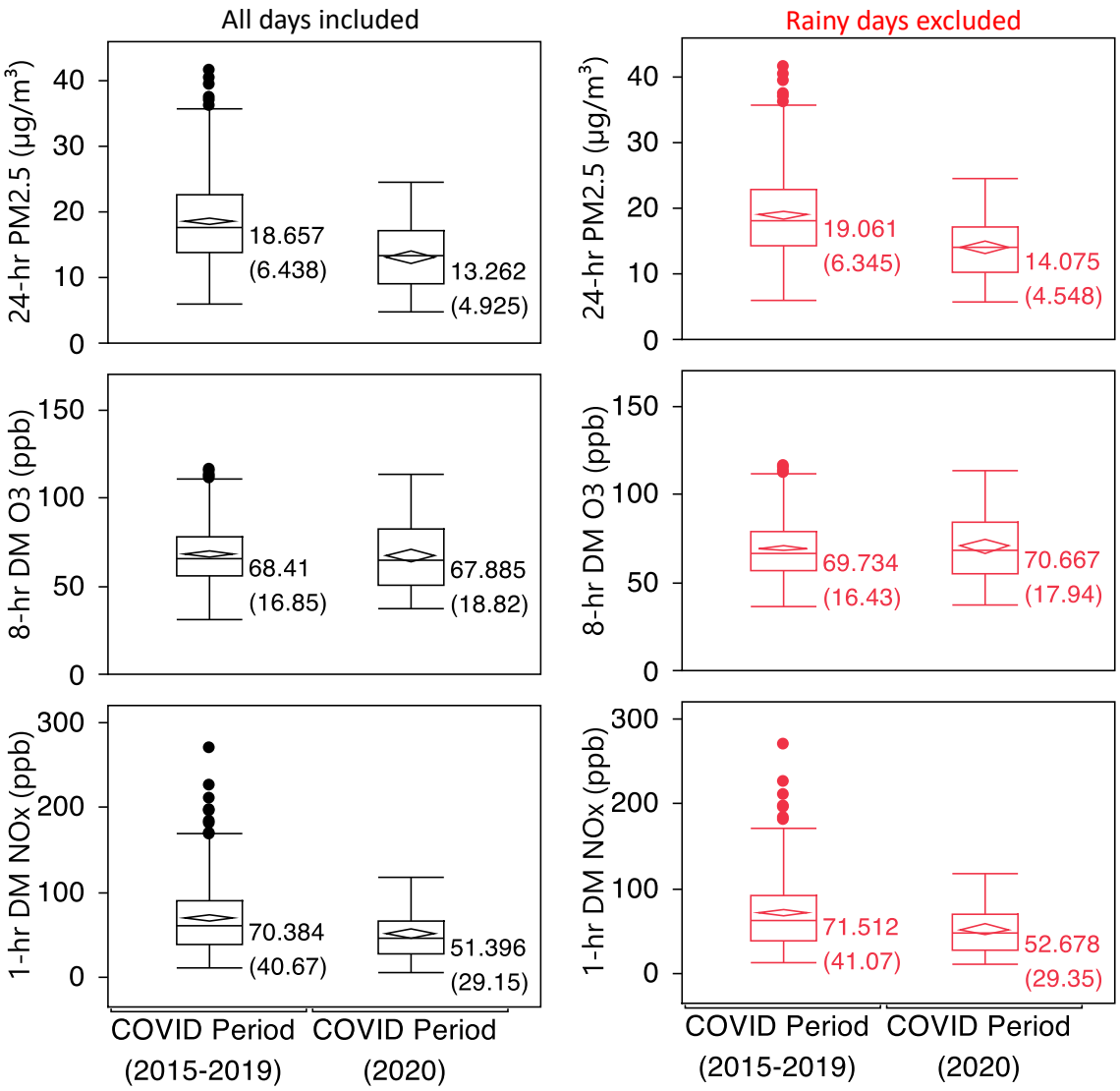

Figure A.8: Sensitivity test by excluding the rainy days from the analysis (right, in red) in comparison to including all the days (left, in black). The means are reported to the right of the box plots with the standard deviation in parenthesis.

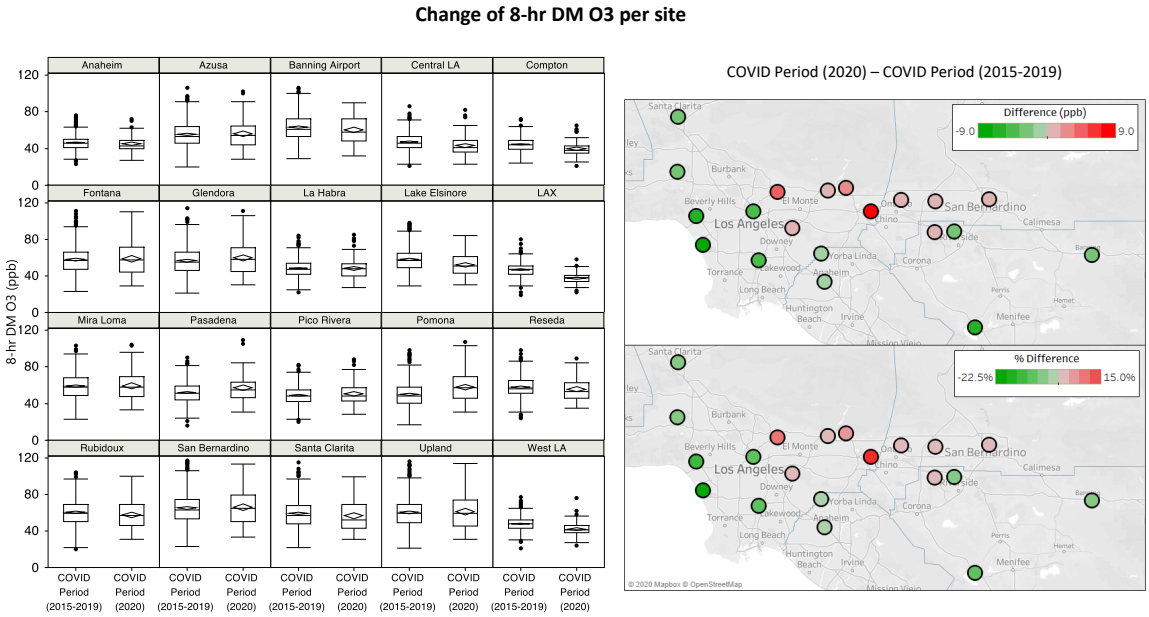

Figure A.9: Left: Box plots of 8-hr DM O3 values during the 2015 to 2019 COVID period and 2020 COVID period. Right: Map of the difference between the 2015 to 2019 COVID period and 2020 COVID period in parts per billion (top) and percentage (bottom).

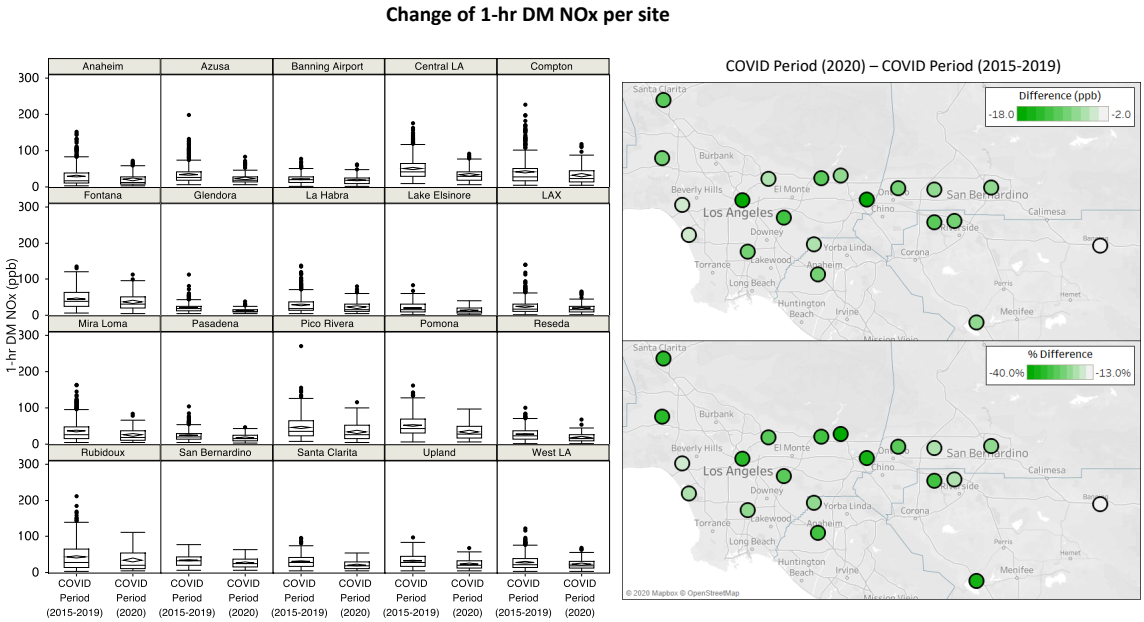

Figure A.10: Left: Box plots for 1-hr daily maximum NOx values during the 2015 to 2019

COVID period and 2020 COVID period. Right: Map of the difference between the 2015 to 2019 COVID period and 2020 COVID period in parts per billion (top) and percentage (bottom).

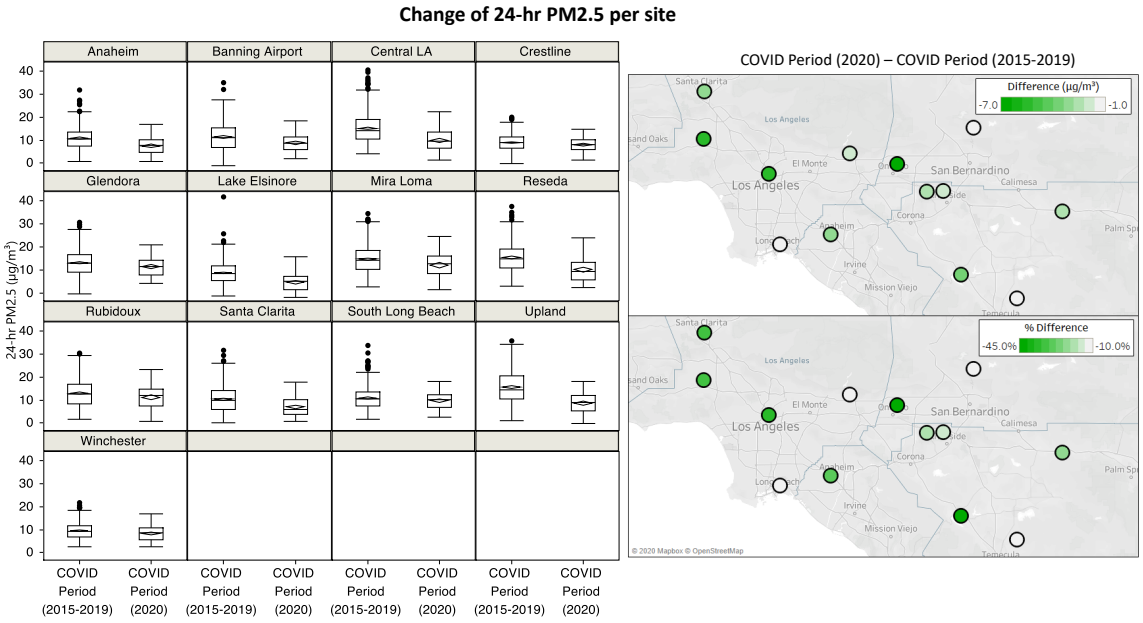

Figure A.11: Left: Box plots for 24-hr PM2.5 values during the 2015 to 2019 COVID period and 2020 COVID period. Right: Map of the difference between the 2015 to 2019 COVID period and 2020 COVID period in µg m−3 (top) and percentage (bottom).

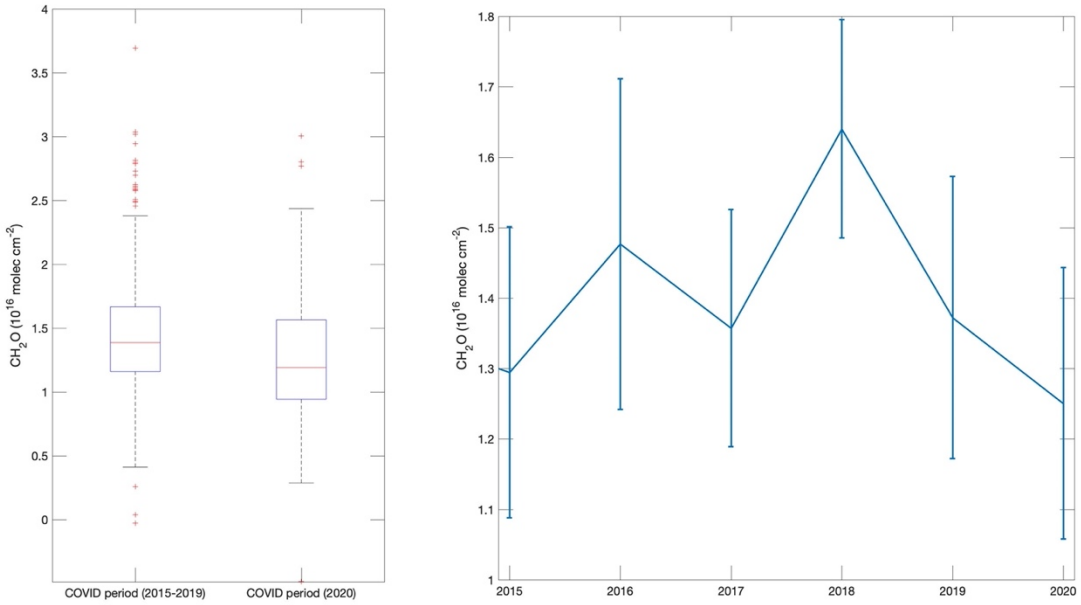

Figure A.12: Left: Box plots for the column CH2O concentrations for the COVID period for 2015 to 2019 and for 2020. Right: Time series of the yearly COVID period CH2O concentrations. Error bars represent the standard error in the mean.

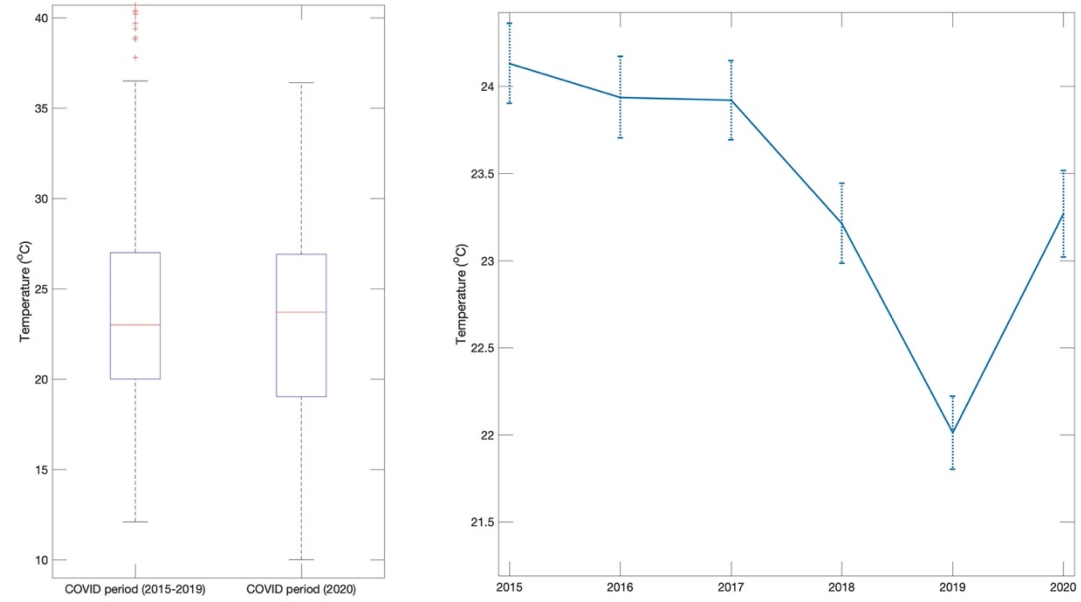

Figure A.13: Left: Box plots for the Pasadena temperature measurements for the COVID period for 2015 to 2019 and for 2020. Right: Time series of the yearly COVID period temperature measurements. Error bars represent the standard error in the mean.

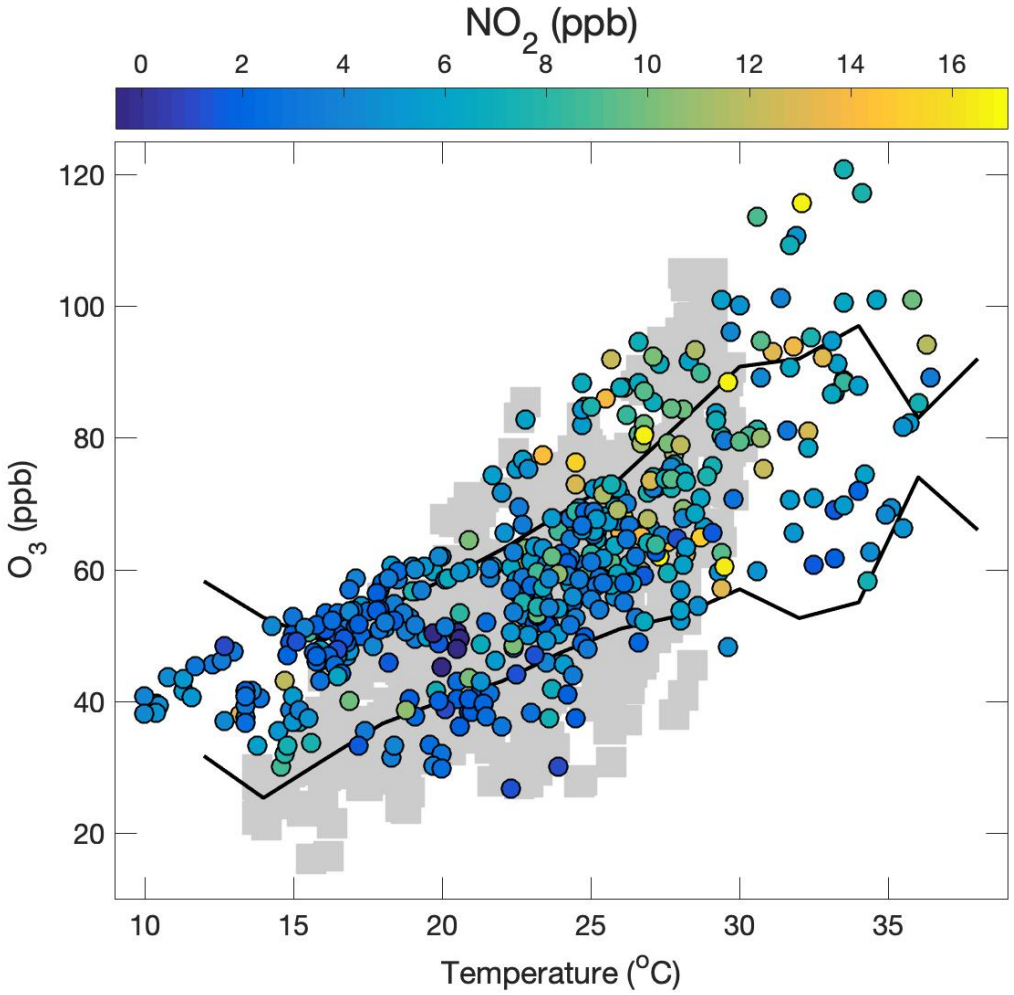

Figure A.14: Hourly afternoon O3 concentrations are plotted against temperature and color coded by NO2, all in ppb. The grey boxes are CalNex O3 concentrations in ppb. All data shown here is from Pasadena. In the left and middle panels, the upper and lower black lines are the 10% and 90% quantile values for the 2015 to 2019 values, respectively.

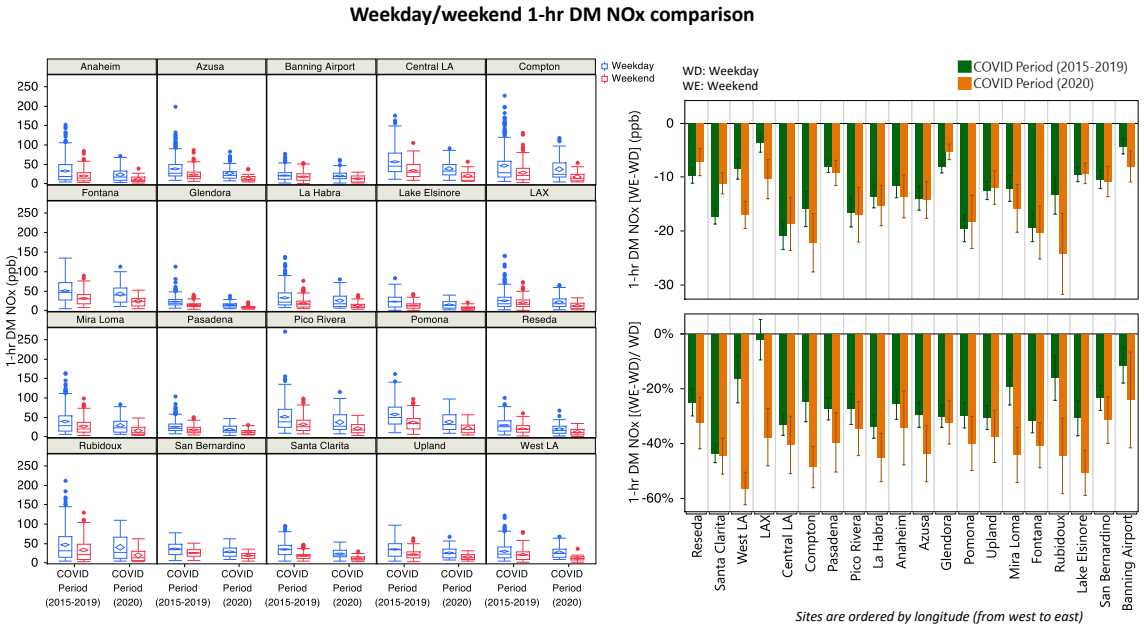

Figure A.15: Left: Box plots for weekend(red) and weekday(blue) 1-hr daily maximum NOx for the COVID period in 2020 and 2015 to 2019. Right: Difference between weekend and weekday 1- hr daily maximum NOx for the COVID period in 2020 and 2015 to 2019 in parts per billion(top) and percent(bottom). Error bars represent the standard error in the mean.

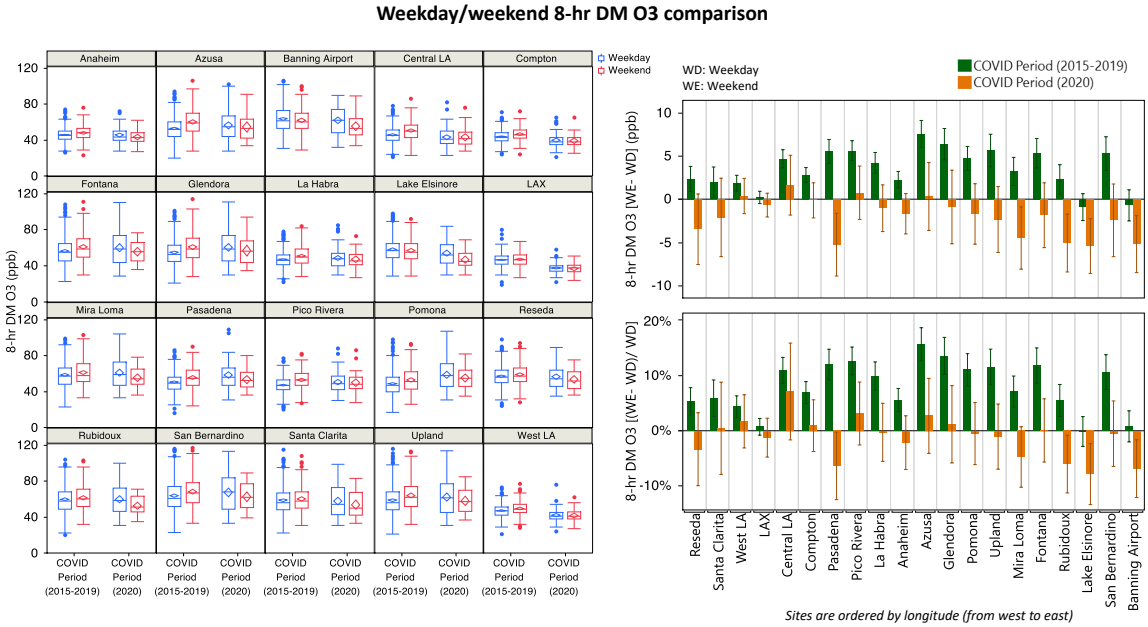

Figure A.16: Left: Box plots for weekend(red) and weekday(blue) 8-hr daily maximum O_3 for the COVID period in 2020 and 2015 to 2019. Right: Difference between weekend and weekday 8-hr daily maximum O_3 for the COVID period in 2020 and 2015 to 2019 in

parts per billion(top) and percent(bottom). Error bars represent the standard error in the mean.

Appendix B

SUPPLEMENTAL INFORMATION FOR INFERRING THE VERTICAL DISTRIBUTION OF CO AND CO_2 FROM TCCON TOTAL COLUMN VALUES USING THE TARDISS ALGORITHM

Variable Name	Variable Description	Defining Equation
$\mathbf{A}$	TARDISS temporal averaging kernel	~
$\mathbf{A}_{\text{vert}}$	TARDISS sensitivity as it relates to the vertical profile	3.22
$\boldsymbol{a}^{\xi}_{TCCON}$	TCCON column averaging kernel vector dotted with an integration operator	~
$\boldsymbol{a}_{\text{TCCON}}$	TCCON column averaging kernel vector	~
χ	Cost of retrieval	3.1
$\mathbf{G}$	Gain matrix of temporal retrieval	3.21
DoF	Degrees of Freedom of signal	3.18
γ_L	Lower partial column scalar	~
γ_U	Upper partial column scalar	~
$\gamma_{a,L}$	A priori lower partial column scalar	~
$\gamma_{a,U}$	A priori upper partial column scalar	~
H	Shannon information content	3.19
$\mathbf{I}$	Identity matrix	~
i	Index value	~
$\boldsymbol{K}$	TARDISS Jacobian matrix	3.12
k_L	Lower partial column TARDISS Jacobian element for one window for one spectrum	3.8
k_U	Upper partial column TARDISS Jacobian element for one window for one spectrum	3.9
n_l	Number of levels in a vertical profile	~
n_s	Number of TCCON spectral measurements in a day	~
n_w	Number of TCCON windows used in the TARDISS retrieval	~

q	Index of the top of the lower partial column part of the profile	~
$\boldsymbol{S}_a$	A priori covariance matrix	~
$\boldsymbol{S}_\epsilon$	Model covariance matrix	~
$\boldsymbol{S}_r$	Retrieval noise matrix	3.26
$\boldsymbol{S}_s$	Smoothing error matrix	3.25
$\boldsymbol{\sigma}$	TARDISS retrieval errors	~
VEM	Validation Error Multiplier	3.27
$\boldsymbol{x}_{\mathrm{a},\gamma}$	Vector of a priori partial column scalar values	3.14
$\mathrm{x}_{\mathrm{a,TCCON}}$	TCCON a priori profile times median of TCCON VSFs for one measurement	~
$\hat{\boldsymbol{x}}_\gamma$	Retrieved state vector of partial column scalar values	3.16
$\hat{x}_{\gamma L}$	Lower partial column element of the retrieved state vector	~
$\hat{x}_{\gamma U}$	Upper partial column element of the retrieved state vector	~
$\boldsymbol{x}_\gamma$	Theoretical state vector of partial column scalar values	3.13
$\boldsymbol{x}_{L2}$	Vector of partial column scalar values calculated via the least squares method	3.15
$\mathbf{x}_{\mathrm{part}}$	A posteriori profile	3.2
$\boldsymbol{x}_{true}$	In situ measured profile	~
$\boldsymbol{y}$	Measurement vector with elements defined by $\mathrm{z_{TCCON}} - \mathrm{z_{a,TCCON}}$	3.10, 3.11
$\boldsymbol{\Xi}_{TCCON}$	Matrix of TCCON column averaging kernels for each window and each spectrum within a day	3.23
z_{TCCON}	TCCON column average mole fraction value for one window and one specturm	3.3
$z_{a,TCCON}$	TCCON a priori column average mole fraction times the median VSF of the windows used	~
$z_{a,L,TCCON}$	Lower partial column of TCCON a priori column average mole fraction times the median VSF of the windows used	~
$z_{a,U,TCCON}$	Upper partial column of TCCON a priori column average mole fraction times the median VSF of the windows used	~
$\hat{\boldsymbol{z}}_{comp}$	Vector of partial column mole fractions used for comparison to the smoothed column averaged in situ mole fraction	~
$\boldsymbol{z}_{PC}$	Vector of reconstructed partial column mole fraction values for a day of measurement	3.17
$z_{PC,L}$	Lower partial column element of the reconstructed partial column mole fraction vector	~
$z_{PC,U}$	Upper partial column element of the reconstructed partial column mole fraction vector	~

$\hat{z}_s$	Smoothed column or partial column averaged in situ mole fraction	3.20, 3.24

Table B.1: Table of variable names, descriptions, and defining equation for all the variables used in the work.

B.1 Temporal Assimilation

To test the influence of the number of observations included in each TARDISS retrieval, we compare the retrieved error value for each individual retrieval and with an increasing number of observations until we use the full day of observations. In this test, we take the midday observation from the Park Falls site on July 18, 2018 and retrieve the partial column error values using the least squares method and the maximum a posteriori method (using a static ideal a priori scalar to avoid influences from the least squares approach). These values are represented by the points that correspond with zero on the x axis of Fig. B.1 for both the lower and upper partial column errors. We then retrieve the errors of the midday measurement again including the observation before and after it which is represented by the points that correspond with 2 on the x axis of Fig. B.1. We repeat this method, expanding the number of observations included until we use the entire day of observations.

The left-hand plot of Fig. B.1 shows the decrease of the retrieved upper and lower partial column error of the midday point as the number of observations included in the retrieval increases. The upper partial column errors decrease more than the lower partial column errors partially due to the temporal constraints of the a priori covariance matrix. In contrast, the right-hand plot of Fig. B.1 shows that the inclusion of more observations in the least squares fit does not change the retrieved partial column errors of the midday measurement. Moreover, the partial column errors retrieved using the least squares method are at least eight times larger than the partial column errors retrieved using the MAP method. This is due to the use of the a priori covariance matrix in the MAP method that can improve upon the best estimate retrieval of the least squares method.

To understand the influence of the a priori covariance matrix (overall scaling and temporal constraints), we compare the error values of the least squares method with the MAP method with an entirely uninformed a priori covariance matrix. Shown in Fig. B.2, the uninformed MAP approach returns errors of similar magnitude to the least squares method. This suggests that a main value of the MAP approach is the use of constraints and external information to improve and inform the retrieval.

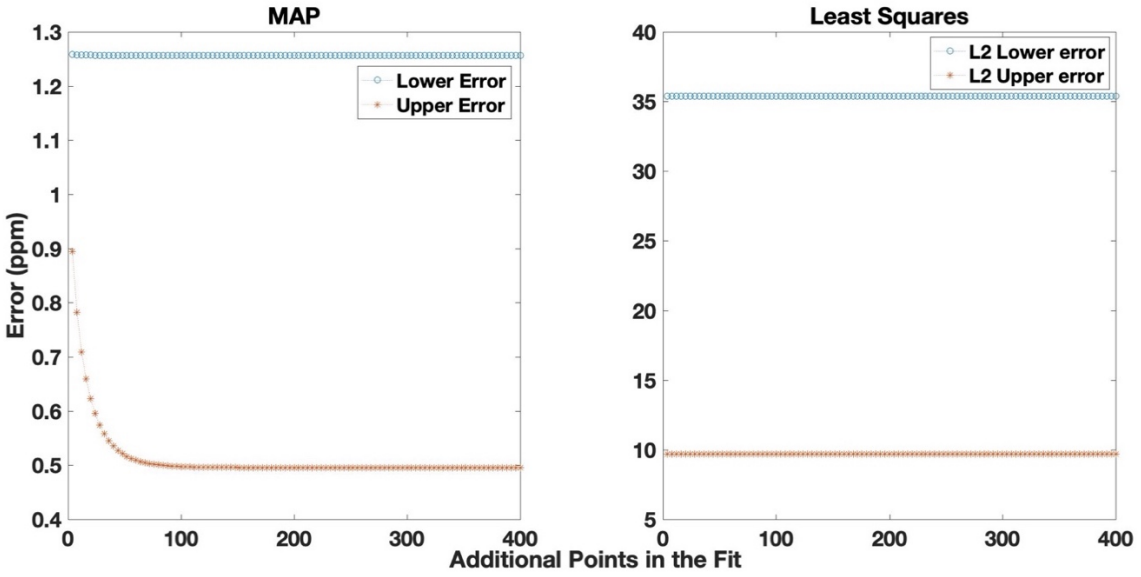

Figure B.1: Errors in the retrieval of CO_2 from the midday total column measurement at the Park Falls site on July 18, 2018 using the MAP method outlined by Equation 3.13 and the least squares method outlined by Equation 3.12. The blue circles represent the error in the lower partial column and the orange asterisks represent the error in the upper partial column. Note the difference in the range of the y axis in the left and right plots both of which are in parts per million. The x axis indicates the number of points included in the overall fit with zero additional points representing the retrieval of a single spectrum.

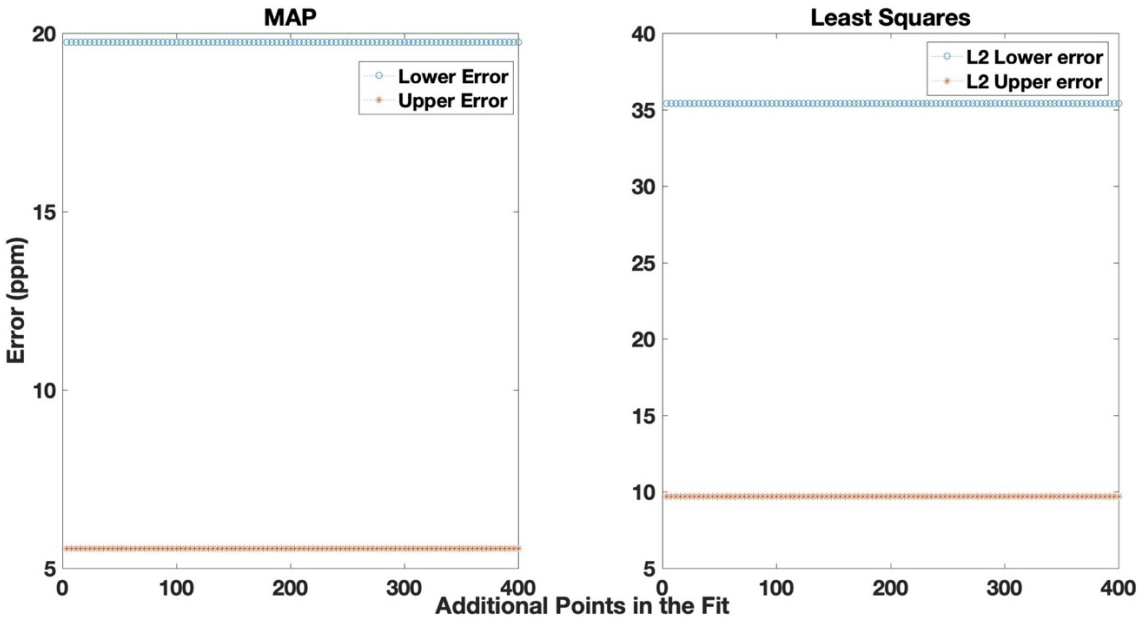

Figure B.2: Same as Fig. B.1, except the a priori covariance is removed from the MAP retrieval.

Site	Type	Species	Campaign/ Program	Data Availability	Dates	Altitudes
Park Falls	Aircraft	CO_2	ATom	https://doi.org/10.3334/ORNLDAAC/1925	20160822	0.79 - 12 km
	AirCore	CO_2	NOAA AirCore	https://doi.org/10.15138/6AV0-MY81	20180730 20180731	Surf. – 21km
Armstrong	Aircraft	CO_2	SEAC4RS	https://doi.org/10.3334/ORNLDAAC/1925	20130923	1.5 - 19 km
Armstrong	Aircraft	CO_2	ATom	https://doi.org/10.3334/	20140820	0.79 - 12 km

				ORNLDAAC/1925		
Armstrong	Aircraft	CO_2	GSFC	https://doi.org/10.25925/20190319	20140820 20140822 20151002 20160210	0.6 - 13 km
Armstrong	Aircraft	CO_2	KORUS-AQ	https://doi.org/10.1525/elementa.2020.00163	20160618	0.68 - 12 km
Armstrong	AirCore	CO_2	NOAA AirCore	https://doi.org/10.15138/6AV0-MY81	20180716 20180717 20180718	Surf. – 21 km
Lamont	AirCore	CO_2, CO	NOAA AirCore	https://doi.org/10.15138/6AV0-MY81	20180723 20180725 20180727	Surf. – 21 km Surf. – 17 km
Lamont	Aircraft	CO_2, CO	NOAA GGGRN aircraft program	https://doi.org/10.1002/2014JD022591, 2015.	2008 - 2018	0.17 - 6 km
East Trout Lake	Aircraft	CO_2, CO	NOAA GGGRN aircraft program	https://doi.org/10.1002/2014JD022591, 2015.	2017 - 2020	0.17 - 7 km

Table B.2: Site, measurement type, species, campaign or program, citation, and dates of the in situ profile data used in this work.

TCCON Window (cm^{-1})	Total Column Validation Slope	Total Column Validation Slope Error	Total Column Mean Ratio Deviation
CO_2			
6220	1.007	0.001	0.001
6339	1.004	0.001	0.002
6073	1.006	0.001	0.001
4852	1.006	0.001	0.003
TARDISS CO_2	1.000	0.0004	0.001
CO			
4290	1.009	0.055	0.056
2160	1.033	0.020	0.041
2111	1.053	0.020	0.052
TARDISS CO	1.047	0.019	0.052

Table B.3: Comparisons of the TARDISS total column retrieval to the total column comparisons of the fits of the TCCON spectral windows used as input for the TARDISS algorithm. The data in the TARDISS row uses the operational parameters for the fit that are identified in Table 3.2 and 3.3 by an asterisk.

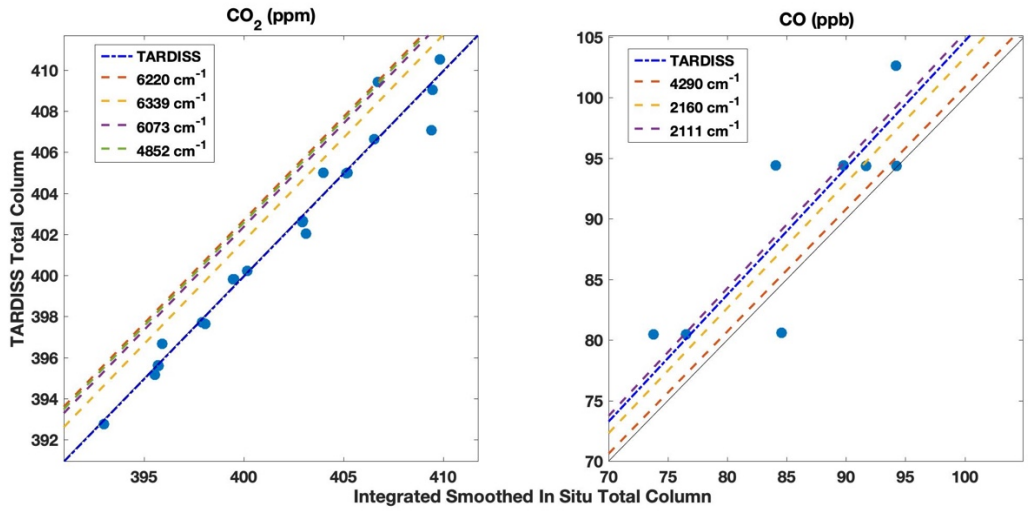

Figure B.3: The direct comparisons between the total column DMF values retrieved from the TARDISS fit and the integrated, smoothed in situ partial columns for CO_2 (left) and the CO (right). The black solid line is the 1-1 line and the blue dot-dash line is the linear fit of the data with the y-intercept forced through zero. The slopes of the partial column validation of the TCCON spectral windows used in the retrieval are represented by dashed lines.

Site	Long Term Total Degrees of Freedom per Measurement	Long Term Comparison Slope	Lower partial column VEM from long-term data	Long term VEM total lower partial column error (ppm for CO_2; ppb for CO)
CO_2				
Lamont	0.0473	1.002	1.00	1.23
East Trout Lake	0.0543	1.001	1.30	1.64
CO				
Lamont	0.144	1.000	1.00	1.18
East Trout Lake	0.155	0.945	6.97	8.14

Table B.4: DoF, comparison slopes, VEM, and total errors in the CO and CO_2 lower partial column retrievals for the long term comparisons performed at the Lamont and East Trout Lake sites. The values for total retrieval error and total error represent one standard deviation.

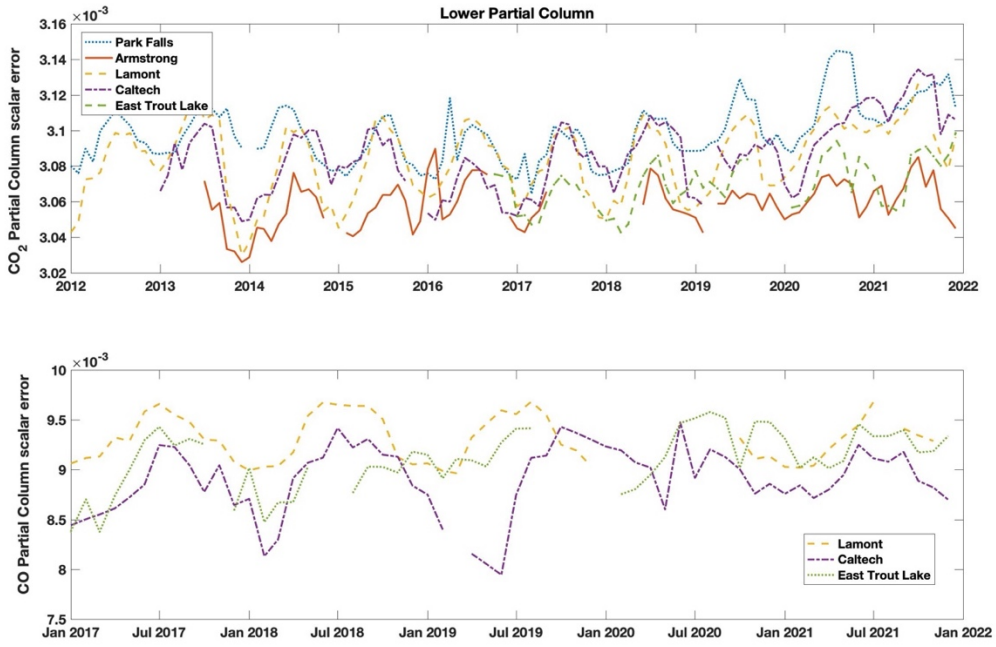

Figure B.4: Monthly mean lower partial column scalar errors plotted for CO_2 (top) and CO (bottom).

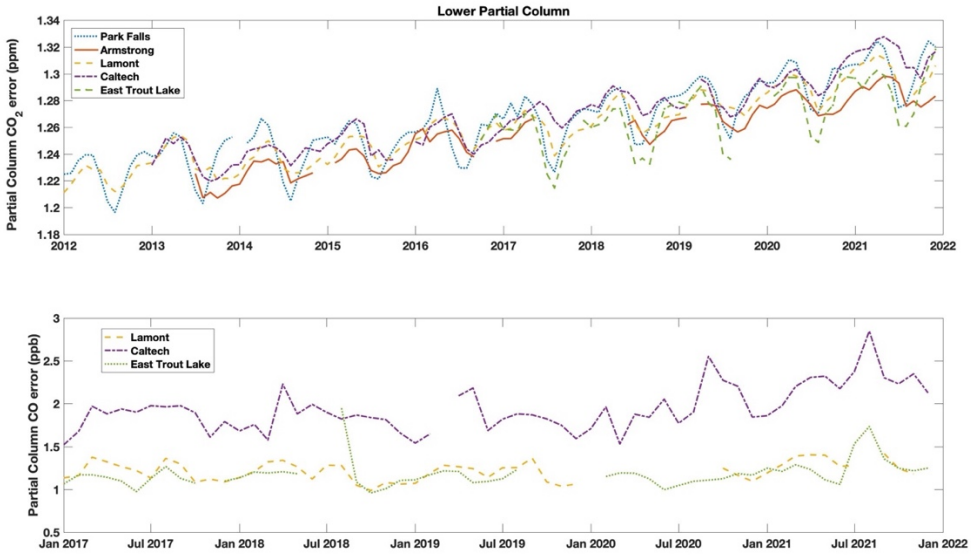

Figure B.5: Monthly mean lower partial column errors plotted for CO_2 in ppm (top) and CO in ppb (bottom).

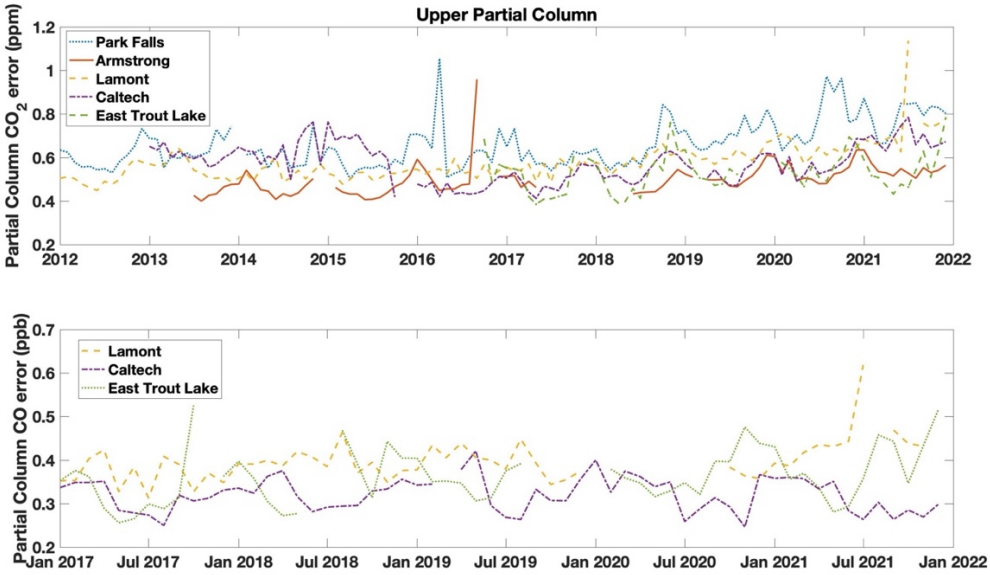

Figure B.6: Monthly mean upper partial column errors plotted for CO_2 in ppm (top) and CO in ppb (bottom).

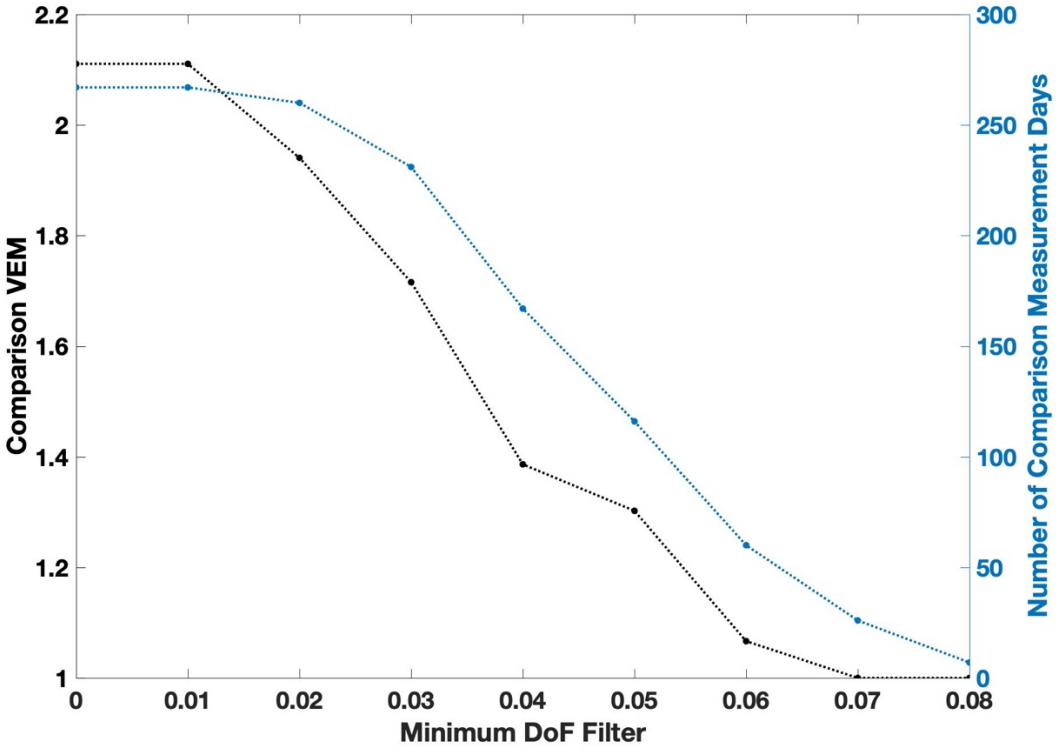

Figure B.7: Comparison Validation Error Multiplier (VEM) and number of comparison days plotted by the minimum DoF per measurement filter applied to the comparison data. The retrieved data is in comparison with in situ data measured as a part of the NOAA GGGRN (Global Greenhouse Gas Reference Network) Aircraft sites from 2008 -2018 at the Lamont measurement site.

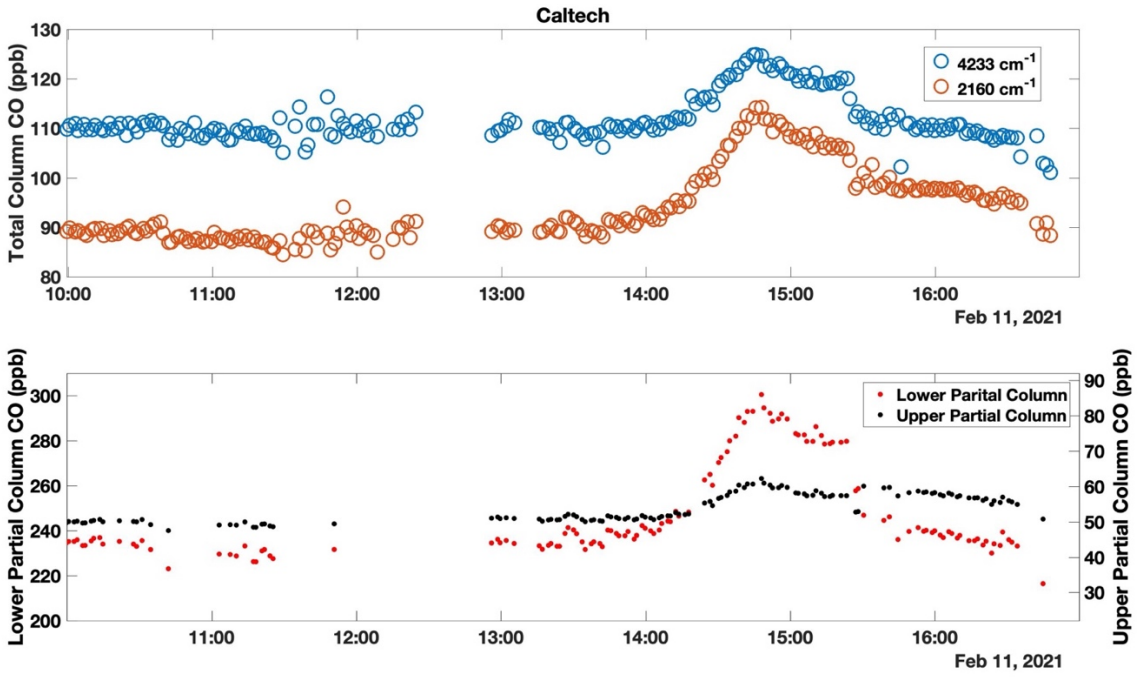

Figure B.8: Example of one day of TCCON retrievals of total column CO (top) from two different spectral windows (4233 in blue and 2160 in orange) above the TARDISS partial column retrievals for CO (lower partial column in red dots, upper partial column in black dots) for the same day (bottom).

Appendix C

SUPPLEMENTAL INFORMATION FOR ASSESSING SURFACE FLUXES OF CARBON DIOXIDE USING A NOVEL REMOTE-SENSING DATASET

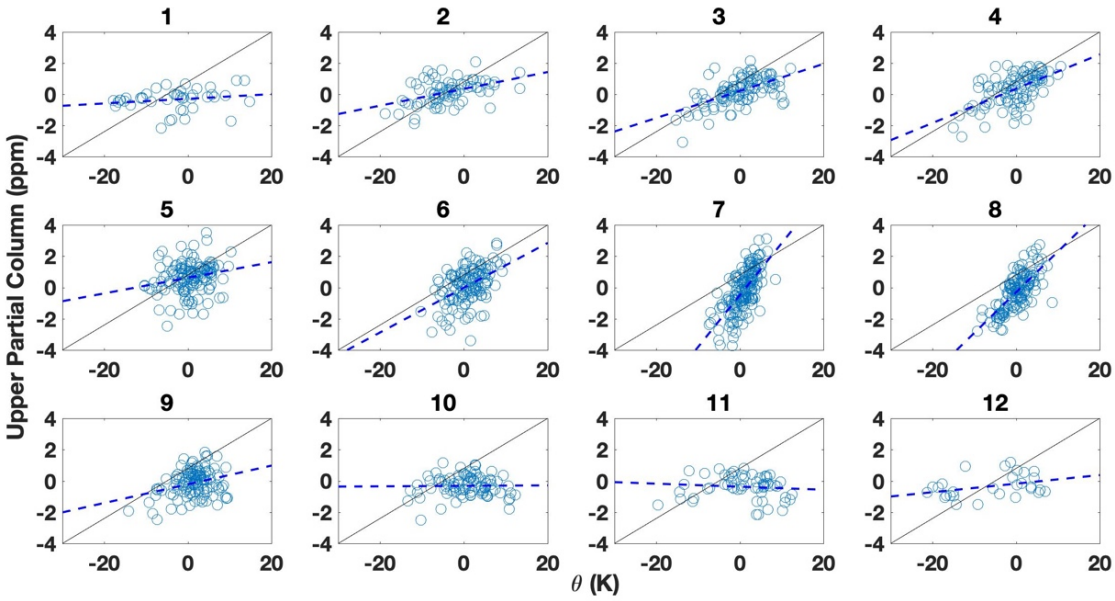

Figure C.1: Monthly comparisons of daily average TARDISS upper partial column CO_2 (y-axis) and the free tropospheric temperature (x-axis) at the Park Falls, WI, TCCON detrended using a 30-day moving mean. The dashed blue line is the linear fit of the data. The solid black line is the same slope between each panel as a visual aid. Panel titles represent the month of the year with "1" representing January and "12" representing December.

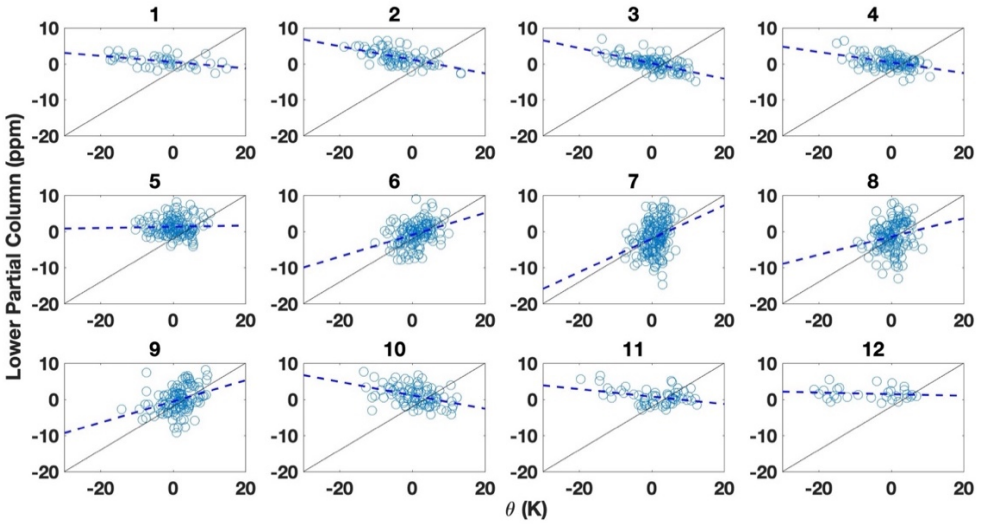

Figure C.2: Same as Fig. C.1 for the lower partial column values.

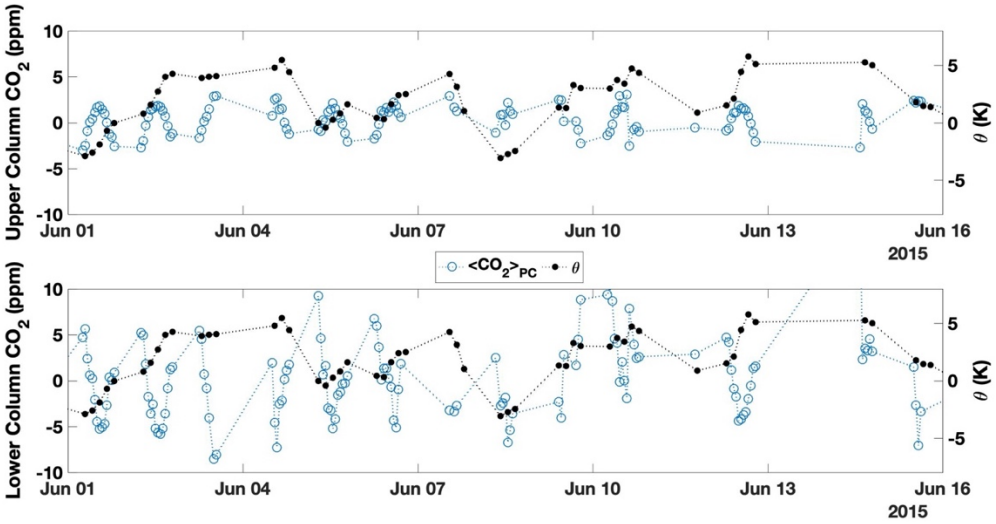

Figure C.3: Selected time series of hourly average TARDISS upper (top panel) and lower (bottom panel) partial column CO_2 (left axis, blue circles) and the reported three-hourly values of free tropospheric temperature (right axis, black squares) at the Park Falls, WI, TCCON detrended using a 30-day moving mean.

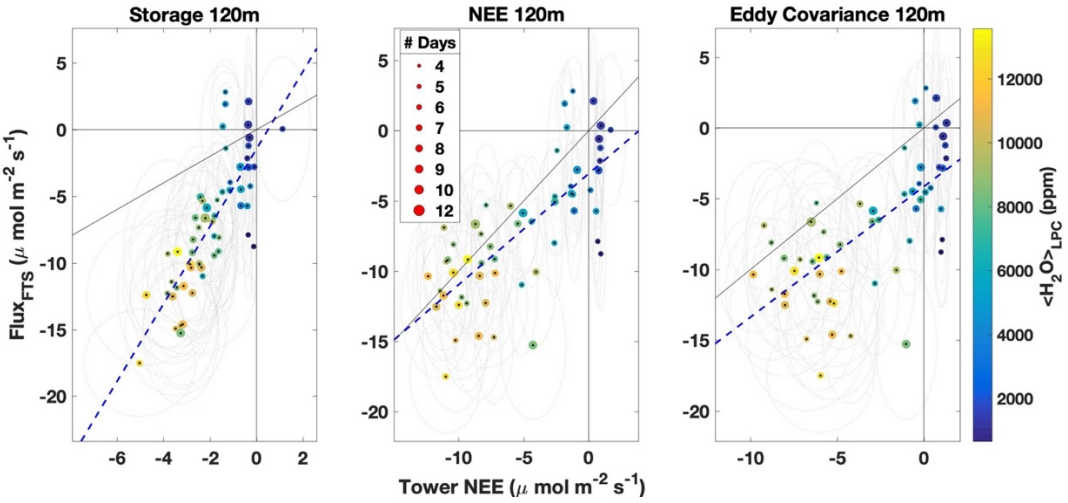

Figure C.4: Same as Fig. 4.3 for the 120m measurement level on the tower.

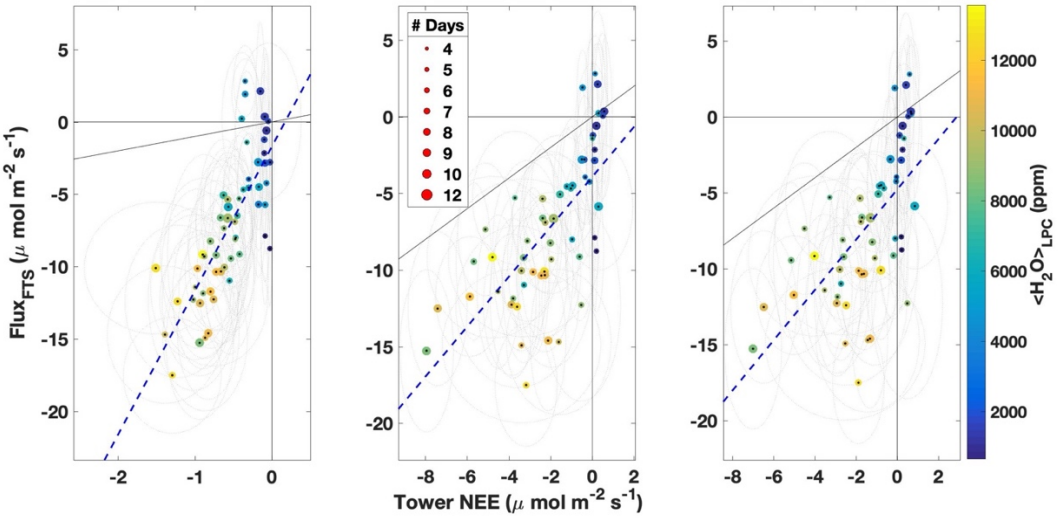

Figure C.5: Same as Fig.4.3 for the 30m measurement level on the tower.

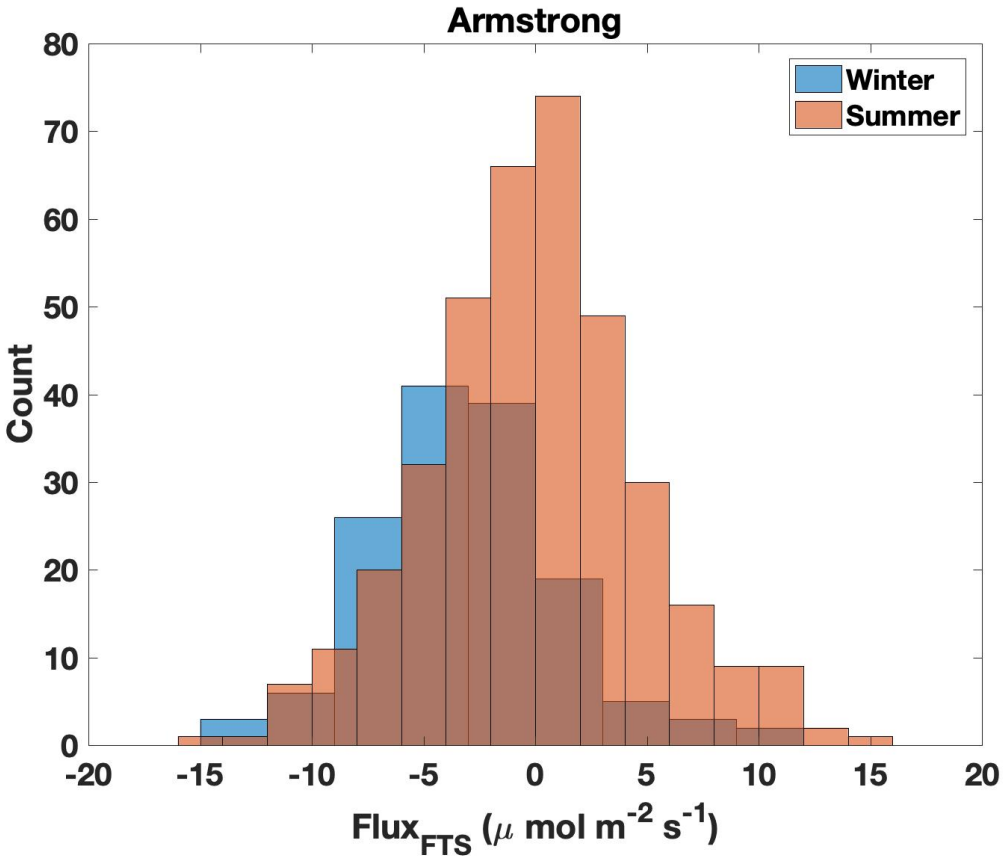

Figure C.6: Histogram of the daily $Flux_{FTS}$ values measured at the Armstrong TCCON site during the Winter (DJF) and Summer (JJA).

Measurement Height	Flux Type	Comparison Slope	Slope Error	Offset (μ mol m^{-2} s^{-1})	Offset Error (μ mol m^{-2} s^{-1})	R^2
396m	Combined NEE	0.651	0.117	-6.22	0.578	0.46
	Storage Fluxes	1.91	0.204	-1.32	0.735	0.62
	Eddy Covariance Fluxes	0.98	0.202	-8.41	0.631	0.40
120m	Combined NEE	0.790	0.097	-3.05	0.660	0.55
	Storage Fluxes	2.91	0.301	-1.44	0.704	0.63
	Eddy Covariance Fluxes	0.923	0.139	-4.14	0.653	0.45
30m	Combined NEE	1.63	0.240	-3.91	0.688	0.47
	Storage Fluxes	9.97	1.09	-1.69	0.720	0.60
	Eddy Covariance Fluxes	1.66	0.286	-4.77	0.671	0.39

Table C.1: Comparison statistics of the monthly values of the TARDISS-derived surface fluxes and in situ, tower estimated NEE, storage, and eddy covariance fluxes at 30, 120, and 396 meters.

	Armstrong NEE (μ mol m^{-2} s^{-1})		Park Falls NEE (μ mol m^{-2} s^{-1})	
	Mean	Standard Deviation	Mean	Standard Deviation
Total Year	-0.635	4.95	-5.14	8.58
Summer (JJA)	1.14	4.48	-10.7	9.43
Winter (DJF)	-3.39	4.56	-1.89	5.71

Table C.2: Statistics of the TARDISS-derived surface fluxes for the Armstrong and Park Falls TCCON sites for overall yearly, summer, and winter data.